

AD-A273 356

(2)



Intelligent Control of Chemical Vapor Deposition Processes

Third ^{FINAL} Annual Report

Contract No. F49620-90-C-0066

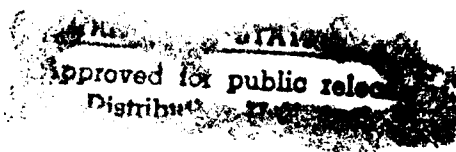
Prepared for:

Defense Advanced Research Projects Agency
Defense Sciences Office
3701 North Fairfax Drive
Arlington, Va 22209-2308

Administered by:
Air Force Office of Scientific Research
Building 410
Bolling AFB, DC 20332-6448

DTIC
SELECTED
NOV 29 1993
S E D

The data in this research report shall not be disclosed outside the Government and shall not be duplicated, used, or disclosed in whole or in part for any purpose other than to evaluate the research. The Government has the right to duplicate, use or disclose the data to the extent provided in the contract. This restriction does not limit the Government's right to use information contained in the data if it is obtainable from another source without restriction.



93-28368

87P

ISI Report No. 5008-03

September 1, 1993

Integrated Systems, Inc.

3260 Jay Street

Santa Clara, CA 95054-3309

Tel: 408.980.1500 Fax: 408.980.0400

93 11 19 012

REPORT DOCUMENTATION PAGE

Form Approved
OMB No. 0704-0188

Public reporting burden for this collection of information is estimated to average 1 hour per response, including the time for reviewing instructions, searching existing data sources, gathering and maintaining the data needed, and completing and reviewing the collection of information. Send comments regarding this burden estimate or any other aspect of this collection of information, including suggestions for reducing this burden, to Washington Headquarters Services, Directorate for Information Operations and Reports, 1215 Jefferson Davis Highway, Suite 1204, Arlington, VA 22202-4302, and to the Office of Management and Budget, Paperwork Reduction Project (0704-0188), Washington, DC 20503.

1. AGENCY USE ONLY (Leave blank)	2. REPORT DATE	3. REPORT TYPE AND DATES COVERED FINAL/01 SEP 90 TO 31 AUG 93
----------------------------------	----------------	---

4. TITLE AND SUBTITLE INTELLIGENT CONTROL OF CHEMICAL VAPOR DEPOSITION PROCESSES	5. FUNDING NUMBERS
--	--------------------

6. AUTHOR(S) DR. SUNIL SHAH	7745/00 F49620-90-C-0066 62712E
---	---------------------------------------

7. PERFORMING ORGANIZATION NAME(S) AND ADDRESS(ES) INTEGRATED SYSTEMS, INC 3260 JAY STREET SANTA CLARA, CA 95054-3309	8. PERFORMING ORGANIZATION REPORT NUMBER AFOSR-TR- 100-0047
---	---

9. SPONSORING / MONITORING AGENCY NAME(S) AND ADDRESS(ES) AFOSR/NM 110 DUNCAN AVE, SUITE B115 BOLLING AFB DC 20332-0001	10. SPONSORING / MONITORING AGENCY REPORT NUMBER F49620-90-C-0066
---	---

11. SUPPLEMENTARY NOTES

12a. DISTRIBUTION / AVAILABILITY STATEMENT APPROVED FOR PUBLIC RELEASE: DISTRIBUTION IS UNLIMITED	12b. DISTRIBUTION CODE
---	------------------------

13. ABSTRACT (Maximum 200 words)

Significant progress has been made in improving process control on the Technion TB reactor by using a model-based approach to control design. This approach has led to improvements in two areas. First, it has made the control design process more efficient by reducing the time required by a trial and error approach. This will lead to a cost saving in manpower. Second, it has led to design of effective controllers whose design is not evident in a trial and error approach. This has led to improved regulation of actuation and deposition conditions. Both these improvements are expected to lead to a quicker deployment to new deposition strategies and eventually to the cost-effective production of diamond. Progress made under this contract has set the stage for further refinement and implementation of these control strategies in a production environment. Work in this area is under progress on a related contract with Norton Diamond film entitled "Integration of Intelligent Process Control and Monitoring."

14. SUBJECT TERMS	15. NUMBER OF PAGES
-------------------	---------------------

16. PRICE CODE

17. SECURITY CLASSIFICATION OF REPORT UNCLASSIFIED	18. SECURITY CLASSIFICATION OF THIS PAGE UNCLASSIFIED	19. SECURITY CLASSIFICATION OF ABSTRACT UNCLASSIFIED	20. LIMITATION OF ABSTRACT SAR(SAME AS REPORT)
--	---	--	--

Integration of Intelligent Process Control and Monitoring

Third Annual Report

Contract No. F49620-90-C-0066

Prepared for:

Defense Advanced Research Projects Agency
Defense Sciences Office
3701 North Fairfax Drive
Arlington, Va 22209-2308

DTIC QUALITY INSPECTED 5

Administered by
Air Force Office of Scientific Research
Building 410
Boeing AFB, DC 20332-6448

Prepared by:

Pradeep Pandey
Jon Ebert
Valerie Lisiewicz
Ted Schulman
Tamara Artim

Accession For	
NTIS CRA&I	<input checked="" type="checkbox"/>
DTIC TAB	<input type="checkbox"/>
Unannounced	<input type="checkbox"/>
Justification	
By	
Distribution /	
Availability Codes	
Dist	Avail and / or Special
A-1	

Approved by:


Scot Morrison

Scot Morrison, Section Manager
Chemical Process Control


David S. Spain

David S. Spain, Director
Manufacturing Automation Dept.

Contents

1 Executive Summary	2
1.1 Background	2
1.2 ISI Goals	2
1.3 Summary of Accomplishments	3
1.4 Conclusion	4
2 Actuation Control	6
2.1 Introduction	6
2.2 Arc Power System	6
2.2.1 Summary	6
2.2.2 Model	7
2.2.3 Control Design and Results	8
2.2.4 Conclusion	11
3 Deposition Conditions Control	15
3.1 Introduction	15
3.2 Substrate Temperature	16
3.2.1 Summary	16
3.2.2 Model and Controller Design	16
3.2.3 Results	16
3.3 Chamber Pressure	17
3.3.1 Summary	17
3.3.2 Model	17
3.4 Gas Temperature	18
3.4.1 Summary	18
3.4.2 Experimental Results	18
A Arc Power Supply Control	26
A.1 Introduction	26
A.2 Description of Power Supply	27
A.3 Power Supply Model	28
A.3.1 First Order Open-Loop Model	28
A.3.2 Higher Order Open-Loop Model	30

A.3.3	Closed-loop Model	31
A.4	Experimental Results	32
A.4.1	Open-Loop Tests	32
A.4.2	Closed-loop Tests	34
A.5	Gain Tuning and Controller Design	39
A.5.1	Gain Tuning Example	42
A.6	Summary	48
B	Substrate Temperature Control	49
B.1	Model	49
B.2	Controller Design	50
C	Chamber Pressure Control	54
C.1	Introduction	54
C.2	Chamber Pressure Model	54
C.3	Model Validation	57
C.4	Controller Design	58
C.5	Further Issues	59
D	Gas Rotational Temperature Sensor	69
D.1	Introduction	69
D.2	Apparatus and Acquisition System	69
D.3	Rotational Temperature Estimation	70
D.4	Real-Time Implementation	73

Chapter 1

Executive Summary

This report describes results of work performed by Integrated Systems Inc. (ISI) on the project "Intelligent Control of Chemical Vapor Deposition Processes" from September 1, 1992 to August 31, 1993. This work is sponsored by Advanced Research Projects Agency (ARPA) and has been conducted in conjunction with efforts by Norton Diamond Film, a division of Norton Company, and Sandia National Laboratories.

1.1 Background

The plasma arc-jet process developed by Technion/Norton is a leading technology for production of large thin-film diamond. However, further improvements were needed to make the process cost-effective. The path to achieving this goal has been (1) to control deposition conditions and (2) to identify deposition conditions that lead to desired product quality and yield. One of the main problems is that plasma arcs are both inherently electrically unstable and prone to large disturbances in the power they deliver, requiring effective process control to maintain consistent deposition conditions. Previous process control has been largely implemented in the Honeywell Series 9000, and the settings for these controllers have been chosen by trial and error. This approach was tedious and often led to poor performance. ISI is involved in examining the adequacy of these controllers and using proven model-based techniques to improve control where necessary. This approach is expected to (1) enable reliable and efficient production of diamond film and (2) support Norton scientists in understanding optimal conditions for diamond deposition.

1.2 ISI Goals

ISI's goals have been to determine specifications for process control (jointly with Norton), evaluate adequacy of existing control systems, both in the Honeywell Series 9000 and elsewhere, and to design and implement model-based controllers where existing controllers fail to meet desired specifications. These upgraded control systems have been designed for and

implemented on the Technion research reactor (TB) and will soon be transitioned to Norton's production reactors as appropriate.

To meet these goals, ISI has developed a control architecture which divides the overall control strategy into three levels: actuation control, deposition condition control, and film properties control. Actuation control consists of control systems that regulate physical inputs to the reactor (e.g., arc power and hydrogen flow). Deposition condition control refers to the next level of controllers that regulate deposition conditions (e.g., substrate temperature and chamber pressure). Finally, film properties controllers are the outermost level controllers regulating diamond film properties. This architecture is shown Figure 1.1 and is described in detail in the Second Annual Report [1]. Based on this architecture, ISI has focused on implementing an actuation controller for (1) arc current, and deposition condition controllers for (2) substrate temperature, (3) chamber pressure, and (4) gas temperature. No film properties controllers were developed.

1.3 Summary of Accomplishments

Highlights of accomplishments are:

1. Improved control of the arc power system has been demonstrated. Specifically, the ability to tune the arc current controller was demonstrated on the Technion TB reactor. This has permitted stable arc operation at operating conditions where such operation was not possible with previous controller settings. In addition, no-ballast operation has been demonstrated. This will lead to reduced facility complexity and cost of operation. These improvements have been made with model-based control design based on a nonlinear parametric model of the arc power system.
2. An improved substrate temperature controller has been designed based on an empirical model. Results of this design have been used to update the controller settings in the Honeywell Series 9000. The new controller is several times faster than the previous one, and is able to reduce substrate temperature fluctuations.
3. Improved control of chamber pressure has been demonstrated. ISI has designed a controller based on a parametric model of chamber pressure and implemented it on an AC-100. This controller is several times faster than the one implemented in the Honeywell Series 9000. Based on this design, the settings of the Honeywell controller have been updated and are in use routinely.
4. ISI has designed and implemented an algorithm to estimate the gas temperature of the arc-jet plume. Gas temperatures obtained using this sensor compare well with those predicted by Norton's process models.

In addition to designing and implementing improved controllers, ISI has worked on providing communication links between sensors, data acquisition platforms, and an AC-100. Specific features of this environment include:

1. Real-time interface between an AC-100 and advanced sensors using GPIB/IEEE 488.
2. Macintosh/LabView real-time data acquisition architecture for model-based sensing.

This has led to an integrated environment to perform experiments to explore the deposition process.

1.4 Conclusion

Significant progress has been made in improving process control on the Technion TB reactor by using a model-based approach to control design. This approach has led to improvements in two areas. First, it has made the control design process more *efficient* by reducing the time required by a trial and error approach. This will lead to cost saving in manpower. Second, it has led to design of *effective* controllers whose design is not evident in a trial and error approach. This has led to improved regulation of actuation and deposition conditions. Both these improvements are expected to lead to a quicker deployment to new deposition strategies and eventually to the cost-effective production of diamond.

Progress made under this contract has set the stage for further refinement and implementation of these control strategies in a production environment. Work in this area is under progress on a related contract with Norton Diamond film entitled "Integration of Intelligent Process Control and Monitoring."

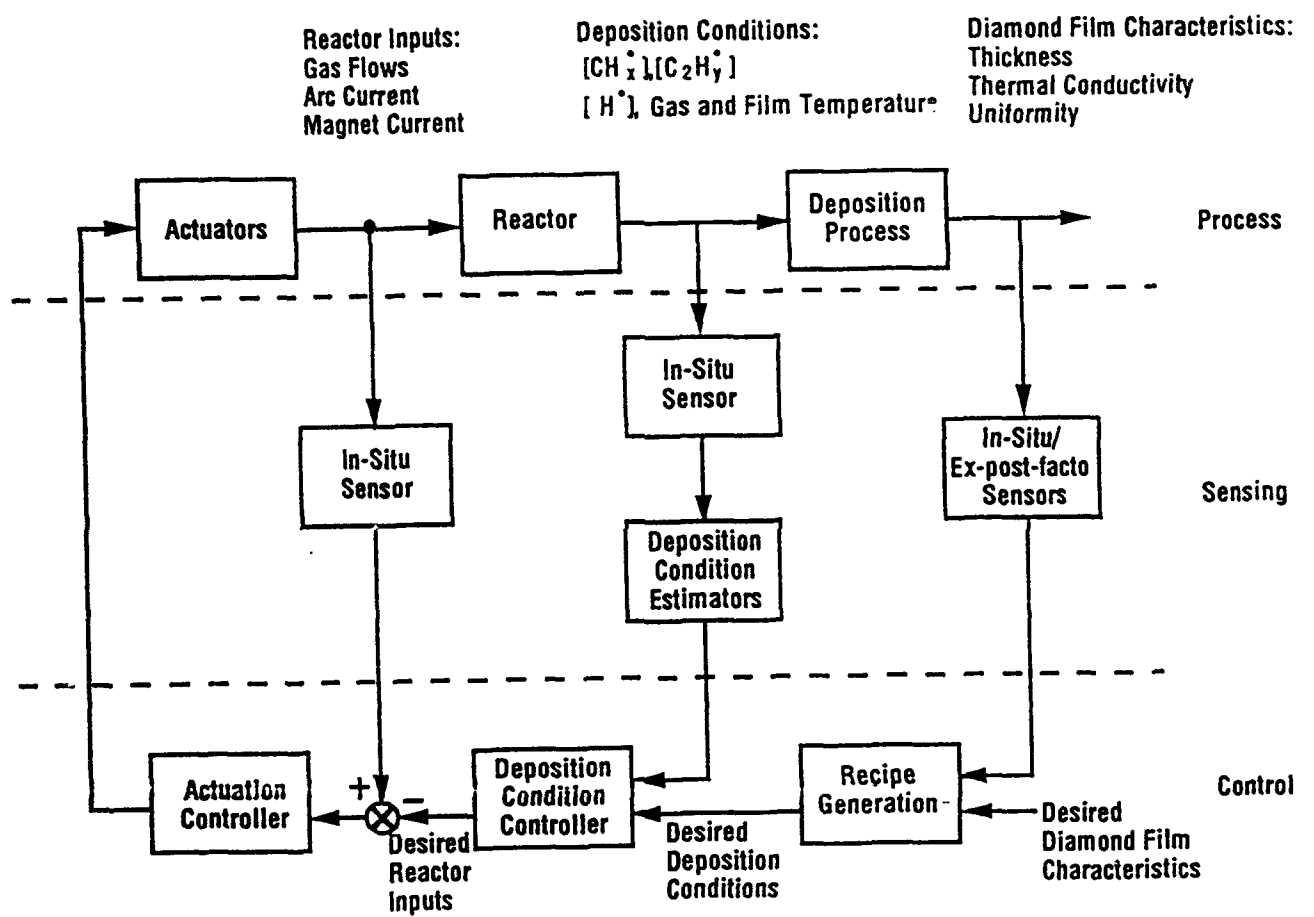


Figure 1.1: Process Control Architecture

Chapter 2

Actuation Control

2.1 Introduction

Actuation consists of the physical inputs to the reactor, e.g., gas flows and magnet and arc currents. The arc power system is the most important actuator since it affects two key deposition conditions (1) temperature of the substrate on which the diamond film grows, and (2) amount of atomic hydrogen produced. Fluctuations in substrate temperature are widely believed to be responsible for inferior diamond quality and loss of diamond film through premature separation from the substrate. While it is not possible, at present, to directly measure the amount of atomic hydrogen produced, atomic hydrogen concentration is believed to depend on the gas enthalpy, which is affected by arc power levels and fluctuations. Thus, controlling the amount of power delivered to the arc is fundamental to the overall process control. For this reason, ISI has focussed its efforts on the arc power system.

During this reporting period, ISI has demonstrated improved control of the arc power system. Specifically, the ability to tune the arc current controller was demonstrated on the Technion TB reactor. This has permitted stable arc operation at operating conditions where such operation was not possible with previous controller settings. In addition, no-ballast operation has been demonstrated. These improvements have been made with model-based control design based on a parametric model of the arc power system.

2.2 Arc Power System

This section summarizes the work done by ISI to control arc power. Details are given in Appendix A.

2.2.1 Summary

An arc is difficult to control because it is inherently electrically unstable and requires compensation for stability. One way to achieve stability is to add ballast resistance; this approach leads to wasted power and increased facility complexity involving cooling of ballast resistors.

Another alternative is to use feedback control. The solution employed by Technion was a combination of these approaches: to use ballast resistors and an analog PI controller to regulate the current. However, arc characteristics vary with operating conditions like arc current, gas flow rates, and engine configuration. Consequently, the arc power system behaved adequately for certain operating conditions and unacceptably for others. No method, other than trial and error, was available to retune the controller to recover performance. These problems are exacerbated by fluctuations in arc voltage.

To address these problems, ISI has designed control strategies based on a parametric model of the arc power system. This strategy has led to significant improvement in regulating arc power on the TB reactor. Specifically:

1. A procedure for tuning the Macroamp PI controller has been developed and tested. This procedure permits arc operation at operating conditions that were not possible with previously used gain settings.
2. ISI has prototyped an advanced control scheme using an AC-100. It is expected that this algorithm will be implemented in the upgraded Honeywell Series 9000.

In addition, the model of the arc power supply developed by ISI is expected to be useful in formulating specifications for future purchase of arc power supplies.

2.2.2 Model

The TB reactor is powered by an SCR-type power supply (Figure 2.1) consisting of the following major components:

- SCR bridge: a rectifier whose dc output depends on firing angle of the SCRs
- firing circuit: produces firing angle of the SCRs proportional to a firing command
- output inductor: provides smooth current
- ballast resistor: stabilizes the arc power system
- dc arc-jet

A parametric model has been developed to describe the behavior of this arc power system. Key features of this model are:

1. The stated nominal inductance is 55 mH. However, this value varies significantly with current (Figure 2.2). The implication of this variation is that the speed of response of the arc system varies accordingly, and can compromise system performance if not accounted for.
2. It was known that the arc impedance varies with operating conditions. Initially it was thought that arc impedance increases monotonically with current. However, experiments with various arc engines and operating conditions show that this is not always true (Figure 2.3). The implication of this variation is that the stability of the system can be compromised if not accounted for.

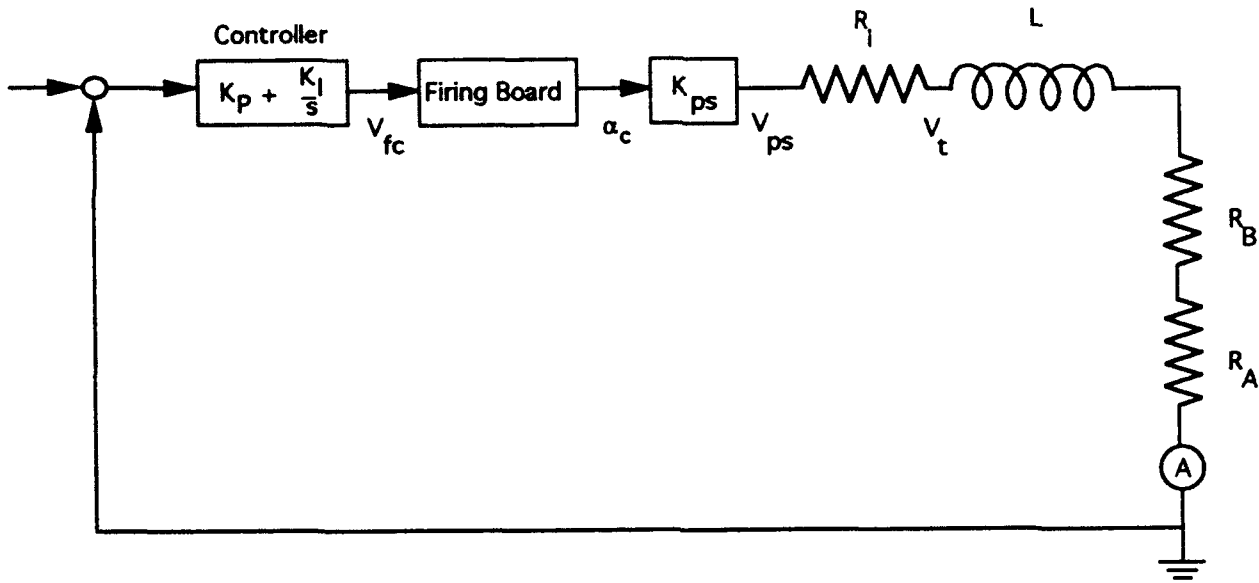


Figure 2.1: A schematic of a Macroamp power supply system

3. The output dc voltage is proportional to the firing command into the firing circuit board. However, the SCRs respond to a firing angle change only at discrete times, introducing a sample and hold type behavior. This limits achievable closed-loop performance.
4. The power supply is modeled as a voltage source with an internal resistance. This resistance affects the stability of the system.

The model is described in detail in Appendix A.

2.2.3 Control Design and Results

There are two low-level controllers associated with the existing power system. One regulates the current delivered by the power supply and the second regulates the power delivered by the arc. The current controller is an analog proportional plus integral (PI) controller

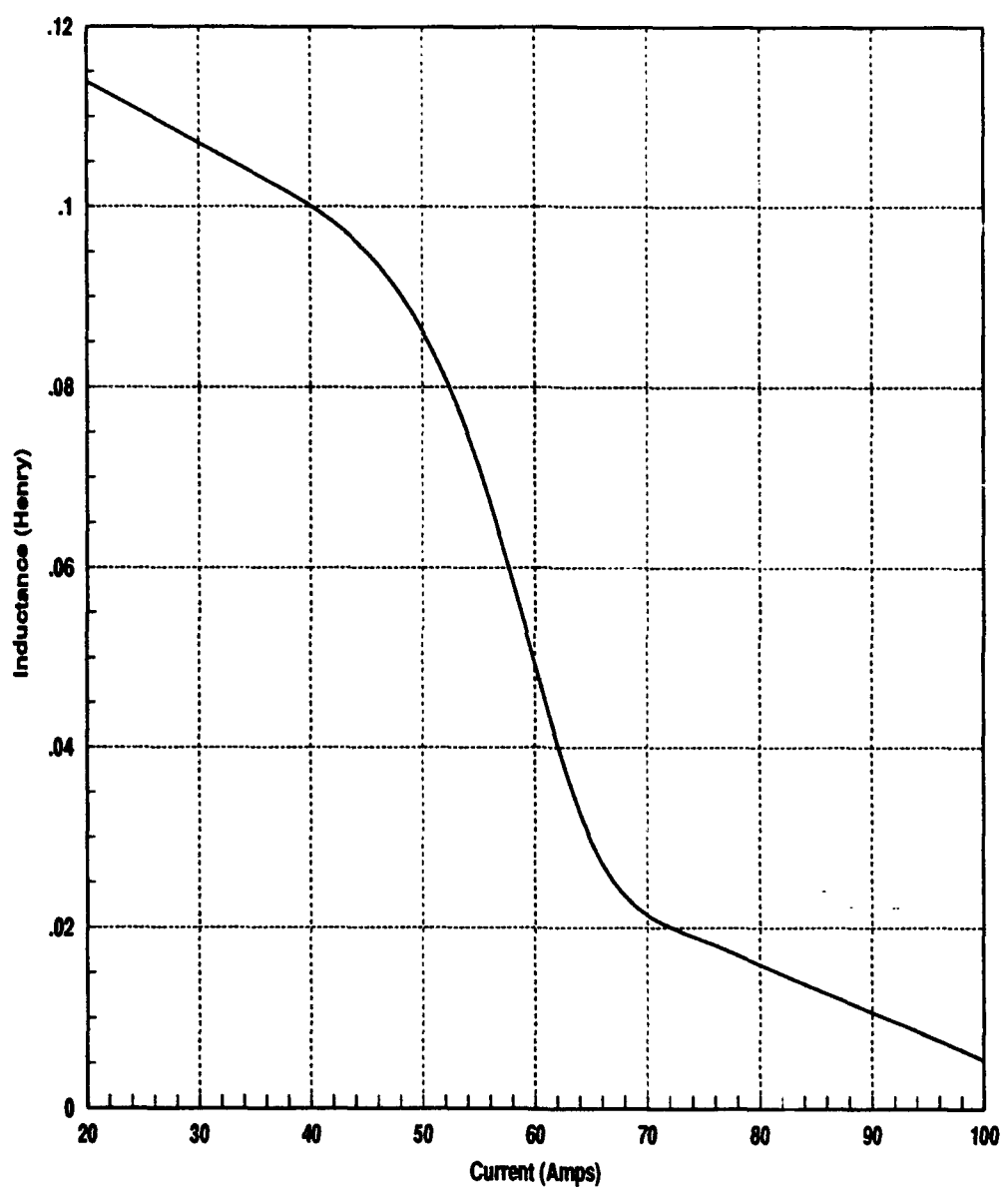


Figure 2.2: Variation of output inductance with current

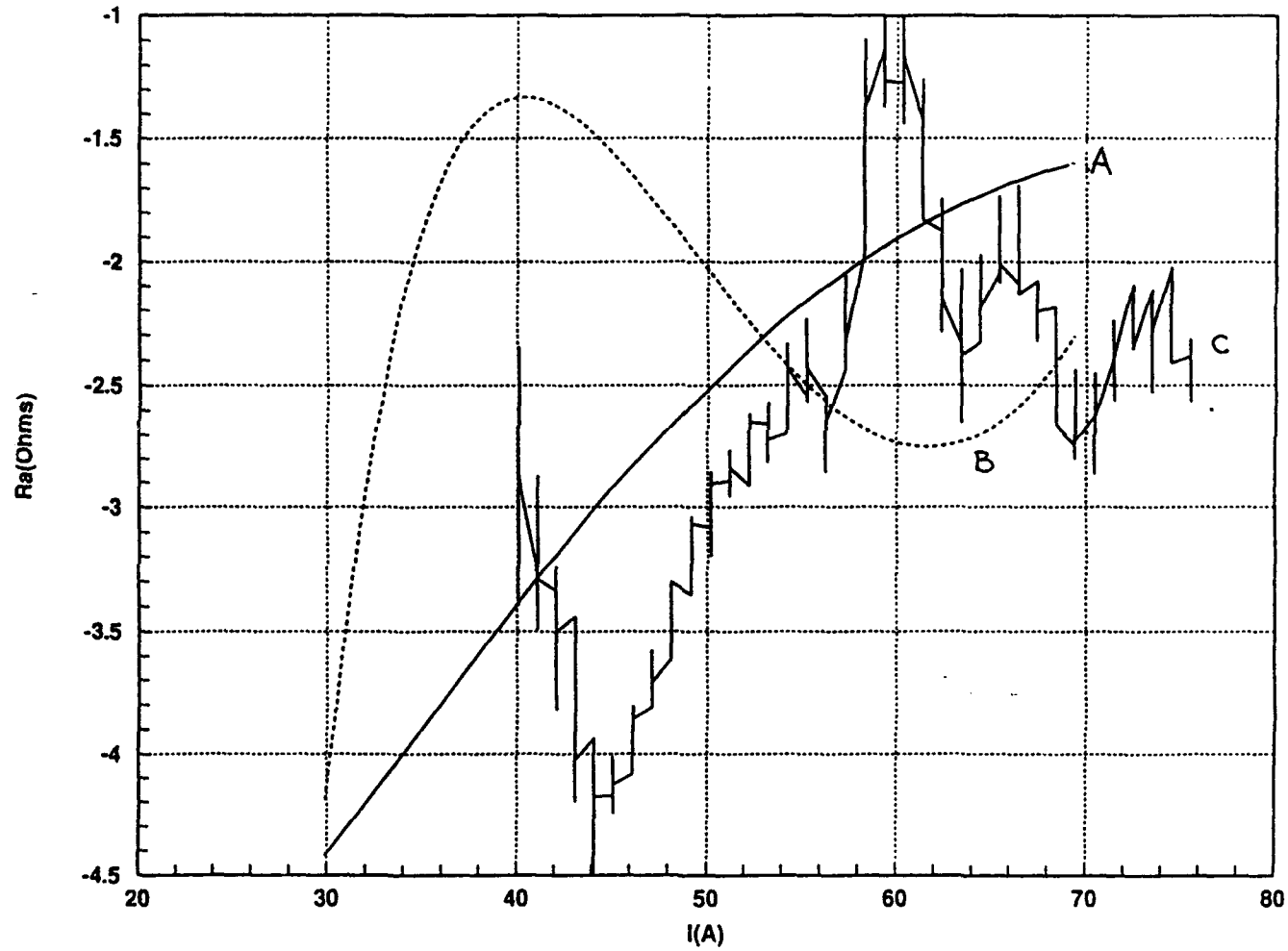


Figure 2.3: Arc resistance for three different operating conditions.

designed by Macroamp and is an integral part of the power supply. The power controller is also a PI-type implemented in the Honeywell Series 9000. It has limited bandwidth due to the relatively slow update rate (1.3 Hz) of the Honeywell control system. Neither of these controllers has been optimized for operation with the arc. In fact, the proportional and integral gains on the current controller board are often left as set by the vendor. However, if the gains are too low the system is well behaved at high currents but is oscillatory at low currents. The situation is reversed if the gains are too high. This behavior is summarized in Figures 2.4, 2.5, and 2.6, which represent, respectively, low, medium, and high gains. Hence, it is of interest to determine if these controllers can be adjusted or modified to operate over a wide range of operating conditions, without ballast resistors, and have improved disturbance rejection characteristics.

Based on the parametric model, ISI has designed and tested a method for tuning the gains of the Macroamp controller. This has enabled operation at current levels where the system had previously exhibited unacceptable oscillations. Experimental results confirm the validity of this method. A manual has been written to describe this tuning procedure (see Appendix E). Work on the arc power controller is in progress on the related contract with Norton Diamond Film.

2.2.4 Conclusion

Model-based control design has permitted improved control of the arc power system. Specifically, the ability to tune the arc current controller has made stable arc operation possible at operating conditions which were incompatible with previous controller settings. In addition to these advances, no-ballast operation has been demonstrated on the Technion TB reactor. This will lead to reduced facility complexity and cost of operation. These improvements have been made with *model-based* control design based on a parametric model of the arc power system.

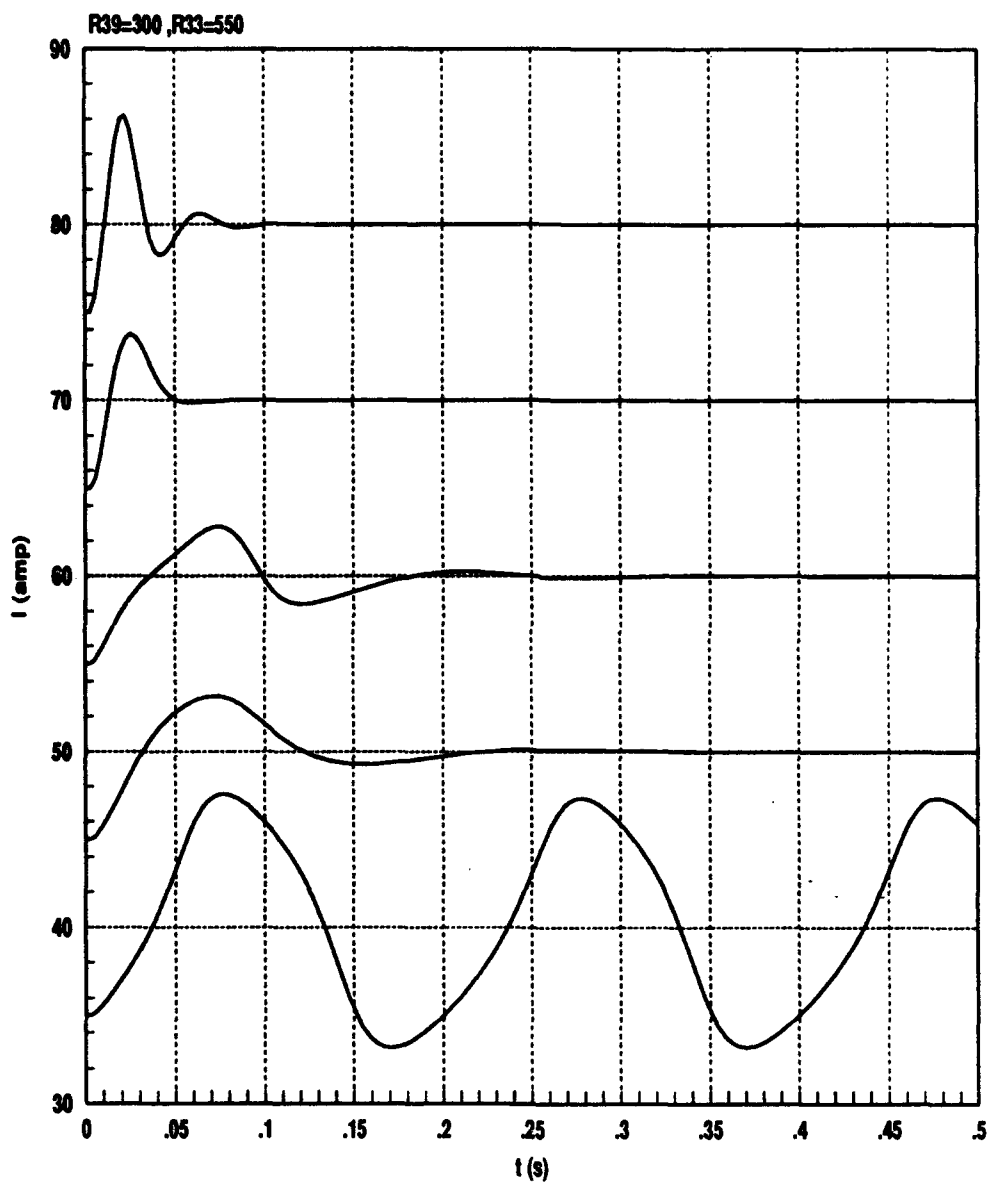


Figure 2.4: Arc current response for low controller gain settings

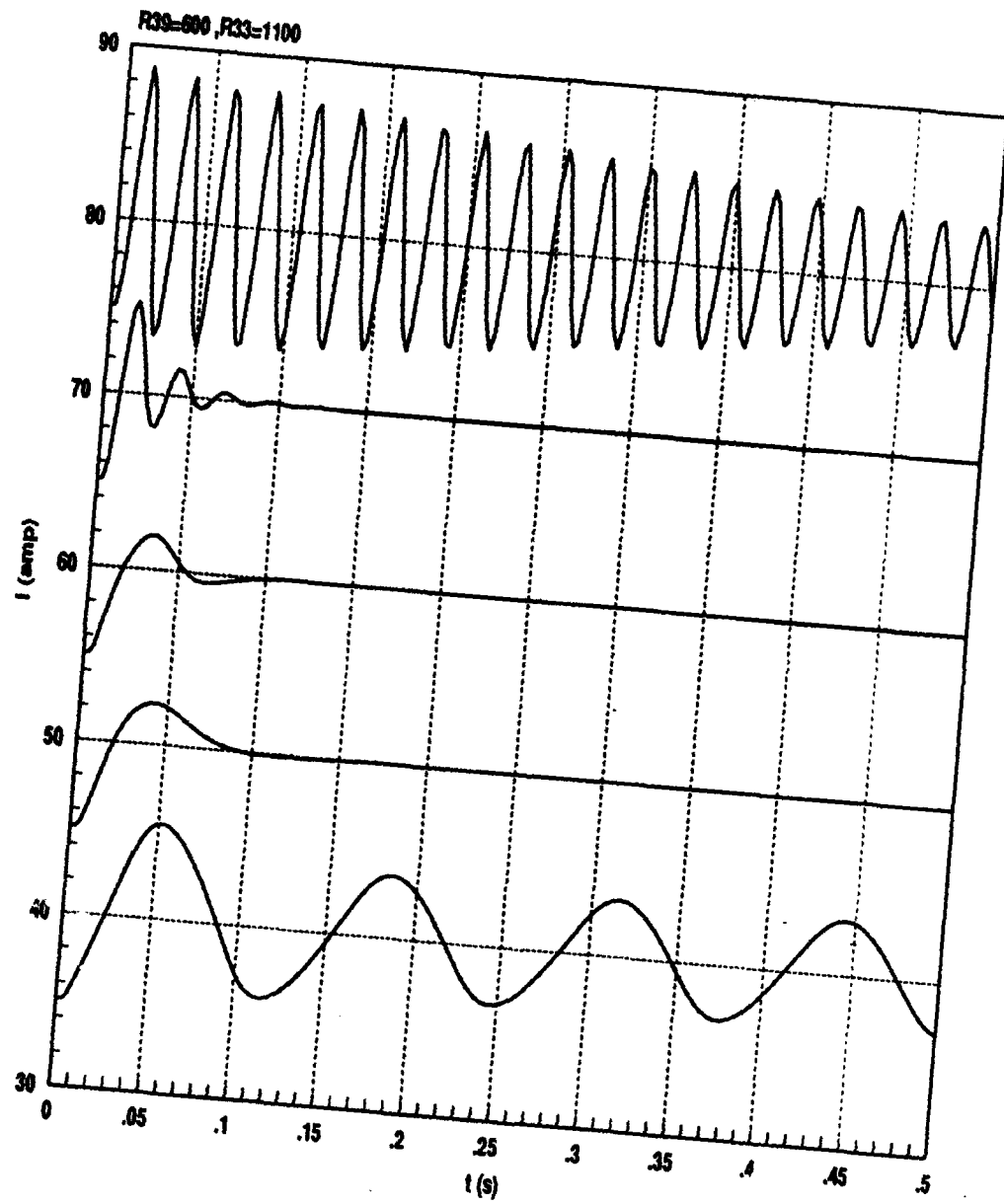


Figure 2.5: Arc current response for medium controller gain settings

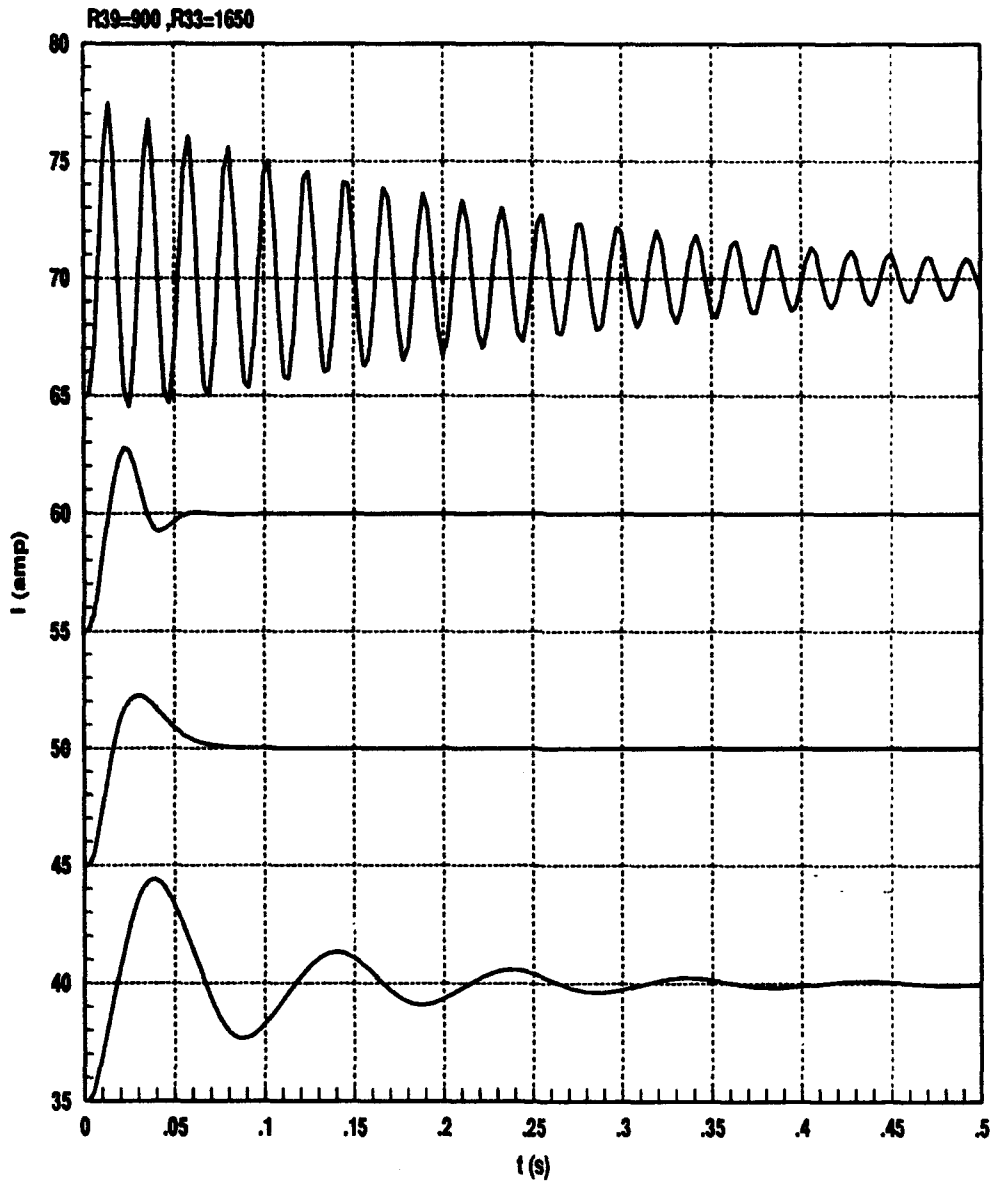


Figure 2.6: Arc current response for high controller gain settings

Chapter 3

Deposition Conditions Control

3.1 Introduction

Deposition conditions are physical conditions that exist at the diamond film surface. They include:

- Substrate temperature
- Chamber pressure
- Gas temperature
- Atomic hydrogen concentration
- Reactive carbon species concentrations

These conditions depend on reactor inputs, such as hydrogen flow and arc power, and on reactor configuration parameters, such as arc gap and substrate standoff distance. Deposition conditions directly affect growth rate of the diamond film and its properties such as thermal conductivity, morphology, and internal stress. Hence, it is important to regulate these conditions. ISI has focused its control design efforts on substrate temperature, chamber pressure, and gas temperature. Atomic hydrogen concentration and reactive carbon species were not examined in detail because reliable measurements of these quantities were not yet available. Specific accomplishments during this reporting period include:

- Development of an empirical model for substrate temperature and design and implementation of improved substrate temperature controller on an AC-100 and Honeywell Series 9000.
- Development of a parametric model for chamber pressure and design and implementation of a preliminary controller on an AC-100.
- Development of an algorithm for estimating gas temperature and its real-time implementation in LabView.

3.2 Substrate Temperature

3.2.1 Summary

Substrate temperature is an important deposition condition since it affects diamond film quality and yield. Production experience shows that changes in temperature of 10°C or more can cause the film to separate from the substrate and be destroyed. Also, thermal gradients across the film during growth are believed to be a source of film buckling after removal from the substrate. Hence, substrate temperature control is important for process repeatability and high yield. Previously, a PI controller implemented in the Honeywell Series 9000 was used to regulate the substrate temperature. However, the response of this controller was too slow to keep temperature fluctuations small.

To address this problem, ISI has taken the following approach. As a first step, ISI has developed a model-based approach to designing settings for the PI controller in the Honeywell 9000. This method of determining controller settings has been tested and validated on the Technion TB reactor. However, the setting were chosen conservatively to avoid significant power overshoot. Overshoot would help drive the thermocouple measurement to the desired temperature more quickly, but at the potential cost of larger temperature excursions at the diamond/gas interface. Predictive models and alternative sensor configurations that could remove this limitation are under investigation.

3.2.2 Model and Controller Design

The following first-order differential equation was used to model the substrate temperature:

$$\tau \dot{T} = -T + KP$$

where τ is the time constant (time to 63% of the steady state response to a step arc power change), and K is the steady state gain (number of degrees change in response to a unit step arc power change). These parameters can be determined from the temperature time response. Typical values of these parameters for the Technion B research reactor are $\tau = 40$ second and $K = 30^\circ\text{C}/\text{kilowatt}$. Although the model is clearly a simplification, it is more than sufficient for designing a controller. And because its parameters are directly observable from reactor behavior, an off-line program computing the controller gains can be run whenever the system parameters, e.g., substrate standoff or cooling flows, are changed. The controller selected is PI on the substrate temperature fed back to arc power.

3.2.3 Results

The new controller was first tested on an AC-100 and then implemented on the Honeywell Series 9000. Figure 3.1 compares experimental and simulation results for the substrate temperature for a 10°C step command. The results compare well and prove the model-based approach for control design. The next step is to use a model for diamond film temperature

as a function of arc power and substrate temperature measurement to design a faster temperature controller for further reducing the effects of disturbances. More detailed results are shown in Appendix B.

3.3 Chamber Pressure

3.3.1 Summary

Chamber pressure affects many deposition conditions, including process chemistry and arc resistance. Hence, it is desirable to minimize pressure variations. The chamber pressure has been regulated by a PI controller implemented in the Honeywell Series 9000. In the past, gains for this controller have been determined on an ad hoc basis. ISI has determined that this controller responds much too slowly to changes in setpoint, and that it will not be able to adequately regulate the chamber pressure.

To address this problem, ISI has developed a model-based controller, implemented it on an AC-100, and tested it on the TB reactor. The design is based on a parametric model that was validated by conducting experiments on the TB reactor. Although both the model and controller are preliminary, experimental results indicate that this controller outperforms the one implemented in the Honeywell Series 9000. Work on refining the model and controller is proceeding under a new contract with Norton Diamond Film.

3.3.2 Model

A schematic of the reactor chamber is shown in Figure 3.2. The pressure in the chamber, P , is controlled by adjusting the mass flow either into or out of the chamber. The mass flow out of the chamber is controlled by adjusting the exhaust valve position, θ , while the mass flow into the tank is regulated by mass flow controllers.

Mass balance, along with the ideal gas equation of state, $P = mRT/V$, forms the basis of the parametric model. We assume that R , T , and V are constant, and that the gas is entirely molecular hydrogen. Differentiating the ideal gas equation of state with respect to time and taking mass balance into account gives

$$\dot{P} = (\dot{m}_{in} - \dot{m}_{out})RT/V.$$

Experimental results indicate that \dot{m}_{out} can be modeled as $\dot{m}_{out} = f(\theta)P$, where external pressure is assumed constant, yielding the following expression for the chamber pressure dynamics

$$\dot{P} = -\frac{f(\theta)RT}{V}P + \frac{\dot{m}_{in}RT}{V}.$$

While the valve position, θ , ideally equals the valve position command, the valve does not respond instantaneously to the command. Valve dynamics, hysteresis, and other issues are discussed in Appendix C.

Control Design and Results

To design a controller at a given operating point, the model is linearized about the operating pressure and flow rate. Based on this linearized model, a PI controller was designed and implemented on an AC-100. Figure 3.3 compares the responses of this model-based controller to the previous controller to a step change in pressure command. With the model-based controller, the pressure reaches steady-state within 50 seconds while the old controller takes over 300 seconds. However, the model-based controller exhibits an overshoot of about 4 torr and considerable ringing. Clearly, there is room for further improvement in the new controller. These intermediate controller results are evidence of the capability of a model-based control scheme. Further model refinement and controller design is underway on a related contract with Norton Diamond Film.

3.4 Gas Temperature

3.4.1 Summary

A new sensor was developed to provide an estimate of the gas temperature in the plume of the arc-jet. This sensor estimates the gas temperature by measuring the rotational temperature of the 431 nm CH emission band (the CH-A \rightarrow X band). A model-based approach was adopted in which emission spectra are compared to theoretical predictions of rotational spectra as a function of temperature. The algorithm for comparing the theoretical and measured spectra has been incorporated into a LabView module to provide real-time analysis of the rotational temperature. Preliminary results are encouraging, and compare well with equilibrium calculations and expected temperatures. Appendix D provides a more detailed discussion of the work.

3.4.2 Experimental Results

Preliminary results from the gas temperature sensor are encouraging. Figure 3.5 illustrates some results obtained on the TB reactor at Technion using the real-time LabView implementation of the rotational temperature sensor. Gas temperatures have been found to be in the range from 2000-3000K. The gas temperature as a function of enthalpy (power/flow rate) can be computed assuming the hydrogen gas is in chemical equilibrium. Specifically, when hydrogen gas is heated, some fraction of the input power is spent dissociating the H₂ molecules, producing ions, and changing the internal energy level of the molecules. The remainder of the power is spent raising the temperature of the gas. Therefore, we expect the temperature of the gas to increase less than linearly with enthalpy. The measured rotational temperature, shown as symbols in Figure 3.5, seems to be in reasonable agreement with this equilibrium calculation.

Another feature of the rotational temperature sensor that is encouraging is the near-Gaussian shape of the noise distribution. Figure 3.4 illustrates this effect. By measuring the rotational temperature approximately 200 times at the same operating point and plotting

a histogram of the results, it is illustrated that the distribution of temperatures about the mean is approximately Gaussian. While this does not speak to the accuracy of the technique, it does provide insight into the noise characteristics and precision. For example, for Figure 3.4, the standard deviation for the measurement is 14.1K. Although not illustrated here, this precision was found to be sensitive to the emission signal levels, as was expected. Weaker signals require many more samples to achieve similar levels of uncertainty. The error bars shown on the rotational temperatures in Figure 3.5 are approximately $\pm 2\sigma/\sqrt{N}$, where $N \geq 30$. It is evident that a gas temperature sensor will be of considerable benefit to understanding diamond deposition process. At present, the sensors being used to characterize the operating conditions are, apart from substrate temperature, somewhat removed from the actual diamond deposition process. While the arc power and enthalpy are important, they are not as intimately associated with the deposition chemistry as the gas temperature. The gas temperature determines the H atom concentration in the arc-jet plume, which limits the H atom flux to the surface, which ultimately limits the diamond film growth rate (for a specified quality).

From the discussion above, two approaches for implementing the rotational sensor are being considered. One approach is to simplify the rotational temperature sensor to a point that it may not be measuring gas temperature, *per se*, but can be used as a metric of the "chemical state" of the plume. While this approach is reasonable, it does not take full advantage of the possible benefits that can be derived from understanding the arc-jet chemistry, an understanding which is augmented by the rotational temperature measurements. Therefore, the second approach is to improve the model for the rotational temperature, and use it as a diagnostic for arc-jet chemistry and fluid mechanics. This latter approach involves cooperation with scientists from Norton, SRI, and Sandia, and is expected to be of considerable benefit.

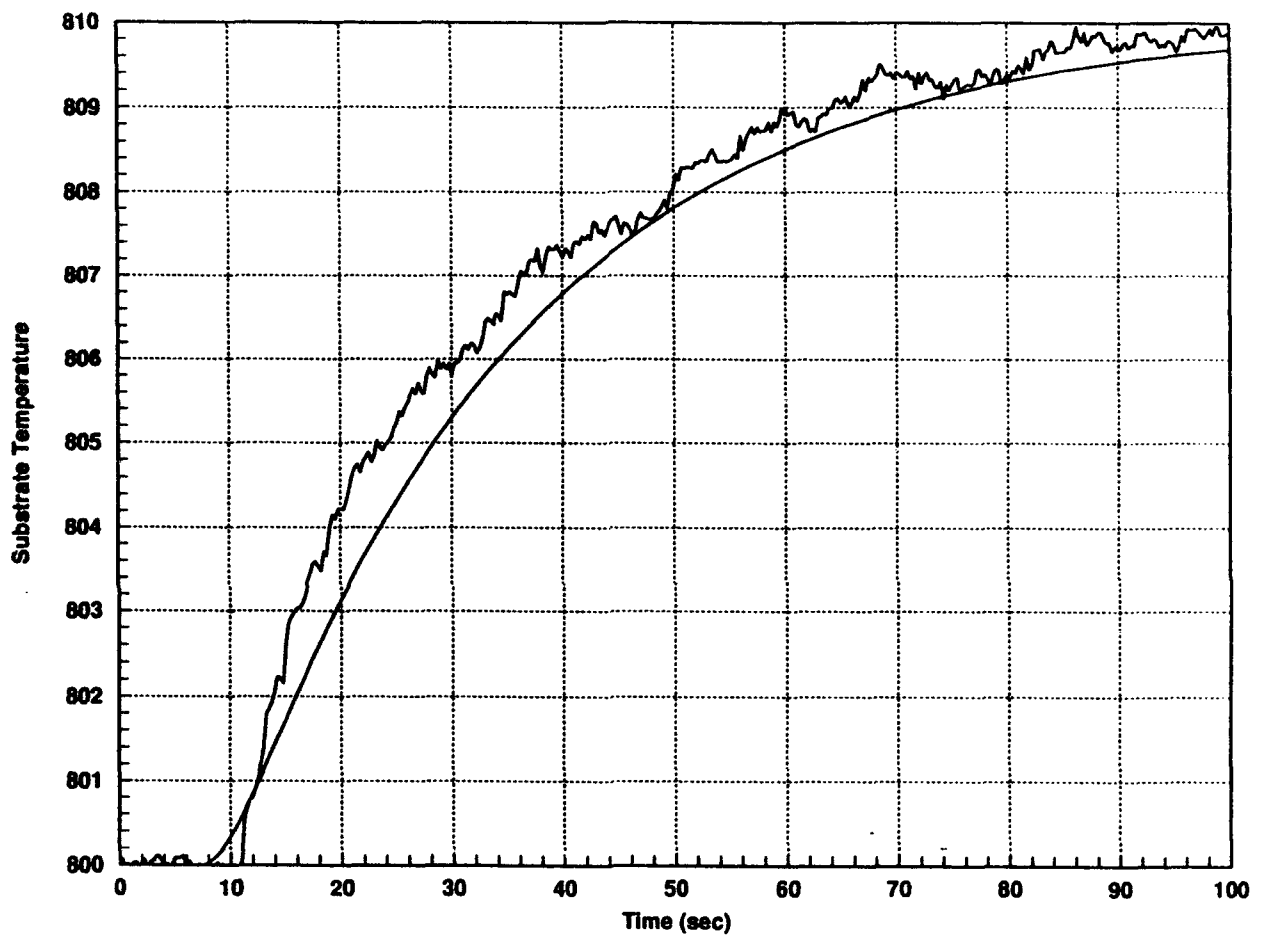


Figure 3.1: Comparison of experimental and simulated response of substrate temperature with the model-based controller for a 10°C step command.

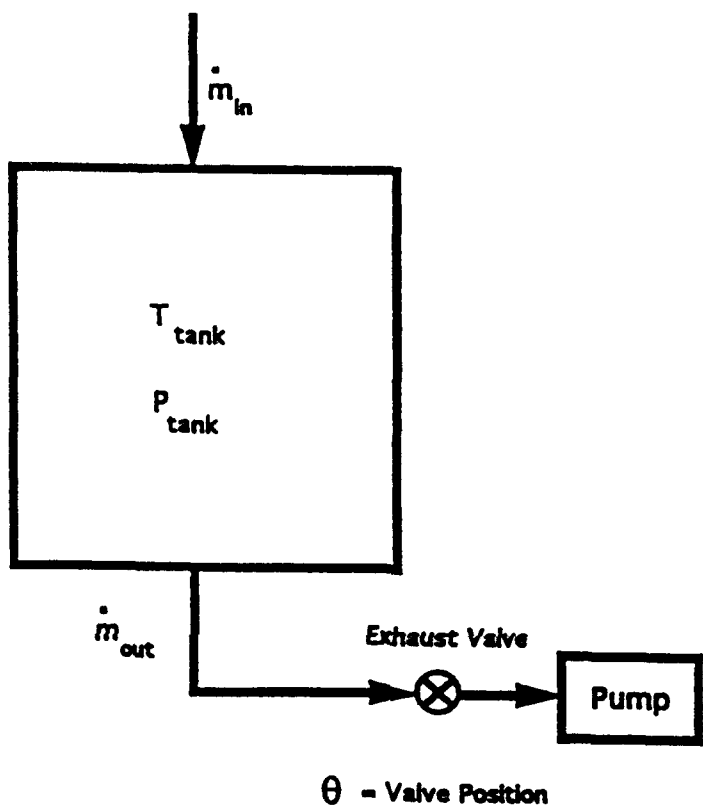


Figure 3.2: Tank pressure model

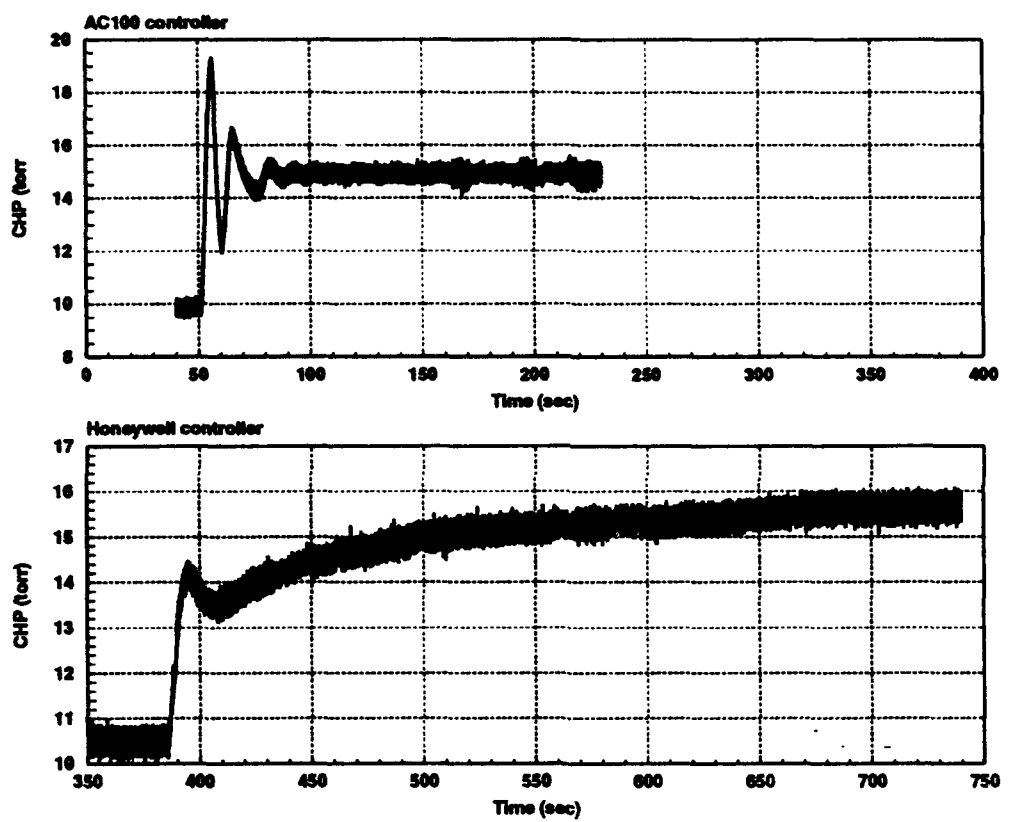


Figure 3.3: Honeywell/AC100 PI Comparison

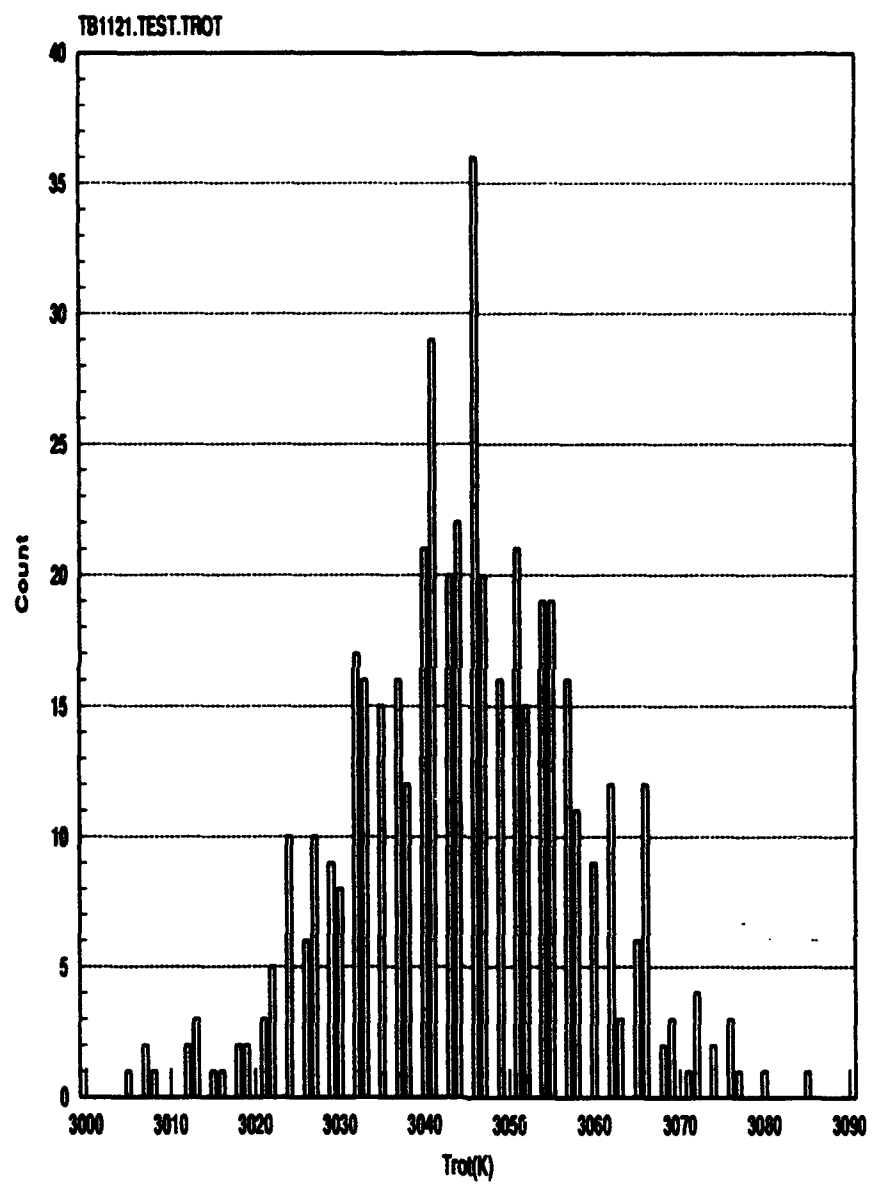


Figure 3.4: Histogram of Rotational Temperature.

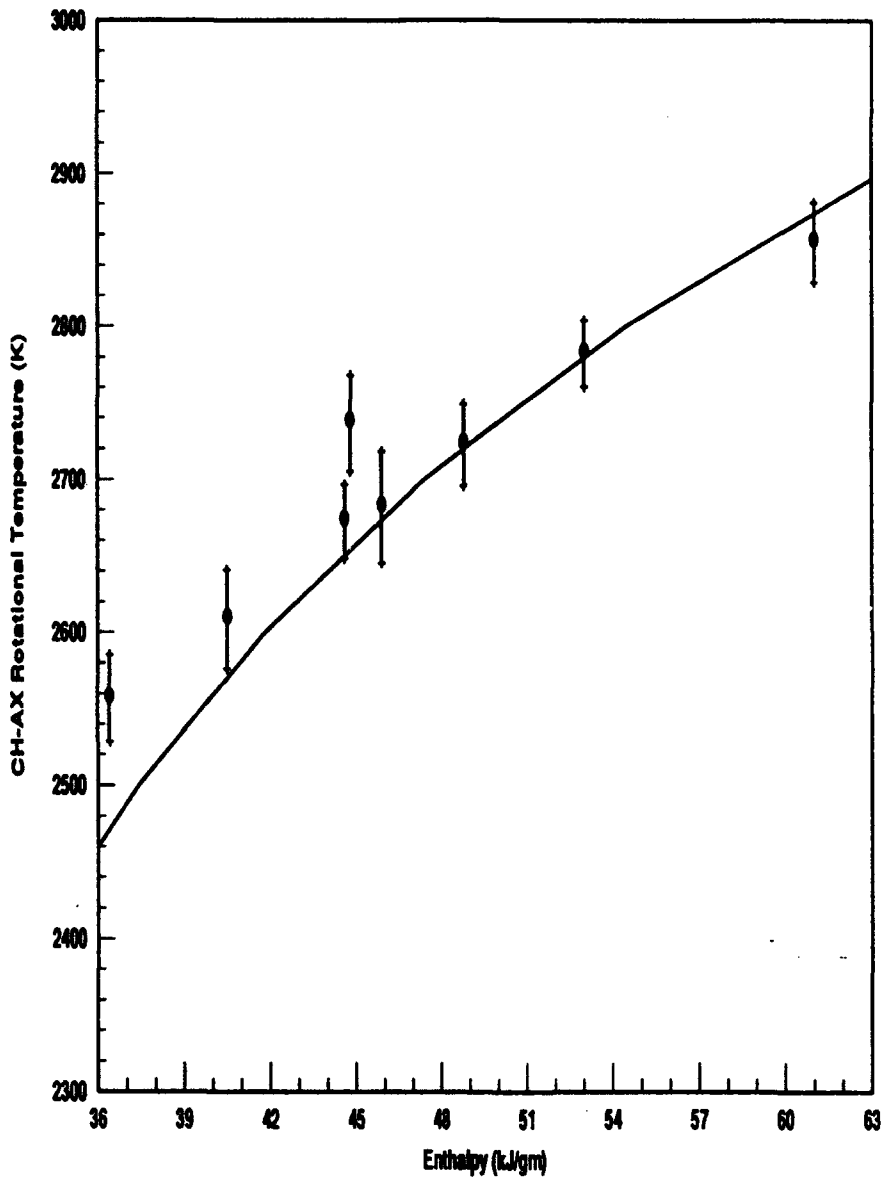


Figure 3.5: Rotational temperature versus enthalpy compared to an equilibrium calculation assuming $\text{H}_2\text{-H}_2$ equilibrium.

Bibliography

- [1] Pradeep Pandey, V. Lisiewicz, T. Schulman, and B. Schwarz, 1992, Intelligent Control of Chemical Vapor Deposition Processes, Second Annual Report
- [2] Jon Ebert, 'Results of Power Supply Tests', 30 June 1993 to 2 July 1993, ISI internal report
- [3] Jon Ebert, V. Lisiewicz, P. Pandey, 'Tuning the Arc Current Controller', June, 1993

Appendix A

Arc Power Supply Control

A.1 Introduction

The operation of a DC arcjet is complicated by the inherent instability of the arc. In most circumstances the voltage across an arc decreases with increasing current. This negative slope ($R_a = dV/dI$) of the I-V characteristic results in a load that is unstable when powered by a typical power supply (voltage source with small internal resistance). One can stabilize the circuit passively by adding enough series resistance (ballast) to make the net slope of the I-V curve positive. This approach has been historically employed for arcs, but the waste of power in the ballast resistors makes it unattractive.

An alternative approach to stabilizing the arc circuit is feedback control. In this approach a control circuit continuously monitors the current through the arc (I) and adjusts the power supply voltage to maintain constant current. Presently a PI (proportional+integral) controller internal to the Macroamp power supply is being used. The compensation provided by this controller is adjustable (tunable) through potentiometers on the control circuit which set the proportional and integral gains.

The control issue is not entirely resolved by addition of the PI current controller to the Macroamp power supply, since the PI controller *tuned* for one operating condition may not provide adequate control at other operating conditions. As described above, the stability of the system is degraded when the slope of the I-V curve, or arc resistance, R_a , becomes more negative. Experiments have confirmed that R_a is dependent on most operating parameters, including arc engine geometry, arc current, chamber pressure, and magnet current. Tuning the PI controller on the Macroamp is required every time the operating parameters change, and even then, insufficient knowledge of the system makes ad hoc manual tuning unpredictable. To further complicate matters, there is evidence that the arc characteristics change unpredictably during long deposition runs. Since the Macroamp PI controller cannot

be adjusted during a run, the circuit may become unstable if R_a changes too much. If the change in R_a is more moderate, the system can remain stable but the controller becomes less capable of rejecting voltages disturbances in the arc.

To address these problems, ISI has designed control strategies based on a parametric model of the arc power system. This strategy has led to significant improvement in regulating arc power on the TB reactor. Specifically:

1. A procedure for tuning the Macroamp PI controller has been developed and tested. This procedure permits arc operation which was not possible with previously used gain settings.
2. ISI has prototyped an advanced control scheme using an AC-100. It is expected that this algorithm will be implemented in the upgraded Honeywell Series 9000.

The advances listed above were possible through the development of an accurate model of the power supply. This model has been tested and found to be predictive of power supply performance for measured power supply parameters. In addition, the model developed by ISI is expected to be useful in formulating specifications for purchase of future power supplies.

A.2 Description of Power Supply

The power supply is comprised of four main components: an SCR bridge rectifier, a firing circuit, a current controller, and an output choke (inductor). (see Figure A.1). A brief description of each of these components is described in this section. For more details see the Macroamp power supply manual.

The SCR bridge consists of two full-wave three-phase bridges in series, each with six SCRs. A transformer separates the primary 3 ϕ -480VAC input from the SCR bridges using a delta primary to drive both delta and wye secondaries. Firing pulses are issued by the firing circuit to each of the 12 SCRs. The output voltage, V_t , of the power supply is controlled by selecting the delay of each pulse. When the SCR non-conduction time, or the delay angle, α , is large the output voltage is small since the SCRs are non-conducting for most of the 60Hz cycle driving them. Conversely, when the delay angle is small the output voltage is high, up to the limit of $\alpha = 0$ where the SCR bridges operate as 3 ϕ full-wave bridges with a maximum voltage near 1400 V.

The firing circuit can issue a pulse to a specific SCR only once every 60 Hz cycle. Since the firing circuit (Enerpro 6100, 6-pulse FCB) issues a pulse to the delta SCR bridge every 1/360 sec, it cannot change the delay angle any faster than once every 360 Hz cycle. The 6-pulses going to the second SCR bridge, the wye bridge, are issued 30° after the pulses to

the corresponding phases on the delta bridge. The result of this mode of operation is that the SCR bridge/firing circuit combination causes the power supply to perform as a 360 Hz sample and hold.

The delay angle of the SCR gate pulses is set by a firing command, V_{fc} , input to the firing circuit. When this command is issued by the Macroamp current controller or an AC100 controller it is referred to as *closed-loop* operation. The power supply can also be operated *open-loop* by injecting V_{fc} directly (e.g., with a constant voltage source). The normal mode of operation is *closed-loop* where the current controller continuously adjusts the firing command to make the measured current, I , agree with the commanded current I_c . The model that describes this mode is called the *closed-loop model*. Further details of the hardware of the power supply can be found in the Macroamp manual.

Finally, the output choke, or inductor, is wired in series with the power supply to smooth the current ripple through the circuit. The inductance, L , of the choke varies with current. At low currents the inductance is high, but as the current increases the core of the inductor begins to saturate and the inductance falls. For example, the TB Macroamp shows a variation in L from approximately 0.11 H to 0.02 H over the current range of the supply. The effect of the inductance on the power supply performance is significant, since it limits the rate at which the current through the circuit can change. Consequently, when L is small the system is fast, and the compensation must be proportionately fast, and when L is large the system is slow and the compensation must likewise be slow. This large variation of L with operating current significantly affects the controller design, as is discussed in the following sections.

A.3 Power Supply Model

An *ideal* power supply can hold a constant voltage regardless of the current drawn. However, in a real power supply the output voltage drops as the current drawn increases. This behavior is modelled by an ideal voltage source in series with a resistor called the internal resistance, R_I . Thus, the output voltage is

$$V_t = V_{ps} - R_I I. \quad (\text{A.1})$$

where V_t is the output terminal potential and V_{ps} is the ideal voltage source potential.

A.3.1 First Order Open-Loop Model

From a very basic point of view, the power supply is an adjustable DC voltage source, providing a commanded voltage across a load. The firing circuit provides the mechanism for adjusting the DC voltage output of the SCR bridge. Thus, as a first approximation, it is reasonable to model the firing circuit and the SCR bridge as a gain, K_{ps} , which represents

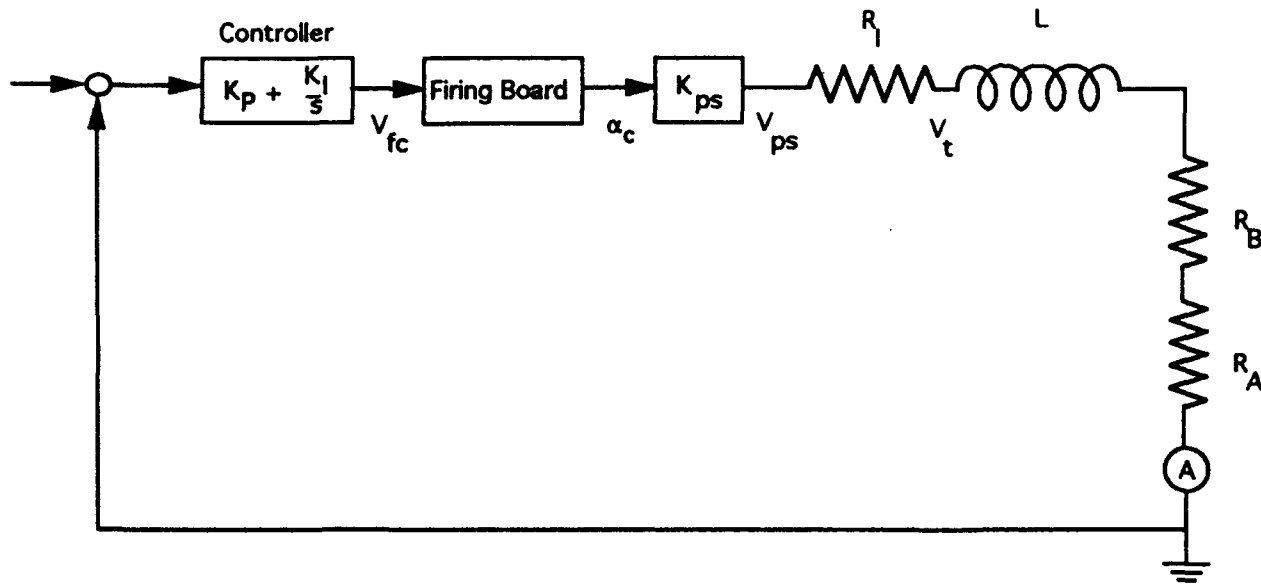


Figure A.1: A schematic of a Macroamp power supply system

the gain between the firing circuit command V_{fc} and the power supply voltage V_{ps} , that is,

$$V_{ps} = K_{ps} V_{fc} \quad (\text{A.2})$$

The load on the power supply consists of the inductor, with voltage drop $L(I)dI/dt$, the optional ballast resistor, with voltage drop $R_B I$, and the arc. The arc voltage can be modeled near some fixed operating point as a linear function of current, or

$$V_a = V_0 + R_A I \quad (\text{A.3})$$

Summing these voltages across the power supply output gives

$$V_t = V_{ps} - R_I I = L(I) \frac{dI}{dt} + R_B I + V_0 + R_A I \quad (\text{A.4})$$

Adding the power supply model described above gives

$$L \frac{dI}{dt} + R_T I = K_{ps} V_{fc} - V_0 \quad (\text{A.5})$$

as the open-loop model of the power supply/load circuit. Here the total resistance, R_T is defined as

$$R_T = R_B + R_I + R_A \quad (\text{A.6})$$

Thus, for this level of approximation, the open-loop transfer function is a first order lag with time constant $\tau = \frac{L}{R_T}$ and gain K_{ps} .

A.3.2 Higher Order Open-Loop Model

While the first order model described above correctly identifies the principal model parameters R_T/L and K_{ps}/L , it does not accurately represent the sample and hold characteristic of the SCR bridge operation or the dynamics of the firing circuit response to changes in firing command. In this section the details of an accurate open-loop model are presented.

As discussed previously, the SCR bridge can only affect the SCR firing angle once every 1/360 seconds. This sample and hold can be modeled as a pure delay, e^{-Ts} with period T equal to half the sample and hold period, or 1/720 seconds. Since the pure delay is not linear, and thus inconvenient to analyze, it is found that for this system a third order Padé approximation to the pure delay,

$$e^{-Ts} \approx \frac{N_{\text{delay}}(s)}{D_{\text{delay}}(s)} = \frac{1 - (T/2)s + (T/2)^2 \frac{s^2}{2!} - (T/2)^3 \frac{s^3}{3!}}{1 + (T/2)s + (T/2)^2 \frac{s^2}{2!} + (T/2)^3 \frac{s^3}{3!}}, \quad (\text{A.7})$$

provides sufficient accuracy for a wide range of model parameters.

In addition to the sample and hold, the firing circuit (Enerpro 6100) has response dynamics that can be modeled as a first order lead-lag followed by a first order low-pass filter closed with an integrator (VCO). See Figure A.1 for an illustration of the details of the firing circuit. The resulting transfer function ¹ for the firing circuit in the TB Macroamp has been calculated as

$$\frac{N_{fc}}{D_{fc}} \approx \frac{0.00210s + 1}{(0.00206s + 1)(0.00122s + 1)(0.00114s + 1)} \quad (\text{A.8})$$

Note that the time constants for each pole and zero in the firing circuit response (Eq. A.8) are of the order 1-2 ms. These times are comparable to the SCR delay time $1/720 \approx 1.39\text{ms}$. While the firing circuit is fast, it is not so fast that one can neglect its dynamic response.

Combining the elements described here with the first-order model described above produces an accurate model of the open-loop power supply. Validity of this model has been confirmed by experimental results and is discussed in section A.4.

¹Fax transmittal from Enerpro to ISI, dated October 11, 1992

A.3.3 Closed-loop Model

For typical arc operation the firing command is provided by feedback control through the Macroamp PI controller. This implements a PI control law consisting of a proportional gain, K_P , and an integral gain, K_I . Ignoring higher order dynamics, the controller issues the firing command

$$V_{fc} = K_P(I_c - I) + K_I \int (I_c - I) dt \quad (\text{A.9})$$

where I_c is the commanded current. As presently configured, the gains of this controller are set by adjusting resistors $R39$ and $R33$, where $K_P \simeq R39/10000$ and $K_I \simeq R33/460$. Additionally, there is a factor of 0.1 multiplying both gains, but this is typically accounted for in the model and not incorporated in the expression for K_P and K_I .

Substituting the controller output into Eq. A.5 and differentiating to eliminate the integral over time gives the closed-loop governing equation

$$L \frac{d^2 I}{dt^2} + (R_T + K_{ps} K_P) \frac{dI}{dt} + K_{ps} K_I I = K_{ps} K_P \frac{dI_c}{dt} + K_{ps} K_I I_c. \quad (\text{A.10})$$

If we assume that near some fixed operating current the inductance is constant, then the Laplace transform of the above equation yields

$$I(s) = \frac{K_{ps} K_P}{L} \left[\frac{s + K_I / K_P}{s^2 + (R_T / L + K_{ps} K_P / L)s + (K_{ps} K_P / L)(K_I / K_P)} \right] I_c(s). \quad (\text{A.11})$$

Here we have ignored the higher order dynamics specific to the controller and firing circuits to obtain a model which is analytically tractable. The resulting model yields three principal model parameters,

- $K_{ps} K_P / L$: The overall proportional gain
- R_T / L : 1/(time constant) for the basic R-I_c circuit
- K_I / K_P : Ratio of integral to proportional gain

The first parameter, $K_{ps} K_P / L$, is the overall proportional gain of the system. Increasing this gain (e.g., by increasing $R39$) results in a faster system, which is generally good. However, if the gain is increased too much the system will become unstable. If $R_T / L < 0$ then the system will also be unstable if this gain is too small.

The second model parameter, R_T / L , is inversely proportional to the time constant for the open-loop system. Furthermore, if $R_T / L < 0$ then the open-loop system is inherently unstable and must be run with feedback control. Since the the arc resistance typically depends on the operating conditions, R_T / L is not adjustable through controller design. However, one can add ballast resistance to the circuit to increase R_T / L .

The final model parameter, K_I/K_P , determines the magnitude of the integral compensation (relative to proportional compensation). When K_I/K_P is large, the controller response to differences between the measured and commanded current will be large – the longer the differences persist, the larger the controller response. This parameter strongly influences the ability of the system to reject low frequency disturbances. Generally larger K_I/K_P providing better disturbance rejection. However, as with the system gain, if K_I/K_P is too large for a given R_T/L the system is unstable. The design goal is set K_I/K_P as large as possible while maintaining a stable closed-loop system with sufficiently high damping.

In addition to the proportional and integral gains, the controller circuit has two lowpass filters. One is on the output firing command, and is a first order filter with a time constant of approximately 1 ms. This lowpass is not negligible since it is almost as slow as the firing circuit delay. A second low-pass filter is in series with the proportional gain section of the controller, and has a time constant of approximately $R39 \times 0.1 \times 10^{-6}$. Since $R39$ is typically $1k\Omega$ or less, this low-pass is relatively fast ($\geq 10kHz$) and does not significantly affect the model. These details are included in the final model.

A complete model for the closed-loop arc power supply has been implemented using ISI tools (MATRIX_X and SystemBuild). Figure A.2 illustrates a typical SystemBuild diagram. Note that the “Sample and Hold” block can be modeled exactly in SystemBuild, but comparisons have demonstrated that the linear third order Padé approximation to a pure delay is sufficiently accurate and, since it is linear, is more easily analyzed. As will be discussed below, the model accurately predicts both the open-loop and closed-loop performance of the arc power supply (with and without ballast).

A.4 Experimental Results

A.4.1 Open-Loop Tests

A number of experiments have been done to characterize the power supply parameters described in the previous section. There are three major parameters, K_{ps} , R_I , and $L(I)$, that are fixed for a given power supply. These parameters were measured for the TB Macroamp power supply equipped with the Enerpro 6100 firing circuit.

To measure the power supply parameters, K_{ps} , R_I , and $L(I)$, the arc was replaced by ballast resistance. This configuration provides a stable system ($R_T/L > 0$) and allows the firing circuit to be commanded with a constant voltage (i.e., open-loop). The terminal voltage, V_t , and current, I , were measured as a function of firing command, V_{fc} . Since we expect $V_{ps} = V_{ps}(V_{fc})$, the gain and internal resistance can be determined using Eq. A.1. Specifically, if $V_t(V_{fc})$ and $I(V_{fc})$ are measured for two loads, R_1 and R_2 , then the internal

18-Aug-93

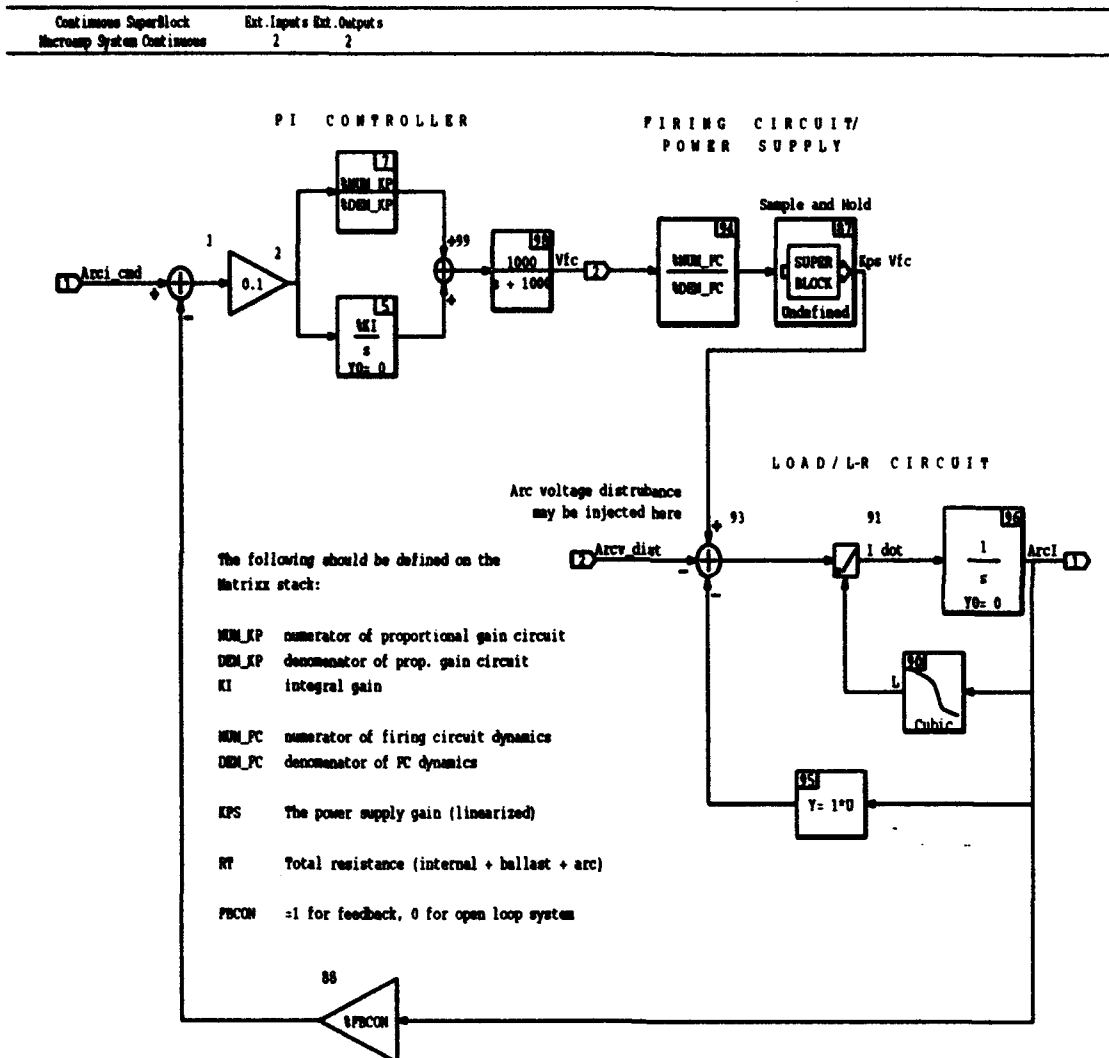


Figure A.2: SystemBuild block diagram of the nonlinear arc power supply model.

resistance can be calculated at each firing command, V_{fc} , using the formula

$$R_I(V_{fc}) = \frac{V_{t,1}(V_{fc}) - V_{t,2}(V_{fc})}{I_2(V_{fc}) - I_1(V_{fc})}. \quad (\text{A.12})$$

Here the subscripts 1 and 2 denote results measured with load resistance 1 and 2. The primary assumption here is that V_{ps} is only a function of V_{fc} , so that $V_{ps,1} = V_{ps,2}$.

Once R_I is known, the power supply gain, K_{ps} , can be computed directly from the formula

$$K_{ps} = \frac{d(V_t + IR_I)}{dV_{fc}} \quad (\text{A.13})$$

Using this approach on the TB power supply gives an estimate of $R_I \approx 2\Omega$ and $K_{ps} \approx 800$. Figure A.3 shows typical V_t versus V_{fc} results for 4, 8, and 12 ballast tubes (each tube is about 0.7 Ohms). Note that the maximum V_{fc} for each curve is limited by operating current ($\sim 80\text{A}$).

Measuring the inductance $L(I)$ is only slightly more complicated once the ISI toolset and AC100 are connected to the power supply. A step change in the firing command is issued by the AC100 and the voltage and current responses are recorded. A simple least square fit of the open-loop model to the current response provides an estimate of $L(I)$. Figure A.4 shows several open-loop step responses and the corresponding model fit. These results were obtained using 12 tubes of ballast ($\sim 8.5\Omega$) and no arc. It is interesting to note that there is approximately 3 ms delay from the time the firing command step is issued ($t = 0$) until the current begins to respond. This delay is the combined effect of the SCR sample and hold and the firing circuit dynamics.

Figure A.5 shows the resulting estimate of $L(I)$ obtained by fitting the open-loop model to the measured step responses. The inductance varies from approximately 0.11 H at 35 A to approximately 0.02 H at 72 A. A cubic spline fit, shown as a solid line in Figure A.5, is used to model the continuous function $L(I)$.

Having specified R_I , K_{ps} , and $L(I)$, the open-loop model is completely specified. To test this hypothesis a series of experiments were performed to compare the model with open-loop responses of the system with an arc. As discussed in previous sections, the arc cannot be run open-loop unless R_T/L is positive. Thus, 4 tubes of ballast were added to the circuit and the response to open-loop steps was measured. Figure A.6 shows both the measured responses and the responses predicted by the open-loop model. The agreement between the model and measured response is very good.

A.4.2 Closed-loop Tests

Once the open-loop model is known, the closed-loop model is obtained by characterizing the current controller. As discussed above, the controller model is a simple proportional-plus-

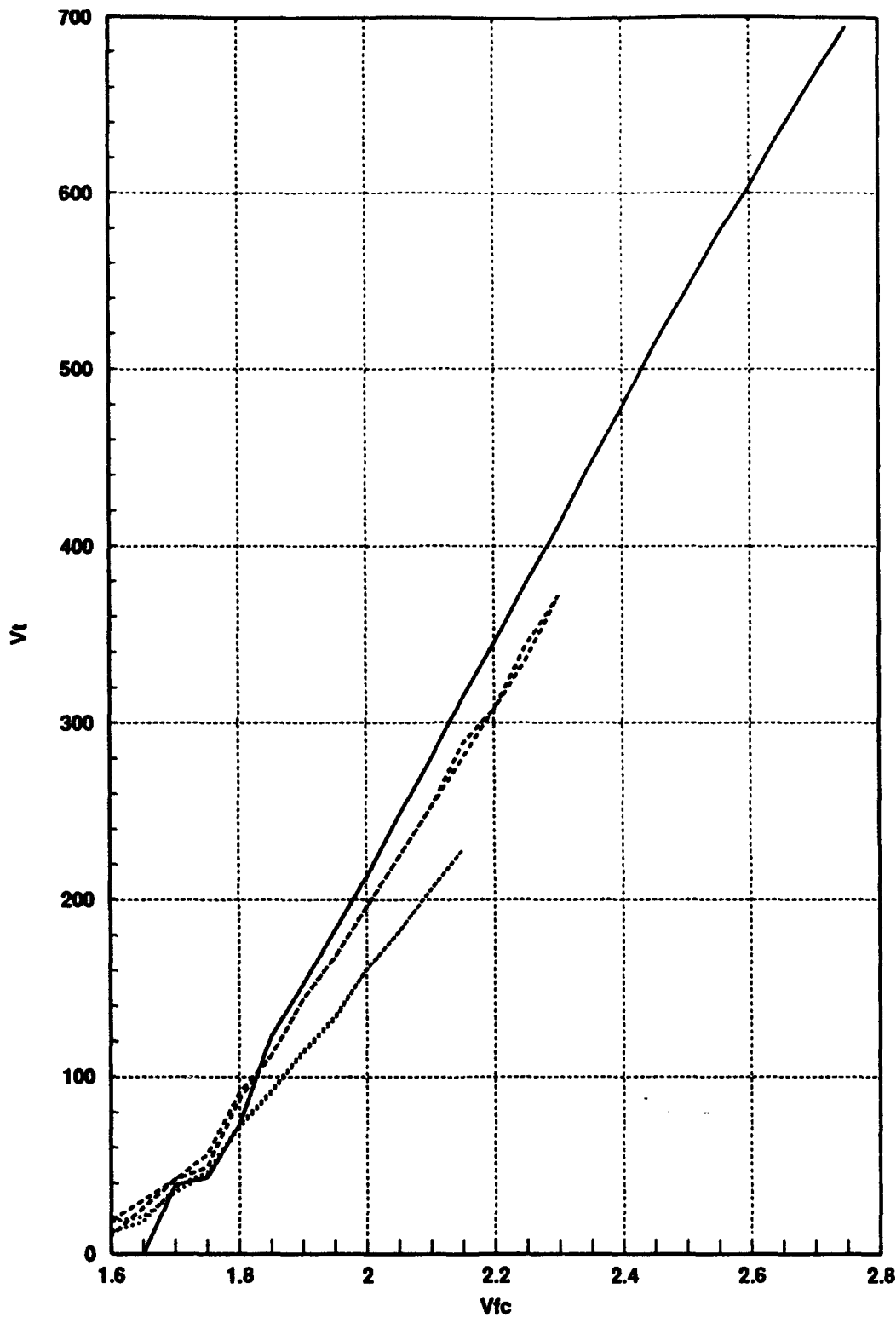


Figure A.3: Terminal voltage as a function of firing command voltage for 4, 8, and 12 tubes of ballast resistors and no arc.

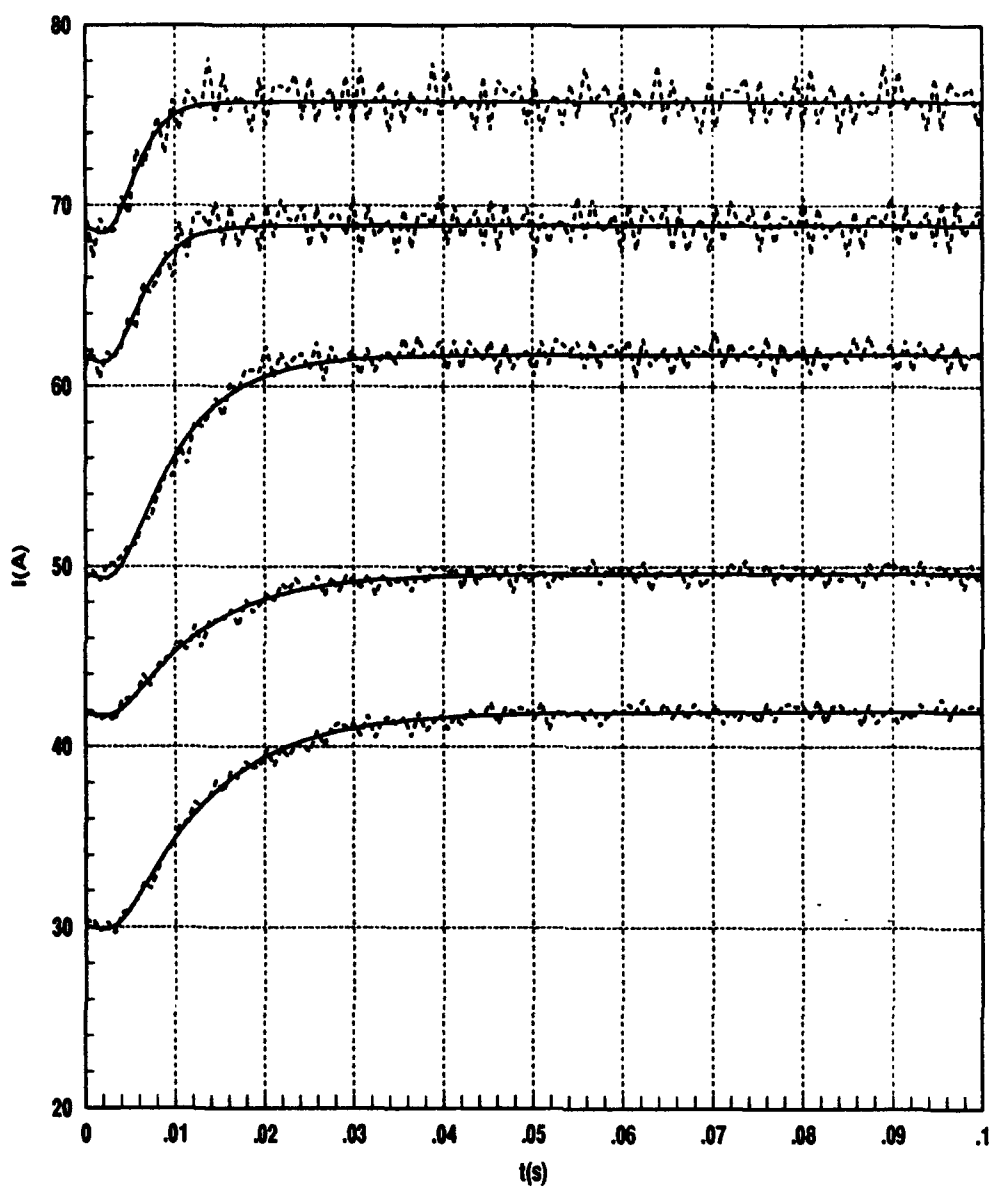


Figure A.4: Open-loop step response of the Macroamp power supply with 12 tubes of ballast resistors and no arc.

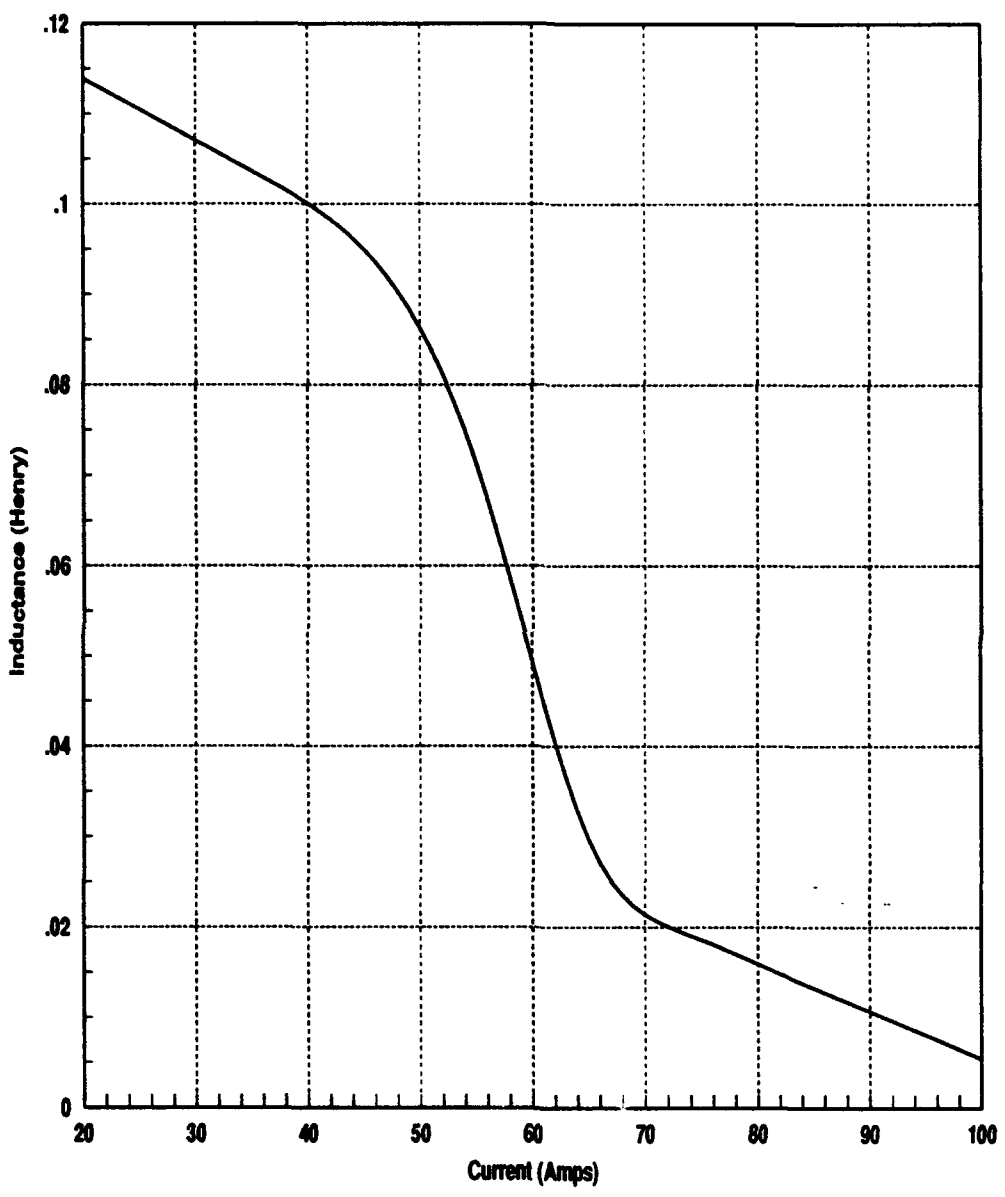


Figure A.5: Variation of output inductance with current

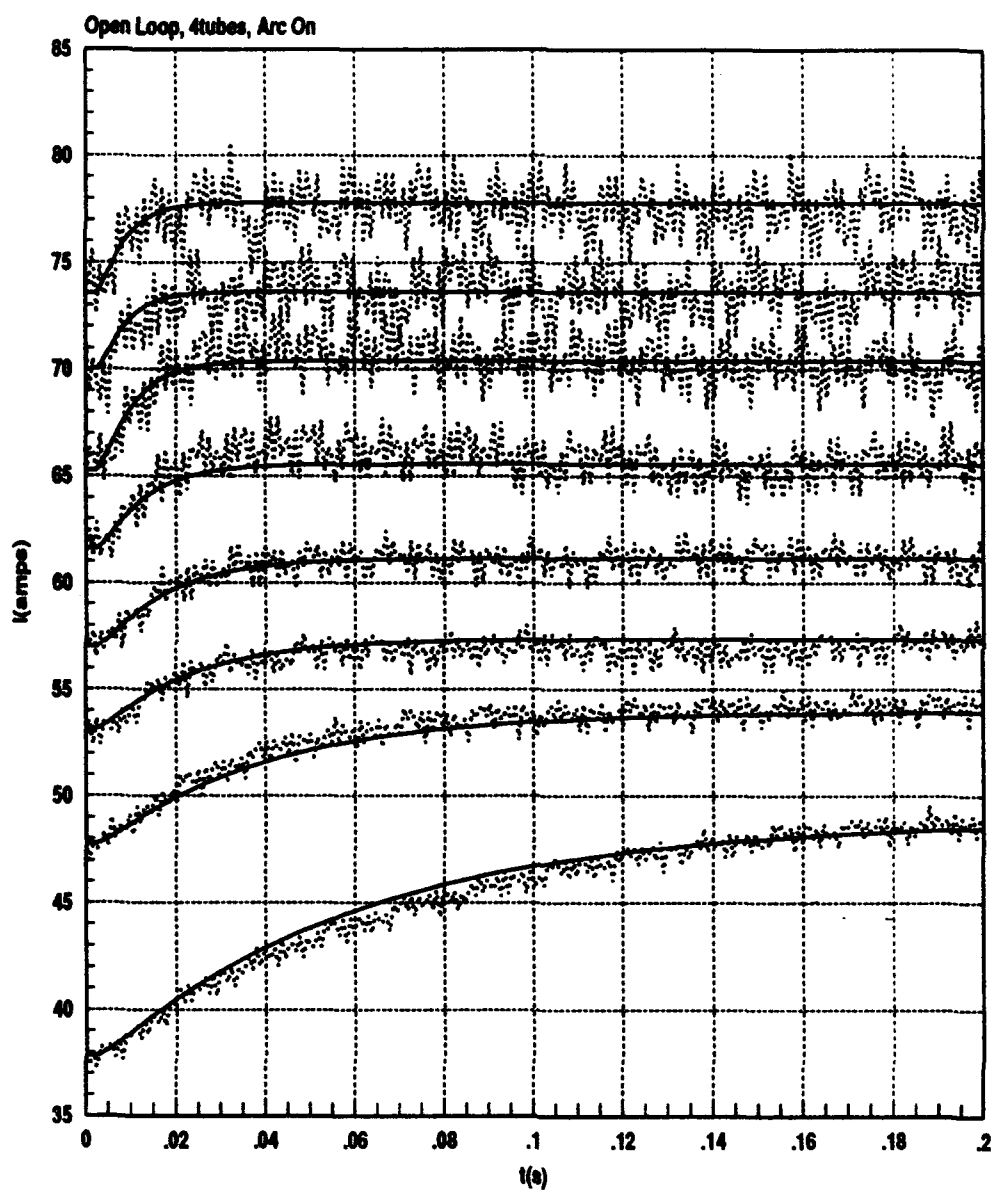


Figure A.6: Comparison of measured and simulated response of arc power system in open-loop mode of operation with the arc on and four tubes of ballast resistors.

integral gain, with two low-pass filters. To verify the accuracy of the closed-loop model the controller gains, K_p and K_i , were measured and current command steps were issued to the controller. The resulting current responses were recorded and compared to model predictions. Figures A.7 and A.8 show typical results.

Figure A.7 shows the current response for an arc with 4-tubes of ballast ($\sim 2.8\Omega$) and Figure A.8 shows the response for ballastless arc operation. In all cases the model predicted the response of the system with suitable accuracy. The response time of the system decreases significantly with increasing current, both with and without ballast. Most of this decrease is attributable to the decrease in L . When the open-loop system is stable (4-tubes) the response time varies but the overshoot and ringing in the response is not too bad. However, when the open-loop system is unstable (no ballast) the closed loop response is too slow at the low current and has too much overshoot at high current. For comparison, the step starting near 55 or 60 A has a very good response. The rise time is fast relative to steps at lower currents and the overshoot is small relative to steps at higher currents.

It is evident from these results that the power supply model outlined here is reasonably accurate. The model predictions agree well with experiments in all cases tested to date. The effects of changing the controller gains have been measured and the agreement with the model persists. Experiments have also been done with gain settings near the edge of the stability envelope and the model performed well.

A.5 Gain Tuning and Controller Design

One of the goals of this work is to provide a rational approach to tuning the power supply – preferably an approach that allows tuning either automatically (through gain scheduling) or by manually setting the gains on the power supply controller. In this section the gain requirements are discussed and the stability boundary and “best” gain settings are provided. Experimental results are presented to demonstrate the effect of using fixed controller gains.

In the previous sections, it was established that there are three important model parameters, R_T/L , $K_p, K_P/L$, and K_I/K_P . Based on this model one can predict the stability boundary for the continuous range of these parameters. Such an analysis was done for values of K_I/K_P of 10, 20, and 40, and the result is a stability boundary in the $(K_p, K_P/L, R_T/L)$ plane. Figure A.9 shows the three stability boundaries for the three settings of K_I/K_P . If, for a given gain, $K_p, K_P/L$, the value of R_T/L is to the left of the stability boundary then the system is uncontrollable. If $R_T/L < 0$ then there are minimum and maximum allowable gain settings. If $R_T/L \geq 0$ then there is only a maximum allowable gain. Figure A.9 also shows that the system becomes stable for a wide range of R_T/L if K_I/K_P is smaller. As was discussed previously, this does not imply that smaller K_I/K_P is better, since reducing K_I/K_P degrades the ability of the controller to compensate for disturbances. The design

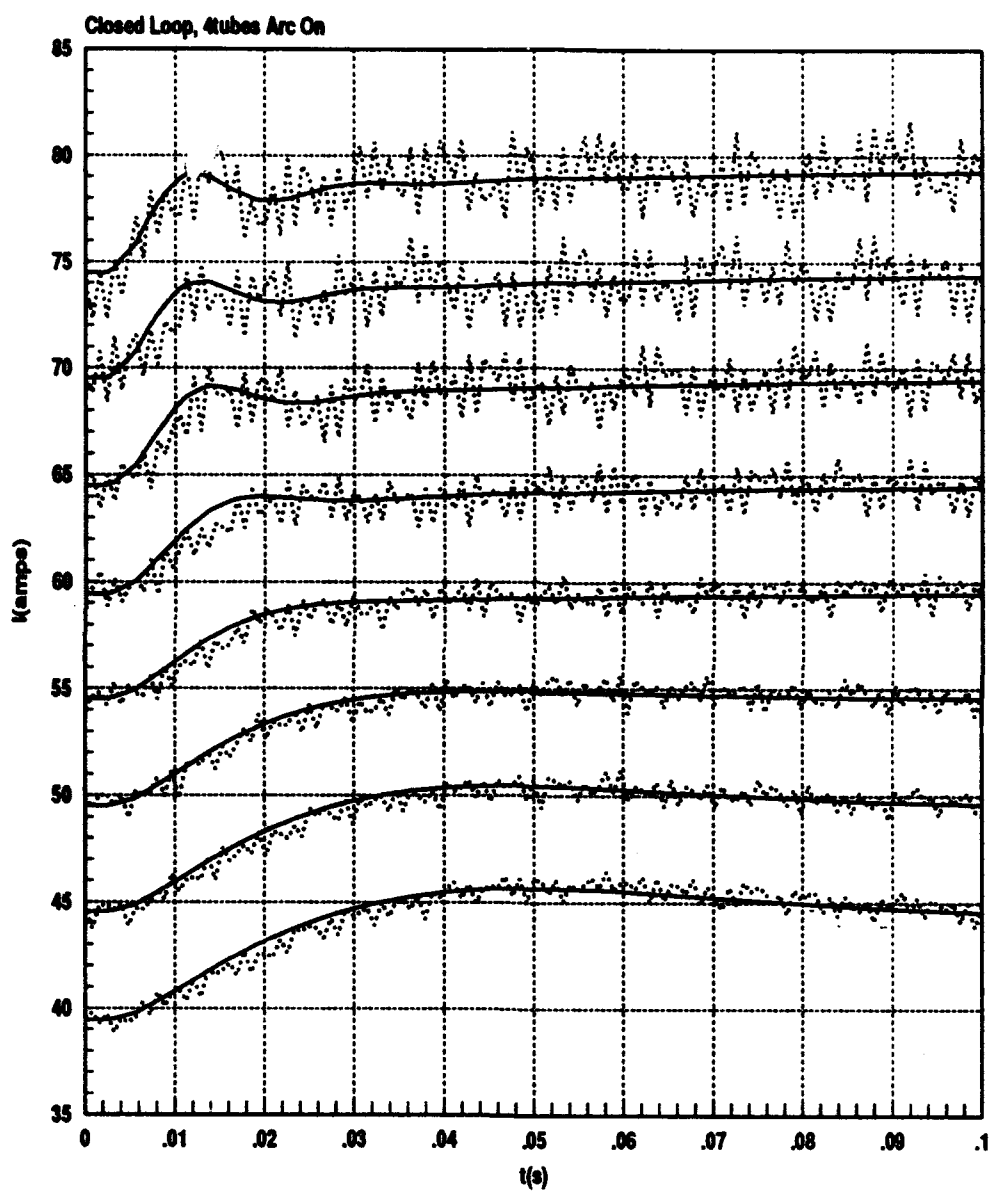


Figure A.7: Comparison of measured and simulated response of arc power system in closed-loop mode of operation with the arc on and four tubes of ballast resistors.

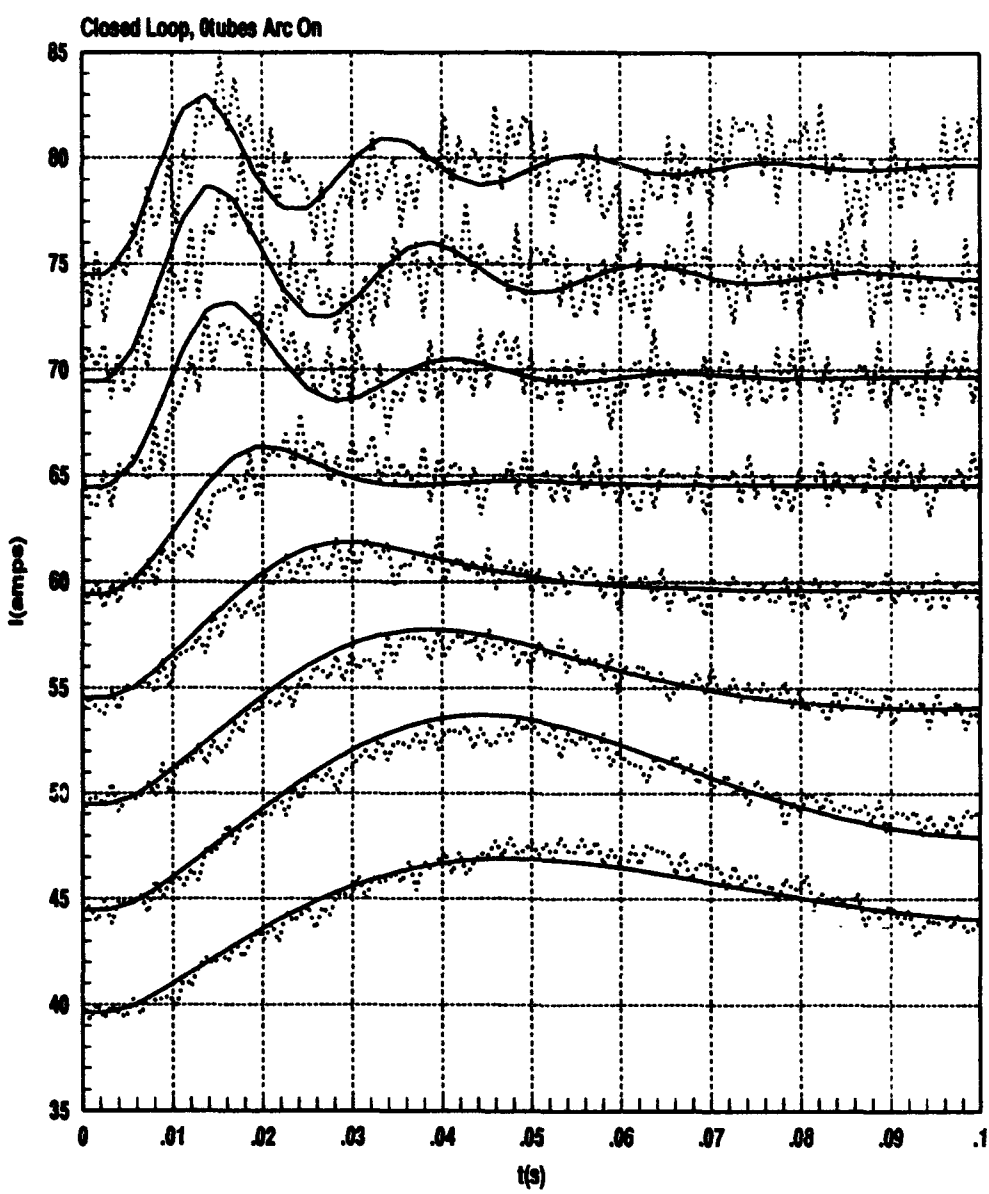


Figure A.8: Comparison of measured and simulated response of arc power system in closed-loop mode of operation with the arc on and no ballast resistors.

criterion should be to have the largest K_I/K_P that will ensure stable and robust control.

In addition to the stability boundary, Figure A.9 shows the preferred gain setting, labeled as "best". The "best" curve is the gain setting that produces acceptable overshoot while maintaining an acceptably fast response. The three arrows mark the values of R_T/L for each K_I/K_P setting that allow an "optimal" 0.7 damping ratio. If R_T/L is to the left of the arrow for a given K_I/K_P the damping ratio will be less than 0.7. In non-control terminology, this means that the overshoot of a step response will be acceptable for R_T/L to the right of the arrow, but will increase as R_T/L is decreased to the left of the arrow.

Figure A.9 reveals that the "best" line is approximately horizontal, apart from a small decrease with increasing R_T/L . This suggests that a good first step in automatic gain scheduling would be to fix K_I/K_P on the Macroamp controller and add another proportional gain, K_{gs} , that varies with current to compensate for $L(I)$. Specifically, the gain schedule should be designed such that $K_{gs} \propto 1/L(I)$. A more sophisticated approach would be to compensate for changes in R_T/L either by measuring R_T real-time or by measuring it for a set of operating parameters.

A.5.1 Gain Tuning Example

To illustrate the use of Figure A.9 in setting the controller gains, consider a specific example of its use to tune the TB power supply.

Suppose the arc resistance, R_A , is measured to be -2.5Ω for a particular operating condition where the system is to be run at 70 amps. From Figure A.5 we see that $L \simeq 0.02$ H. If $R_I = 2.0\Omega$ and the arc is run ballastless, then $R_T = R_A + R_I = 2.0 - 2.5 = -0.5\Omega$ and R_T/L is approximately -25. Based on Figure A.9, this system may be run at approximately $K_I/K_P = 30$ and still have a damping ratio of 0.7. If K_I/K_P was larger, say 40, the system would still be stable, but there may be too much overshoot.

For the "best" gain setting the product $K_p, K_P/L$ should be approximately 1200. Since $K_p \simeq 800$ and $L \simeq 0.02$, K_P should be set to $1200/0.02/800 \simeq 0.03$. To set $K_P \simeq 0.03$ one must adjust R_{39} to a value of $10000 \times K_P \simeq 300\Omega$. Since R_{39} is a 10k trimmer this is a very touchy adjustment.

The next step is to adjust K_I until $K_I/K_P \simeq 30$, or $K_I \simeq 0.9$. Recall that K_I is set by adjusting R_{33} , where $K_I \simeq R_{33}/460$. For this example we must set $R_{33} \simeq 414\Omega$.

Suppose that the PI gains are set as described in this example, but during operation R_A decreases to -4.6Ω , a very low, but not unreasonable value. The system gain $K_p, K_P/L$ is still 1200, but R_T/L decreased to -130 – the system becomes uncontrollable. If R_a does not drop all the way to -4.6Ω , but simply decreases significantly, the system may remain stable

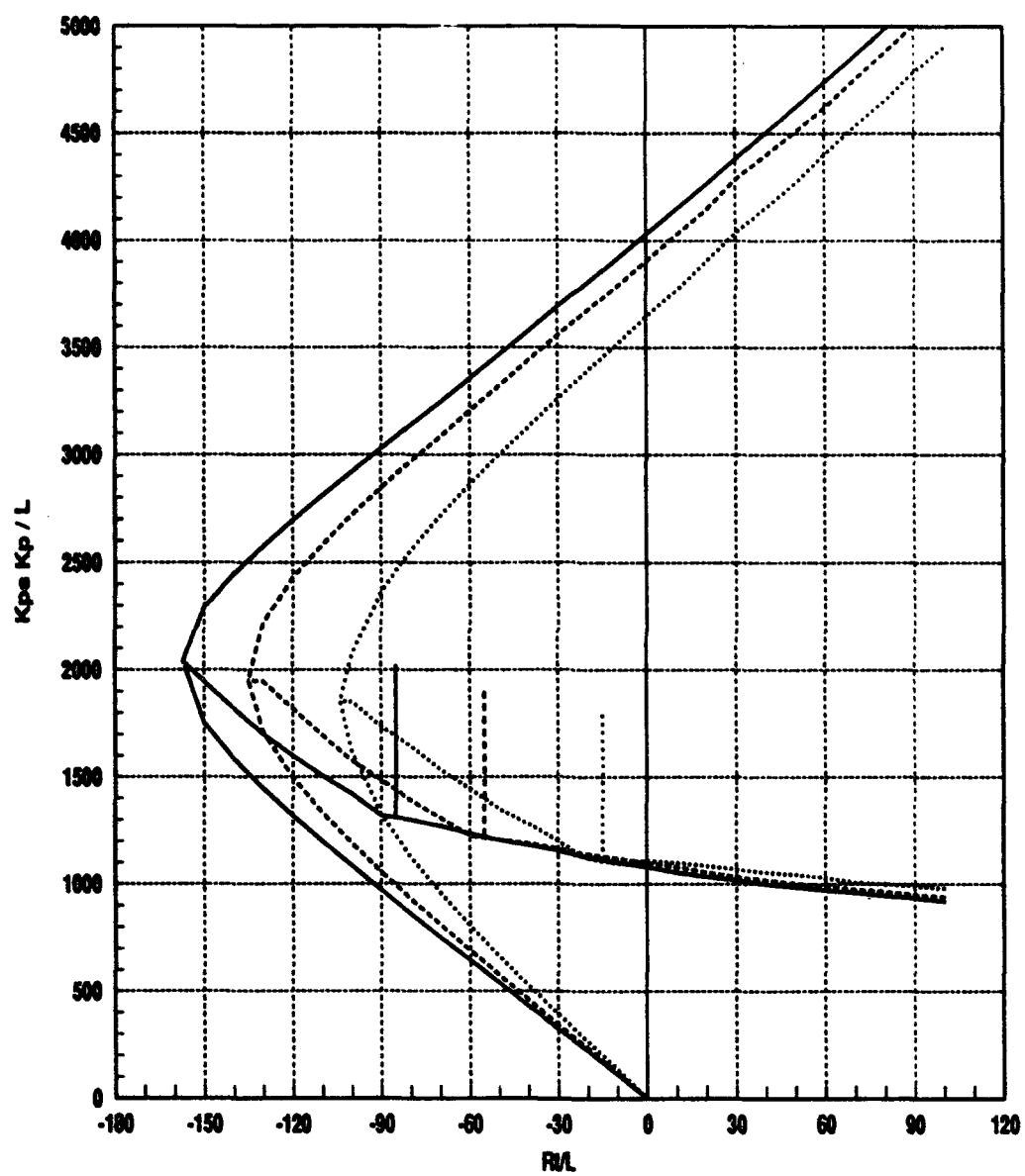


Figure A.9: Stability boundary of the closed-loop arc power system.

but performance will be poor, with disturbances causing ringing and oscillation.

Anticipating the above scenario, the operator decides to add ballast resistance to prevent the system becoming unstable when R_a falls to -4.6Ω . The decision is made to add one ballast tube, or 0.71Ω . This modification increases R_T/L to -94.5 . Unfortunately, this operating point very near the stability boundary – an undesirable situation. When the operating point is near the stability boundary the regulation will be very poor. In addition, drift of temporary changes in any of the operating parameters could cause the system to go completely unstable. If the operator added 2-tubes (1.42Ω) then R_T/L would be -59 and the system would remain stable. Increasing the ballast to 3-tubes gives $R_T/L \simeq -23.5$ and the system is well regulated.

As a final example, suppose the operator wants to set the fixed gains to operate over the entire current range from 30 to 75 A and for three sets of operating conditions, A, B, C. Figure A.10 shows three typical ranges of R_a for the TB arc. Using the spline fit of $L(I)$ shown in Figure A.5 and $R_I = 2\Omega$, one can compute R_T/L . Figure A.11 shows the results for the three operating conditions versus operating current. We see that R_T/L remains within the range $-50 < R_T/L < 20$. At low current $R_T/L \geq -30$ and at high current $R_T/L \geq -50$. At low current L is large so the fixed gain setting must be chosen so that $K_{ps}K_P/L > 400$ or so. At high current L is small so $K_{ps}K_P/L < 3500$. Therefore, the operator should choose $500 * L_{low}/K_{ps} < K_p < 3500 * L_{hi}/K_{ps}$, or $0.055 < K_p < 0.088$. This analysis suggests that the proportional resistor, $R39$, should be set somewhere between 550 and 800Ω . The integral gain, K_I , should be set to approximately 30 or 40 times K_P .

Experience has shown that in fact $R39 \simeq 600\Omega$ is a suitable setting for a wide range of operating conditions. Adopting this value, Figure A.12 illustrates the range of operating gains for the R_T/L data of Figure A.11. It is evident that K_P either twice or half the present value would not allow operation over the full current range. If $K_P \simeq 0.03$ was used, as determined in the previous example, then the system would be stable at higher currents, and perhaps stable at 40 A, but would become uncontrollable near 45 A where R_T/L decreases to approximately -25.

Finally, an example of the step response for $R39 = 600\Omega$ is presented in Figures A.7 and A.8. Note that R_T/L curve A crosses zero near 60 A. Also, the A curve in Figure A.12 crosses the “best” line near $R_T/L = 0$. Therefore, based on this analysis the best performance is for currents near 60 A. This is the same conclusion one reaches by observing the step responses in Figure A.8.

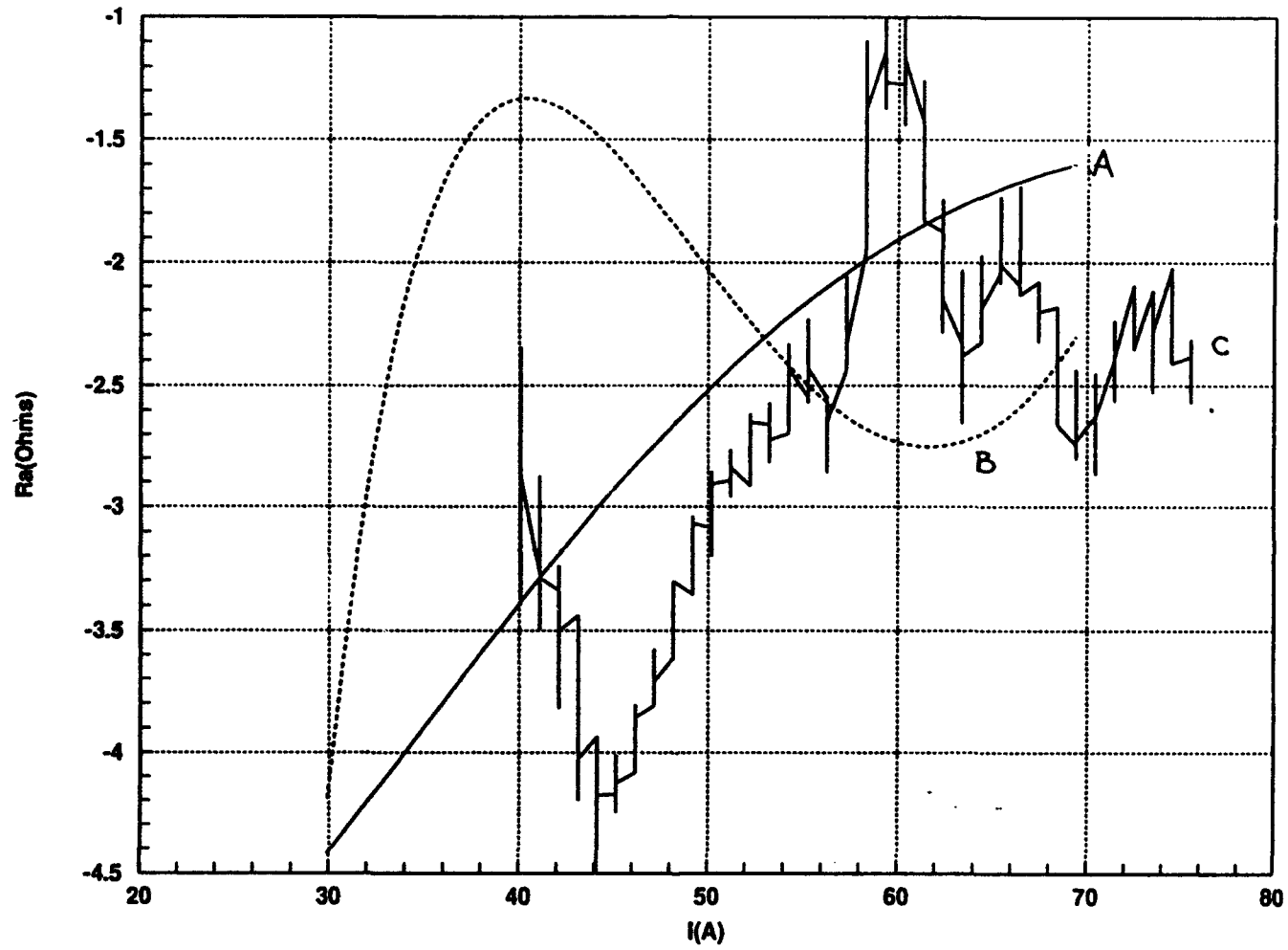


Figure A.10: Arc resistance for three different operating conditions.

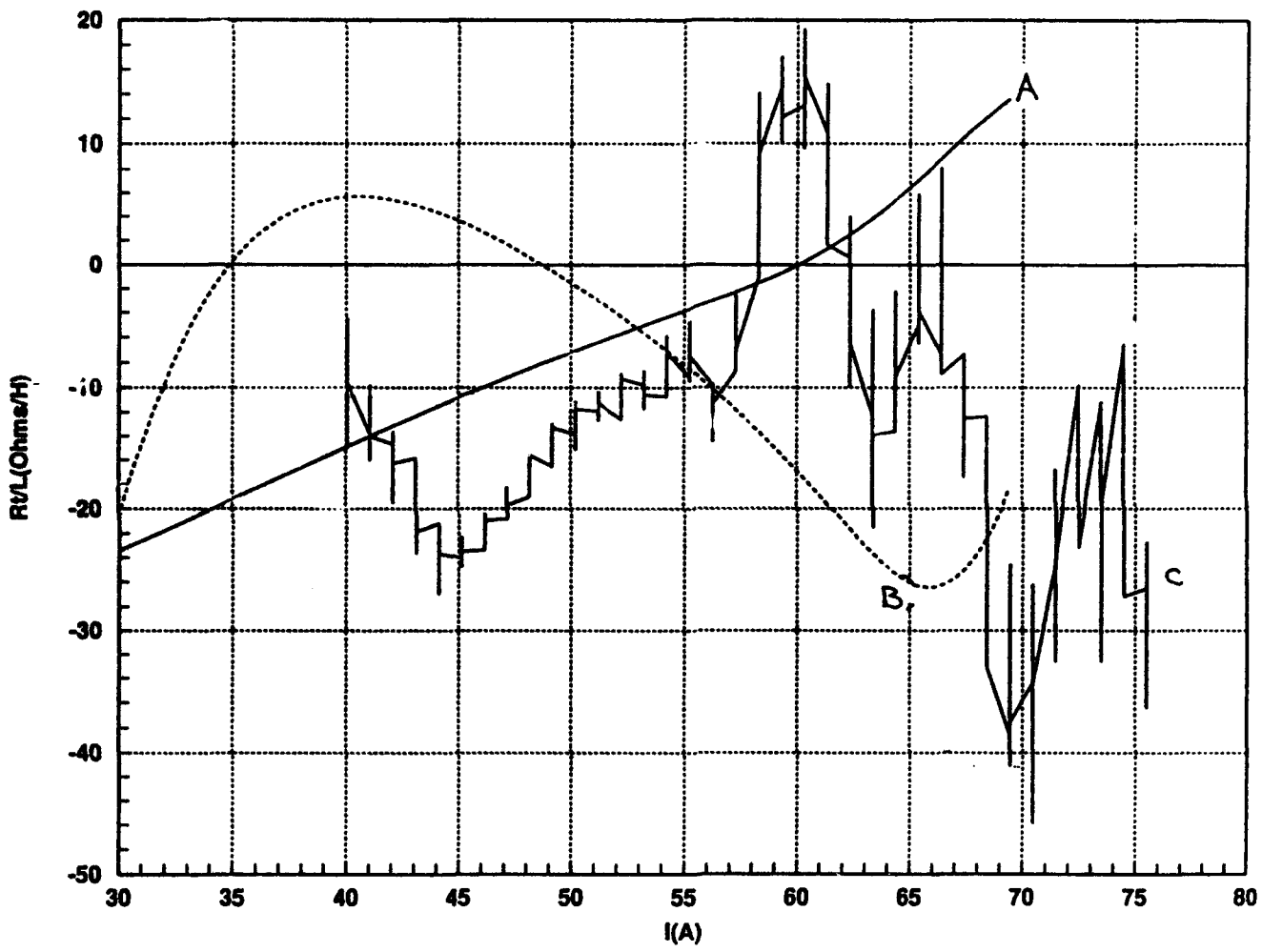


Figure A.11: R_T/L for arc resistance shown in Figure A.10.

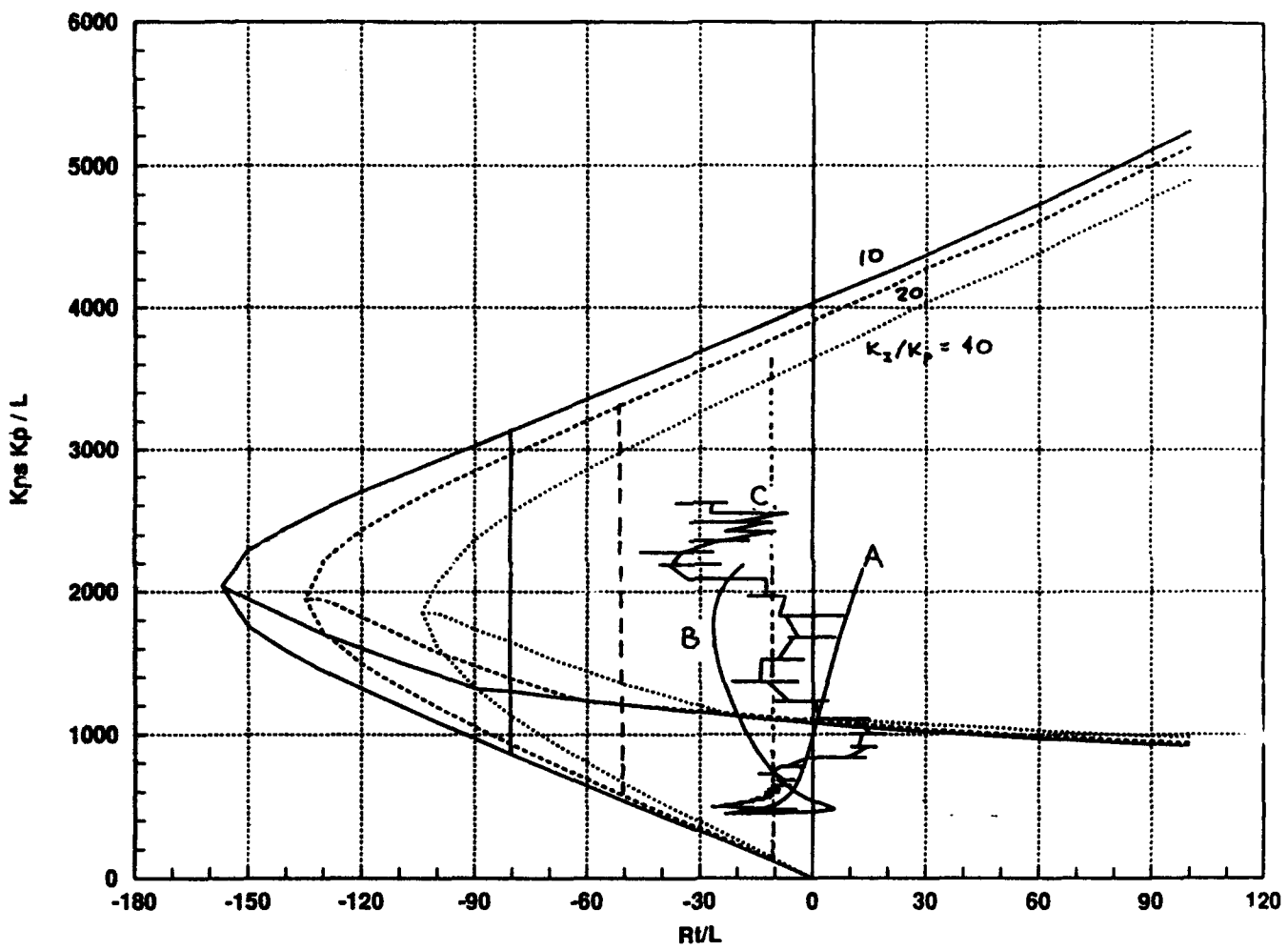


Figure A.12: Range of operating gains for the R_T/L data of Figure A.11.

A.6 Summary

An accurate model for the arc power supply has been developed and compared to experimental results. The agreement between the model and the measurements is very good for a wide range of operating conditions and power supply parameters. Analysis of the model has led to a better understanding of the power supply tuning requirements, and the range of parameters that allow stable operation. The model has been of considerable value for developing alternative control strategies and in aiding our understanding of the problems associated with the fixed gain controller. Also, the knowledge gained from this effort is expected to lead to more appropriate specifications when purchasing new power supplies.

Appendix B

Substrate Temperature Control

Substrate temperature is an important deposition condition since it affects diamond film quality and yield. Production experience shows that changes in temperature of 10°C or more can cause the film to separate from the substrate and be destroyed. Also, thermal gradients across the film during growth are believed to be a source of film buckling after removal from the substrate. Hence, substrate temperature control is important for process repeatability and high yield. Performance of the existing controller implemented in the Honeywell Series 9000 is too slow to adequately regulate temperature.

To address this problem, ISI has designed a faster controller to regulate the substrate temperature. The limitation on the speed of this loop comes from not wanting arc power to significantly overshoot. Overshoot would help drive the thermocouple measurement to the desired temperature more quickly, but at the cost of larger temperature excursions at the diamond/gas interface. Predictive models and alternative sensor configurations that could remove this limitation are under investigation. This appendix briefly describes the substrate temperature model and controller design and shows the comparison between expected and actual results.

B.1 Model

The model for the substrate temperature response to arc power is simply a first order ordinary differential equation:

$$\tau \frac{d}{dt}T = T + KP_A$$

where τ is the time constant and K is the steady-state change in substrate temperature for a unit step change in arc power input and are determined empirically. The assumptions for validity are that the diamond and substrate are homogeneous, that the response covers a

sufficiently small range that linearity holds, and that arc power is actuated much faster than the temperature responds. Figure B.1 shows an overlay of substrate temperature response to a 1 kilowatt step arc power input with the model. The agreement is more than sufficient to support controller design.

B.2 Controller Design

For this simple a differential equation, a proportional plus integral (PI) controller is adequate. This is an attractive result, as a PI controller can be implemented in the Honeywell Series 9000. Designing a controller using such a simple model is desirable and straight forward and allows the controller gains to be set directly from simply measured system response parameters. The continuous time case solution can be solved using Laplace transforms, and for sufficiently high execution rates of the control law, this is sufficient. The only design constraint is the acceptable amount of overshoot in the power response.

Figure B.2 shows the substrate temperature and arc power response to a 10°C temperature command doublet. The temperature response is exponential, as designed, with a time constant of approximately 30 seconds with the down step slower than the up step. This is because of different mechanisms for heating and cooling, and is not accounted for in the model. Note that the arc power goes almost immediately to the required steady state value, with minimal fall back. This is desirable, as the thermocouple measures a temperature below the film, and overshoot in arc power could cause a transient over-temperature in the film when the controller responds to a disturbance. Any further speedup in the temperature response, will have to be achieved with overshoot in arc power. A joint study between ISI, Norton and Sandia is underway to develop a better understanding of the temperature response of the film. This model will be used to provide a better metric for acceptable arc power overshoot levels.

To test the performance of the new model-based controller, step changes were made in the magent current. This induces changes in arc power and arc performance. Figure B.3 shows the substrate temperature response to these disturbances for the original Honeywell controller and the new model-based controller. It is evident that the new controller is able to reduce both the magnitude of temperature fluctuation and the time taken to remove it. For the original controller there is a 9°C temperature excursion which takes about 5 minutes to remove. On the other hand, with the new controller the excursion is reduced to 5°C and takes about 30 seconds to remove. This is a very acceptable result and a significant improvement.

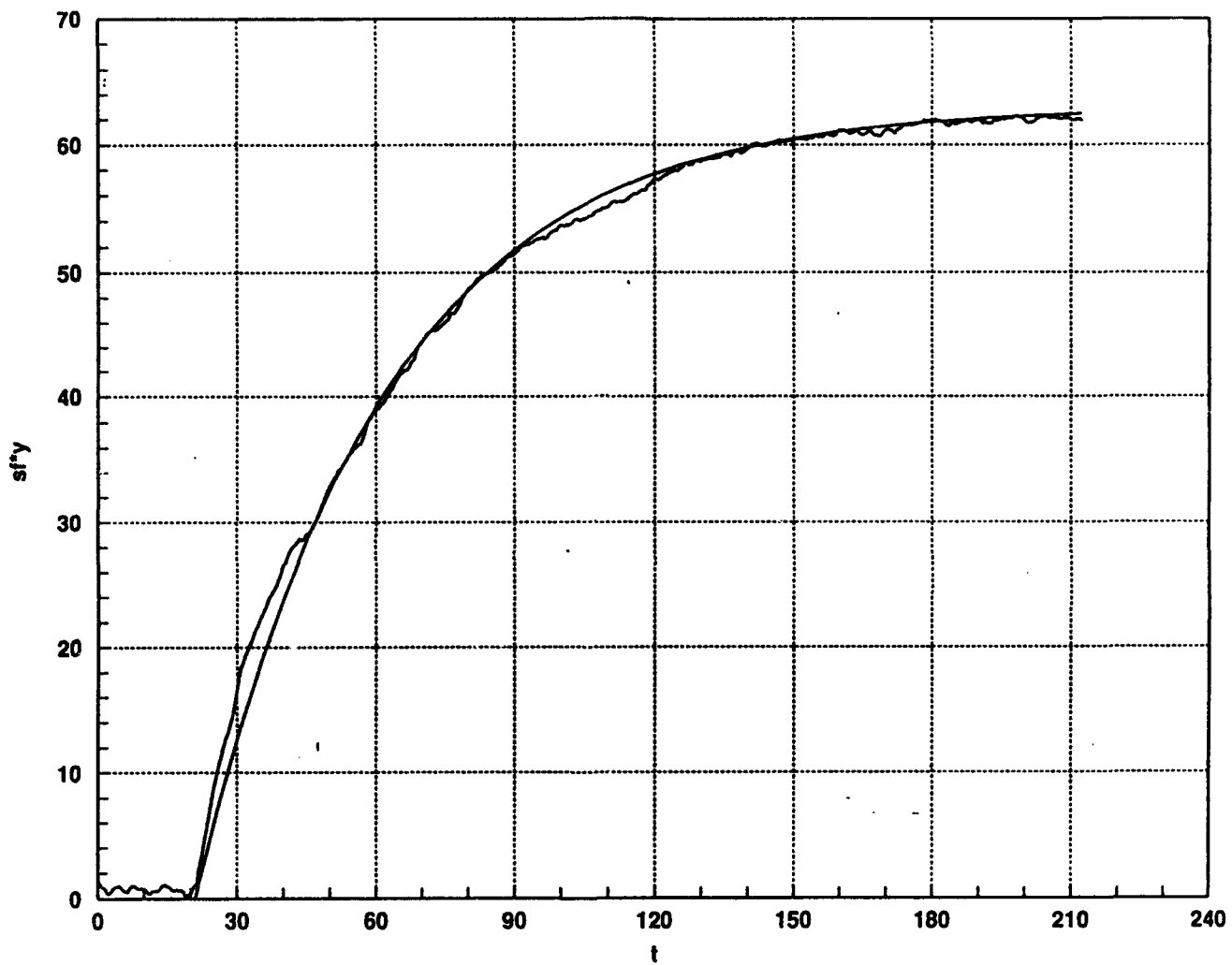


Figure B.1: Open-loop response for substrate temperature.

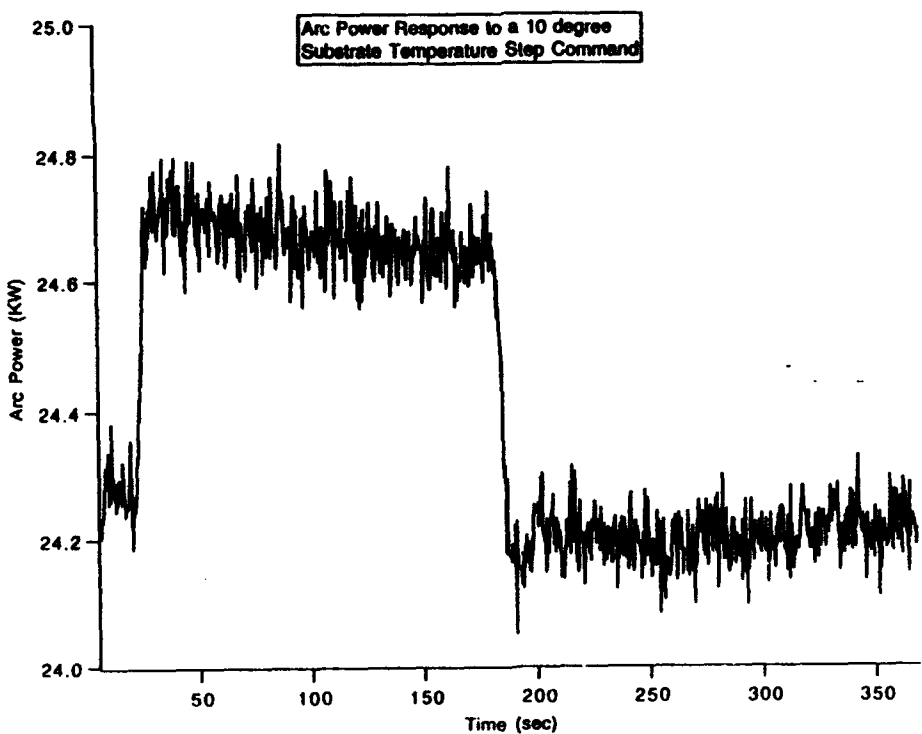
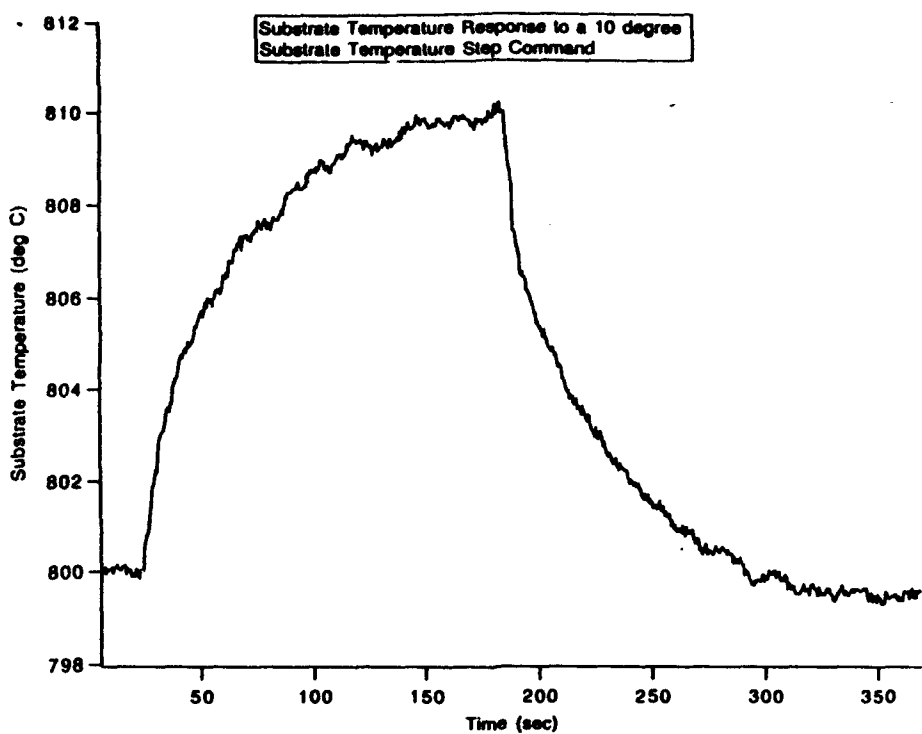


Figure B.2: Closed-loop response for substrate temperature using the new model-based controller implemented in the Honeywell 9000.

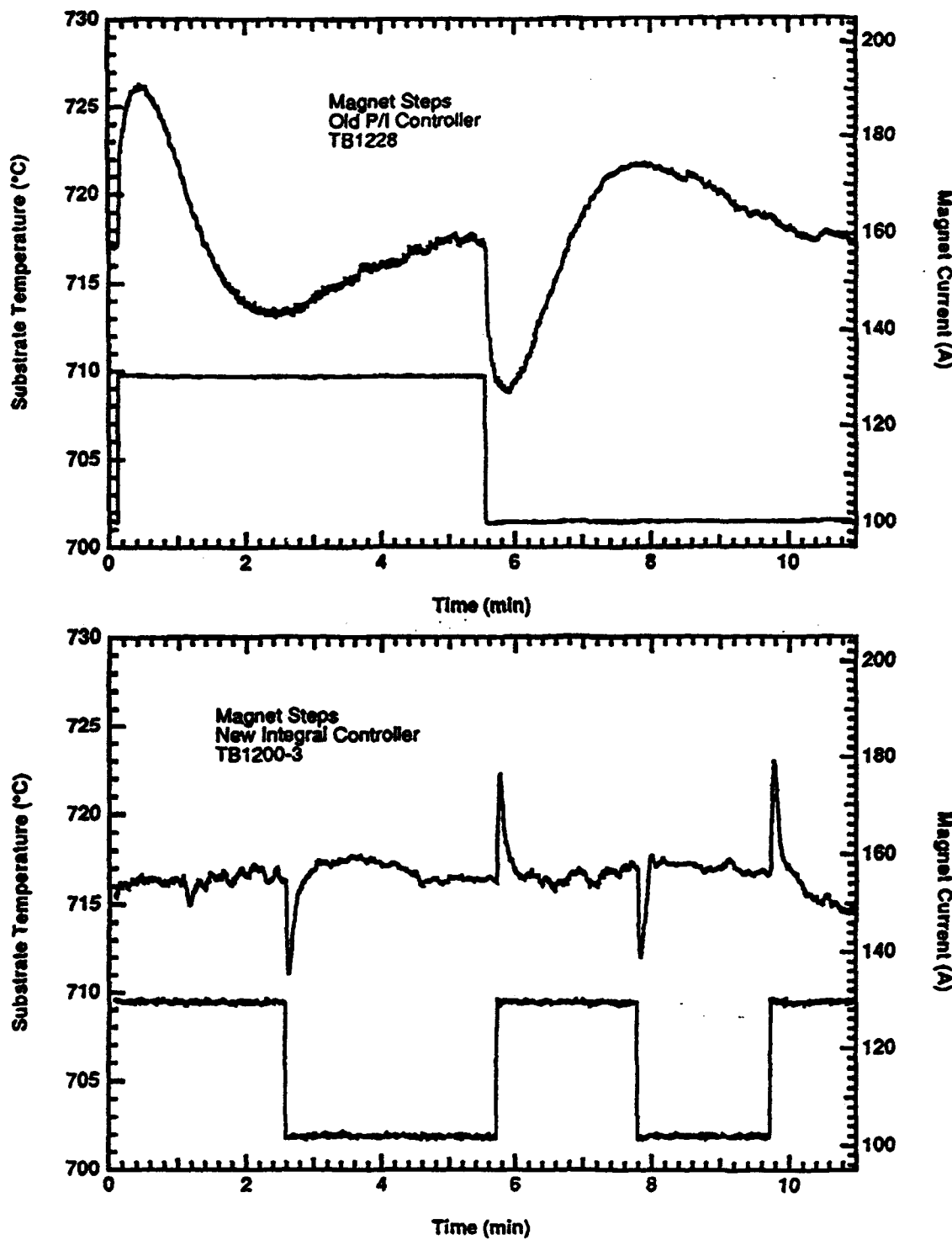


Figure B.3: Comparison of closed-loop response of substrate temperature with the old Honeywell controller and the new model-based controller.

Appendix C

Chamber Pressure Control

C.1 Introduction

Chamber pressure affects many deposition conditions, including process chemistry and arc resistance. Hence, it is desirable to minimize pressure variations. The chamber pressure is regulated by a PI controller implemented in the Honeywell Series 9000. In the past, gains for this controller have been determined on an ad hoc basis. ISI has determined that this controller is slow to respond to changes in setpoint. This indicates that the controller will not be able to adequately regulate the chamber pressure. To address this issue, ISI has developed a model-based controller. This appendix describes an analytical model of the chamber pressure, experimental validation of this model, and design of a controller based on this model.

C.2 Chamber Pressure Model

The basis for a model of chamber pressure is the ideal gas law, applied to a constant-volume tank, as shown below.

$$P = nRT/V \quad (\text{C.1})$$

where P is tank pressure, n is number of moles of gas in tank, V is the volume of the tank, R is the ideal gas constant, T is bulk temperature of tank gases.

Under steady-state conditions, the mass flow out of the tank, \dot{m}_{out} , must equal the mass flow into the tank, \dot{m}_{in} . However, when the mass flow into or out of the tank changes, we can use the time derivative of the ideal gas law to determine the tank pressure dynamics.

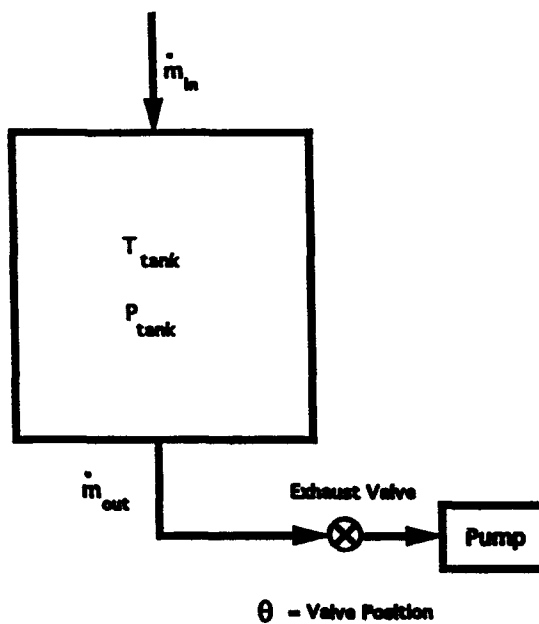


Figure C.1: Tank pressure model

Differentiating equation (1) with respect to time gives

$$\dot{P} = \dot{n}RT/V \quad (C.2)$$

$$= (\dot{m}_{in} - \dot{m}_{out})R_{H_2}T/V, \quad (C.3)$$

where $(R/.002016\text{kg/mole}H_2) = R_{H_2} = 4150 \text{ kJ/kg-K}$. In this expression, we assume that the tank contents are almost entirely hydrogen, since the methane injected during normal deposition is on the order of 0.1% by mass of the hydrogen flow. Therefore, the ideal gas constant for hydrogen, R_{H_2} , is used here. The tank is assumed to be of fixed volume, 0.8 m^3 . Further model validation will determine the volume of the exhaust piping prior to the butterfly valve. This volume will then be added to the known volume of the tank.

For the model to be useful, an expression for \dot{m}_{out} is needed, as all the other parameters can be either commanded or measured. In order to characterize \dot{m}_{out} , a series of tests was performed. In these tests, steady-state chamber pressure was recorded for various hydrogen inflow rates, for a fixed valve opening, θ . The tests were repeated for different valve openings. Results of these test are shown in Figure C.2. The data indicates that, for a given valve position θ , the pressure in the tank is proportional to the mass flow into the tank, i.e.,

$\dot{m}_{in} \propto P$. At steady-state, the mass flow into the tank is equal to the mass flow out. Hence, assuming constant external pressure, the mass outflow can be written as:

$$\dot{m}_{out} = f(\theta)P \quad (C.4)$$

where $f(\theta) = \frac{\Delta\dot{m}_{in}}{\Delta P}$ for a given θ . A second order polynomial expression in θ has been fit to the 6 experimentally acquired values of $f(\theta)$:

$$f(\theta) = -1.142571 \times 10^{-4} + 6.28501 \times 10^{-6}\theta - 3.18559 \times 10^{-8}\theta^2 \quad (C.5)$$

where θ is in units of % open, and $f(\theta)$ is in units of kg/second-torr. This polynomial fit is shown in Figure C.3. We can now rewrite Equation C.3 as

$$\dot{P} = (\dot{m}_{in} - f(\theta)P)R_{H_2}T/V \quad (C.6)$$

which expresses the relation between valve position and chamber pressure. The valve position itself depends on a valve position command, θ_c . At present, a measurement of the valve position is not available. Hence, we assume that the valve position is governed by a simple first-order differential equation.

$$\dot{P} = -f(\theta)\frac{R_{H_2}T}{V}P + \dot{m}_{in}\frac{R_{H_2}T}{V} \quad (C.7)$$

$$\dot{\theta} = -\alpha\theta + \alpha\theta_{cmd} \quad (C.8)$$

Parameters

- P : Measurable
- R_{H_2} : 4150 J/kg K (Assume all gas H₂)
- V : Assume 1.0 m³ tank & piping. Use experimental time constant to better estimate.
- T : Assume bulk temperature of all gas in tank and piping is 250°C. Use experimental time constant to better estimate.
- \dot{m}_{in} : Measurable at mass flow controller. Unknown dependence on P .
- α : Unknown valve dynamics. Possible hysteresis in valve. Assume $\alpha = 2$.
- $f(\theta)$: Empirical characterization of mass flow out of tank. If insufficiently accurate, recharacterize about operating range of interest (30 % - 40% open).

C.3 Model Validation

The initial parameters remaining to be validated in the model were V , the tank volume, and T , the bulk temperature of the gas. While the volume of the tank itself is known to be 0.8 m^3 , V in this model is defined to be the volume of the tank as well as all piping upstream of the exhaust valve. Similarly, the temperature of the arcjet itself can be measured using emission spectra, and is on the order of 2500 K. However, after impinging on the deposition substrate, most of the heat is quickly removed from the gas by a large heat exchanger, and the gas is near room temperature when it exits the tank. The parameter T to be identified is therefore the average temperature of the whole bulk of gas in the tank.

On 26 May, 1993, several chamber pressure experiments were performed on the Technion B reactor. In the first set, performed with no arc present, the valve position command was held constant while the flow command to the arc hydrogen mass flow controller was changed. Several step responses of approximate magnitude 100 standard liters per minute were performed within an operating range of 250 - 400 standard liters per minute. In the next set of steps, the mass flow to the tank was held constant while the valve command was stepped. These two sets of experiments were then repeated with an arc present. In all cases, the pressure, temperature, hydrogen flow, and valve command were recorded at 200 Hz. A representative response (chamber pressure, upstream hydrogen flow response, and upstream hydrogen voltage command) is shown in Figure C.4. As may be seen, the time constant of the mass flow response to a setpoint change was on the order of 3 seconds, which was slower than expected, and on the order of the time constant of the pressure response.

These open-loop steps were compared with the predicted model response in order to test the validity of the model, and more accurately identify some key model parameters. Recalling Equation C.7, if the valve command is held constant, the expression for chamber pressure is

$$\dot{P} = -f(\theta) \frac{R_{H_2} T}{V} P + \dot{m}_{in} \frac{R_{H_2} T}{V} \quad (\text{C.9})$$

From this expression, the steady-state change in pressure in response to a step in arc hydrogen flow is given by $1/f(\theta)$, which is evident from the definition of $f(\theta)$. The open-loop time constant for the pressure response to an arc hydrogen step is given by $\tau = \frac{V}{f(\theta) R_{H_2} T}$. Since for the cold-flow steps the temperature of the gases is known to be room temperature, we can use the experimentally determined time constant to determine the actual value of V , the tank volume.

For the experimental arc hydrogen steps performed, however, the mass flow controller dynamics are on the same order as those of the tank pressure response. Therefore, the hydrogen flow cannot be approximated as a step input, and the time constant of the pressure

response cannot be simply read off a plot. A least-squares approach was therefore taken to finding the volume of the tank from the cold-flow cases. The upstream hydrogen flow was acquired from the mass flow controller, and was input to the full nonlinear SystemBuild implementation of the model (Figure C.5). The model was then run several times, allowing the tank volume to vary from 0.5 to 1.5 m³. For each run, the rms error between the experimentally acquired and modelled chamber pressure was calculated. For these step responses, a tank volume of 1.1 m³ yielded the minimum rms error (Figure C.6).

A similar approach was taken to find the bulk gas temperature for the hot-flow steps. In these cases, the model parameter V was set to the previously-determined value of 1.1 m³, and T was allowed to range from 0 to 100 °C. In most of these cases, minimizing the rms error in the pressure response led to a bulk temperature of approximately 70 °C (Figure C.7).

C.4 Controller Design

While the full nonlinear state equations are given in Equations C.7 and C.8, a model linearized about an operating point is desired for control design. We rewrite the state equations as:

$$\dot{P} = -f(\theta)cP + c\dot{m}_{in} \quad (C.10)$$

$$\dot{\theta} = -\alpha\theta + \alpha\theta_{cmd} \quad (C.11)$$

where

$$c = R_{H_2}T/V \quad (C.12)$$

To linearize around the (constant) operating point $P = P_0$, $\theta = \theta_0$, and $\dot{m}_{in} = \dot{m}_{in0}$, we define

$$\Delta P = P - P_0 \quad (C.13)$$

$$\Delta\theta = \theta - \theta_0 \quad (C.14)$$

$$\Delta\dot{m}_{in} = \dot{m}_{in} - \dot{m}_{in0} = \dot{m}_{in} - f(\theta_0)P_0 \quad (C.15)$$

$$\Delta\theta_{cmd} = \theta_{cmd} - \theta_{cmd0} = \theta_{cmd} - \theta_0 \quad (C.16)$$

The linearized equations are

$$\dot{\Delta P} = -cf(\theta_0)\Delta P - c\partial f(\theta_0)/\partial\theta_0 P_0 \Delta\theta + c\Delta\dot{m}_{in} \quad (C.17)$$

$$\dot{\Delta\theta} = -\alpha\Delta\theta + \alpha\Delta\theta_{cmd} \quad (C.18)$$

or

$$\frac{d}{dt} \begin{bmatrix} \Delta P \\ \Delta \theta \end{bmatrix} = \begin{bmatrix} a & b \\ 0 & -\alpha \end{bmatrix} + \begin{bmatrix} c & 0 \\ 0 & \alpha \end{bmatrix} \begin{bmatrix} \Delta \dot{m}_{in} \\ \Delta \theta_{cmd} \end{bmatrix} \quad (C.19)$$

where

$$a = -c(k_0 + k_1 \theta_0 + k_2 \theta_0^2) \quad (C.20)$$

$$b = -c(k_1 + 2k_2 \theta_0)P_0 \quad (C.21)$$

If \dot{m}_{in_0} is specified, either P_0 or θ_0 is chosen to define the desired operating point, and the steady-state equation $\dot{P}_0 = 0$ is solved to yield the other value.

The time constant of the linearized pressure response to a mass flow step at an operating point is given by $1/a$. Linearizing at three different operating pressures (5, 10, and 15 torr) at a hydrogen mass flow rate of 300 slpm, and a temperature of 400K yields time constants that vary by 200% (1 second to 3 seconds). Clearly, a controller designed for one operating condition will not be valid at another unless it is robust.

Using the expressions developed in the previous section, a model linearized about $P_0 = 10$ torr, $T = 400K$, and $\dot{m}_{in} = 300$ slpm was obtained. Based on this linearized model, a proportional-plus-integral controller was designed. The closed-loop response of the implementation of this controller on the AC-100 is shown in Figure C.8. Although both the damping and bandwidth were designed to be considerably greater, the model mismatch resulted in an underdamped closed-loop system. This model was especially sensitive to mismatch in the characterization of $f(\theta)$. The polynomial fit for $f(\theta)$ was obtained from a data set containing only 3 points between $\theta = 30\%$ and $\theta = 40\%$. Since the steady-state valve position for the usual range of operating pressures and flows lies within this range, and since $f(\theta)$ is especially sensitive to changes in θ in this region, further characterization is warranted. Both the model mismatch and valve characterization issues are being addressed in a new contract with Norton Diamond Film, and controller response has already been significantly improved as a result.

C.5 Further Issues

The hysteresis in the valve is the single most important issue to be explored. As may be seen from Figure C.9, the actual valve position depends on the direction of movement, as well as the valve command. Since the $f(\theta)$ term, and thus the open-loop time constant, is so sensitive (up to 100% change for a 5% change in θ), it is imperative that the valve position signal be acquired, and the valve dynamics characterized. Better characterization of the valve dynamics will also help in determining the appropriate controller bandwidth.

Also of importance is the definition of control objectives. If speed of response and disturbance rejection are the priorities, then further characterization of the valve dynamics and their effect on the tank pressure is warranted. If control need not be fast, but should maintain a setpoint with less than a given percent deviation, then more sensor study is warranted, as the noise on the chamber pressure signal is seen to be ± 0.3 torr. A gain scheduled controller is also an option if control is needed during both startup and normal deposition, as the pressure model is highly nonlinear with respect to the valve position.

FIG 1

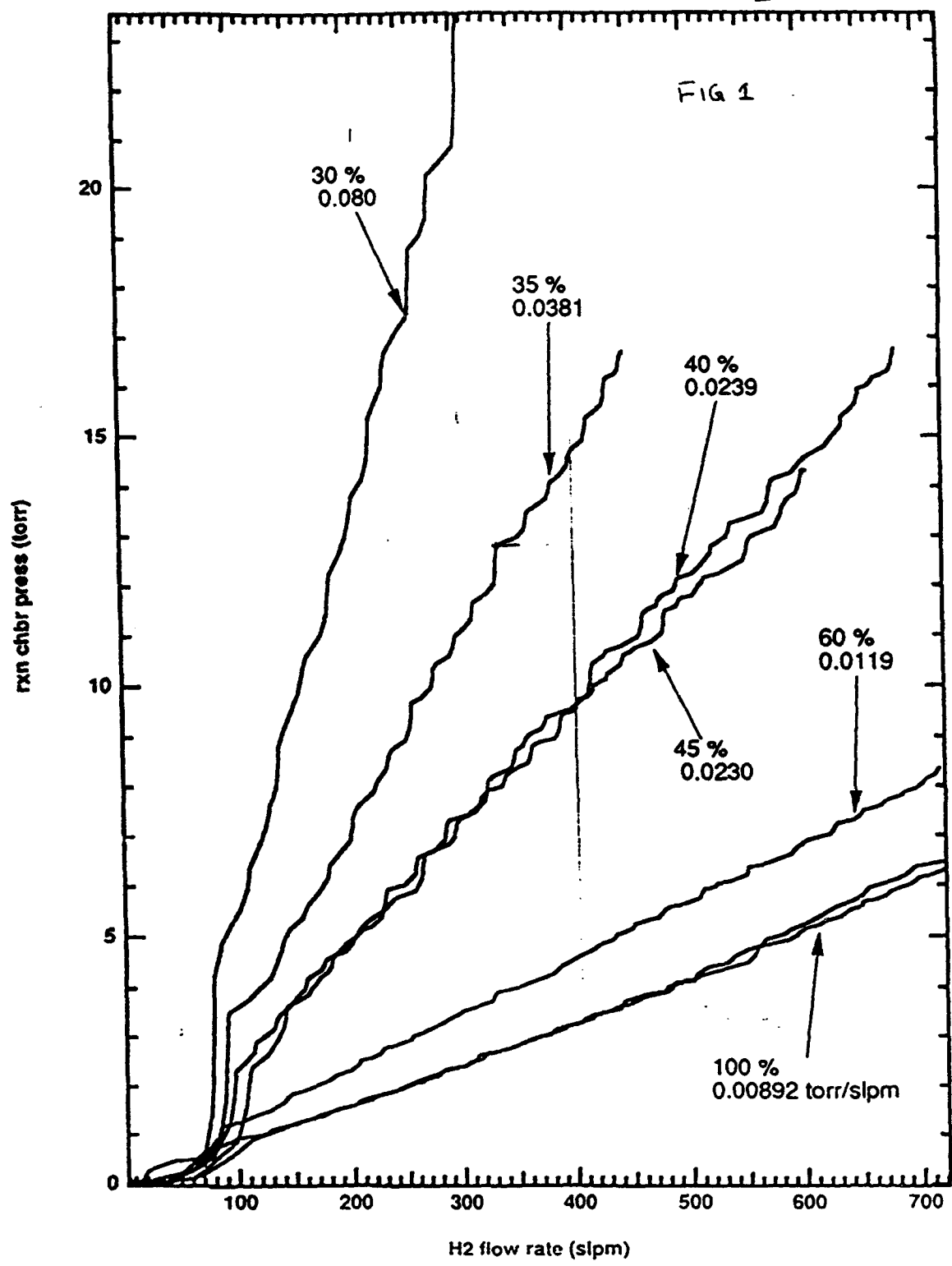


Figure C.2: Steady-state chamber pressure as a function of hydrogen inflow for various valve openings.

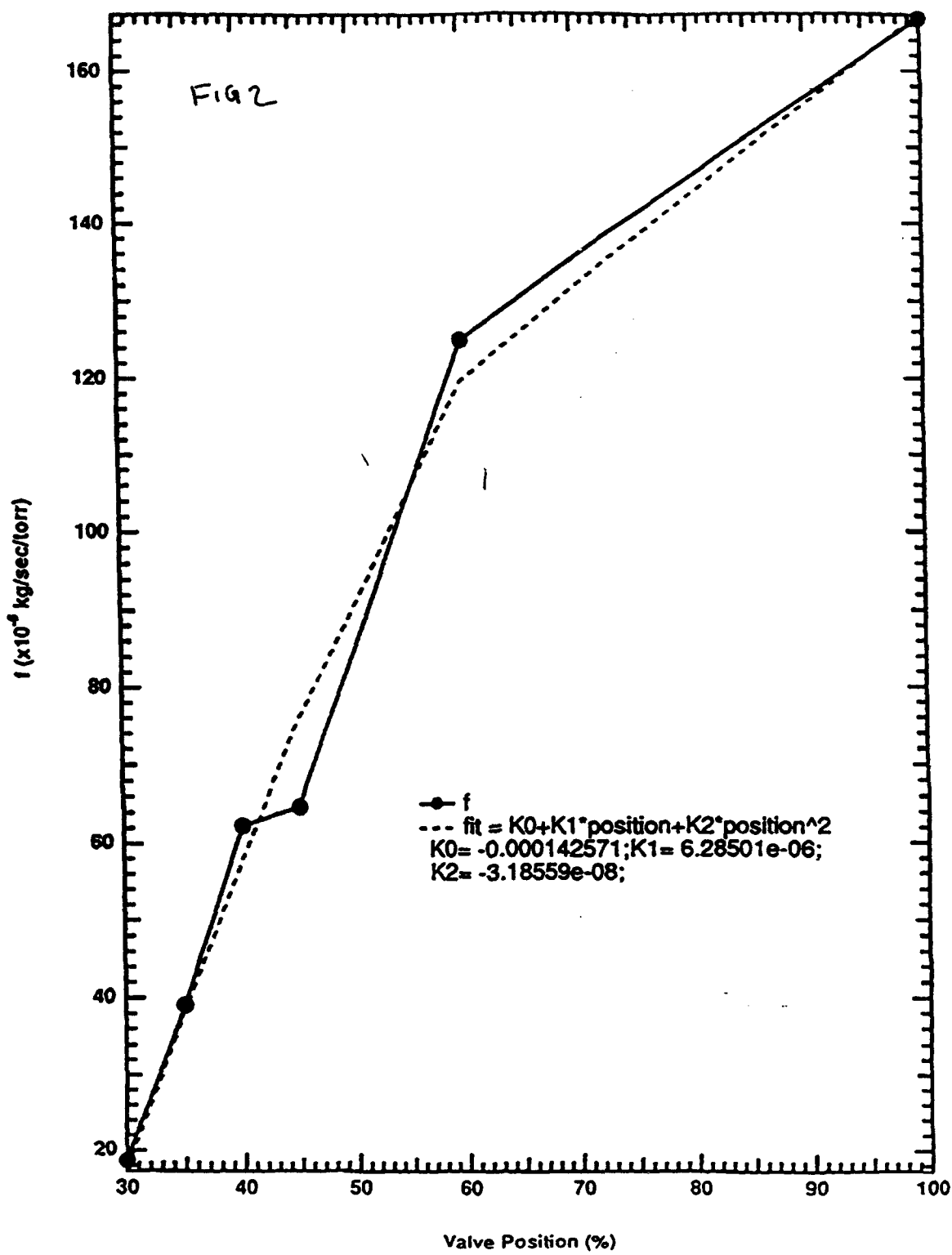


Figure C.3: Measured and a third-order fit for $f(\theta)$.

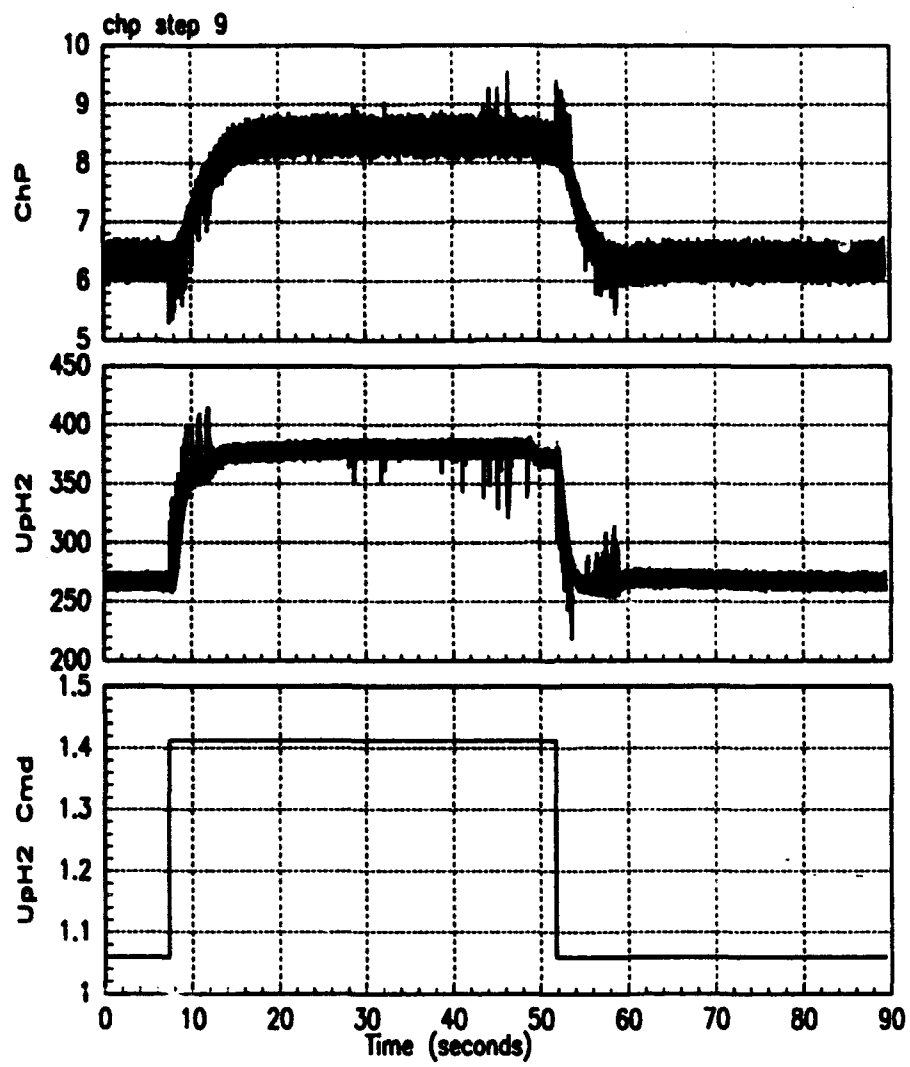


Figure C.4: Open-loop response for chamber pressure for step change in hydrogen inflow.

29-Aug-93

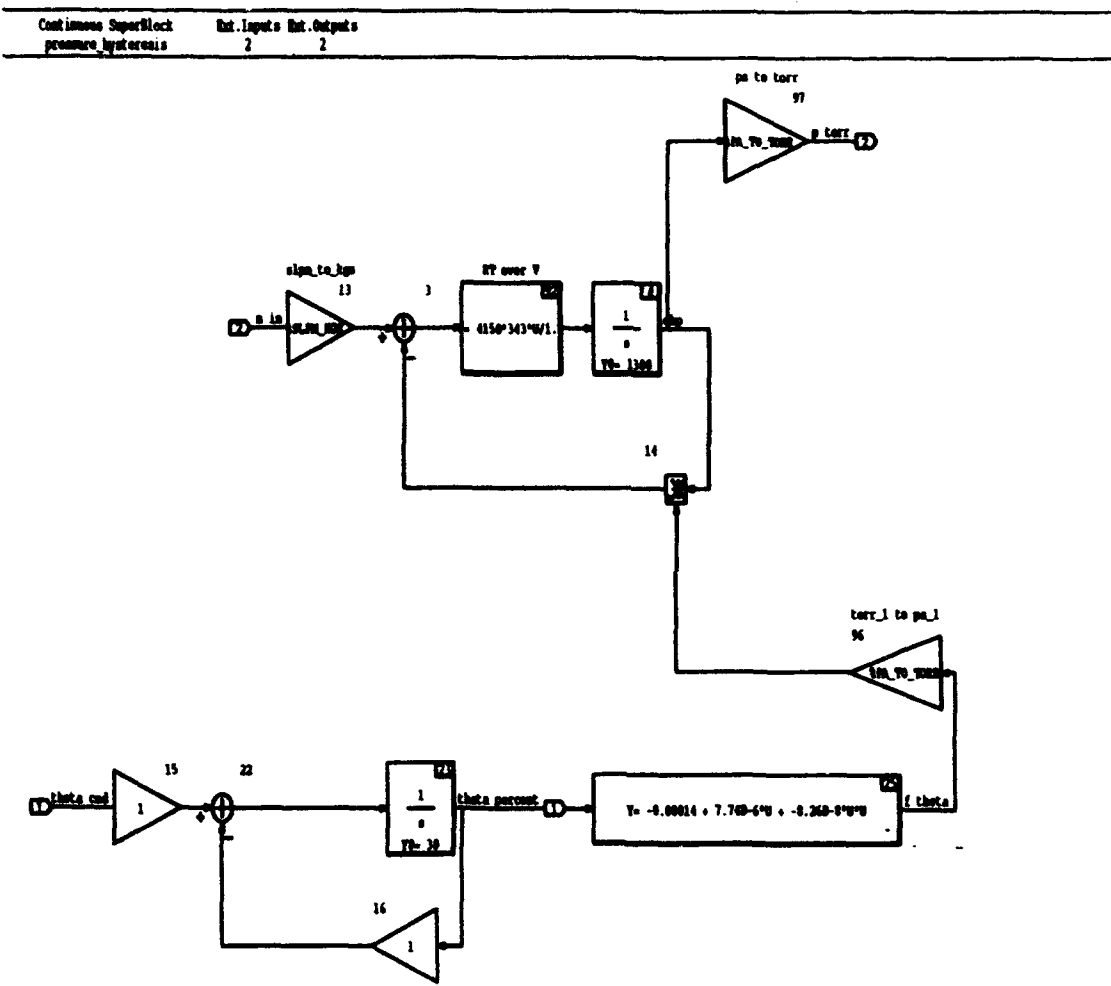


Figure C.5: SystemBuild model for chamber pressure.

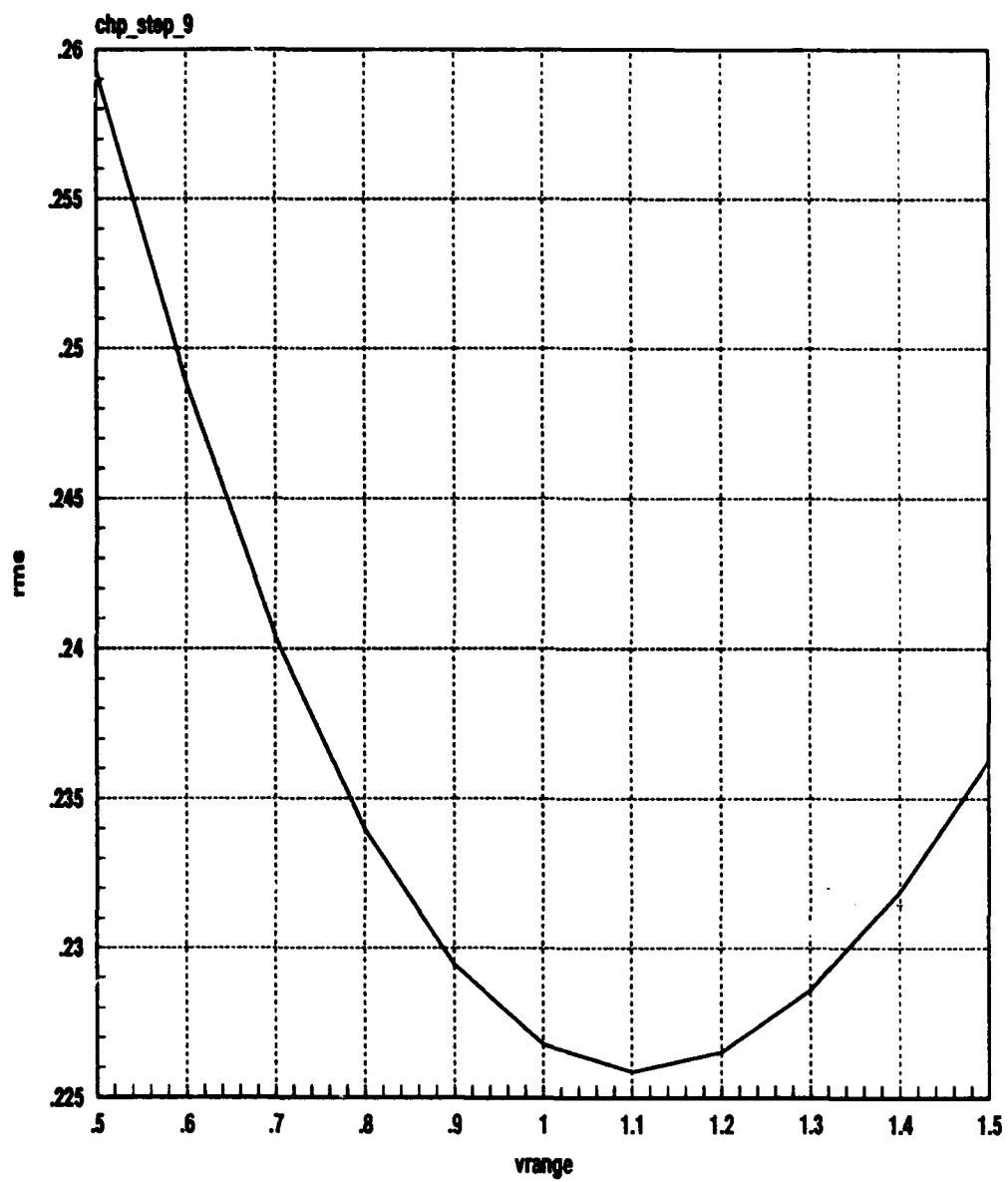


Figure C.6: Rms error for calculating chamber volume.

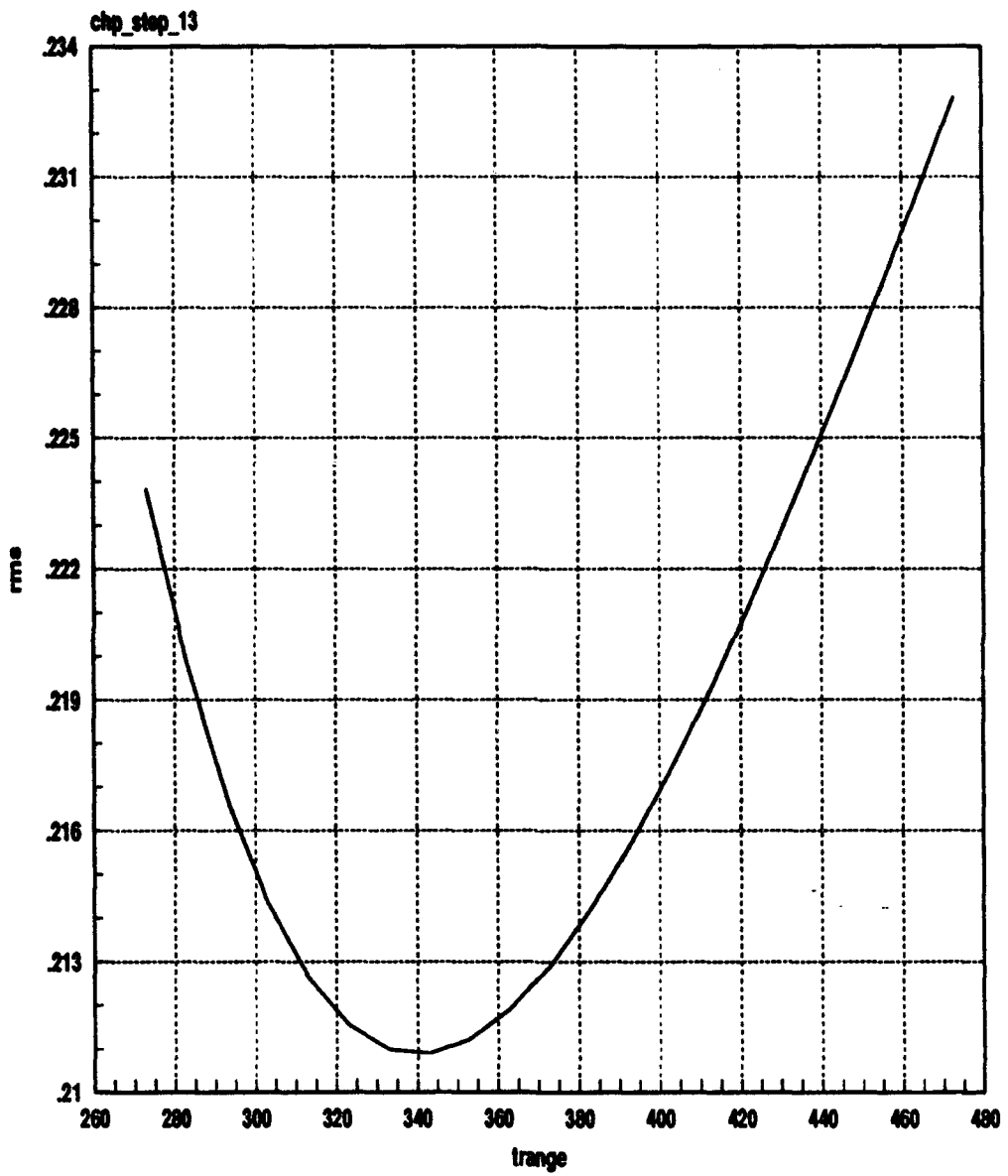


Figure C.7: Rms error for calculating gas temperature.

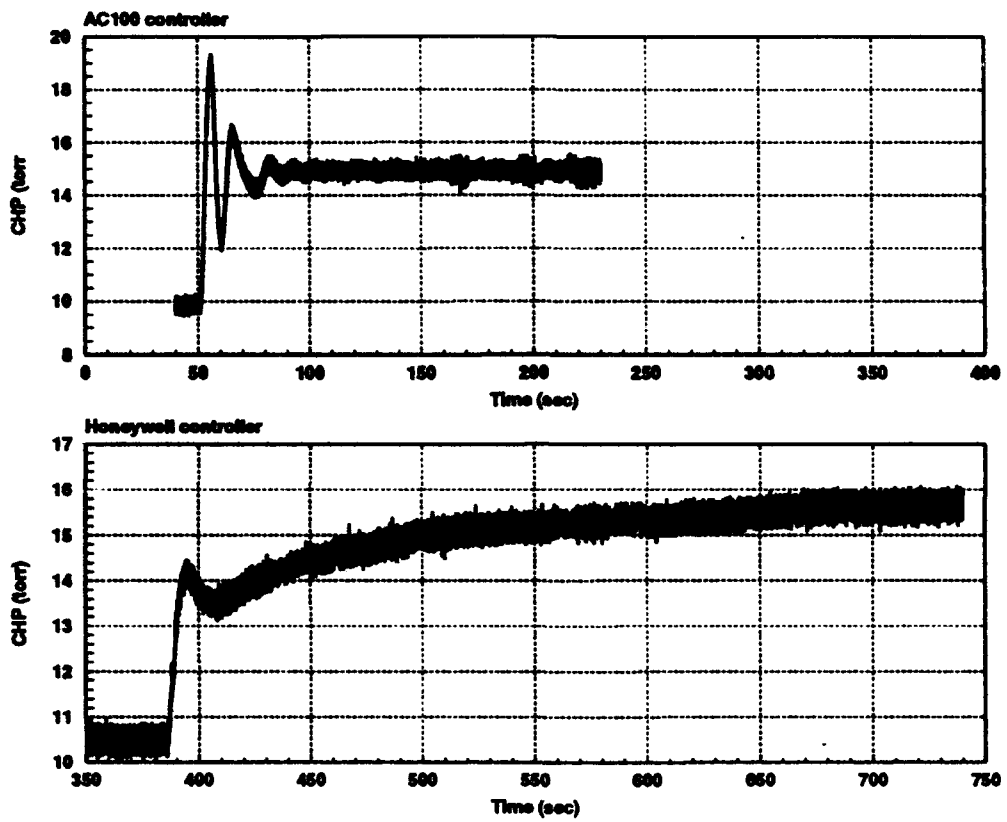


Figure C.8: Closed-loop response for controller implemented on an AC-100.

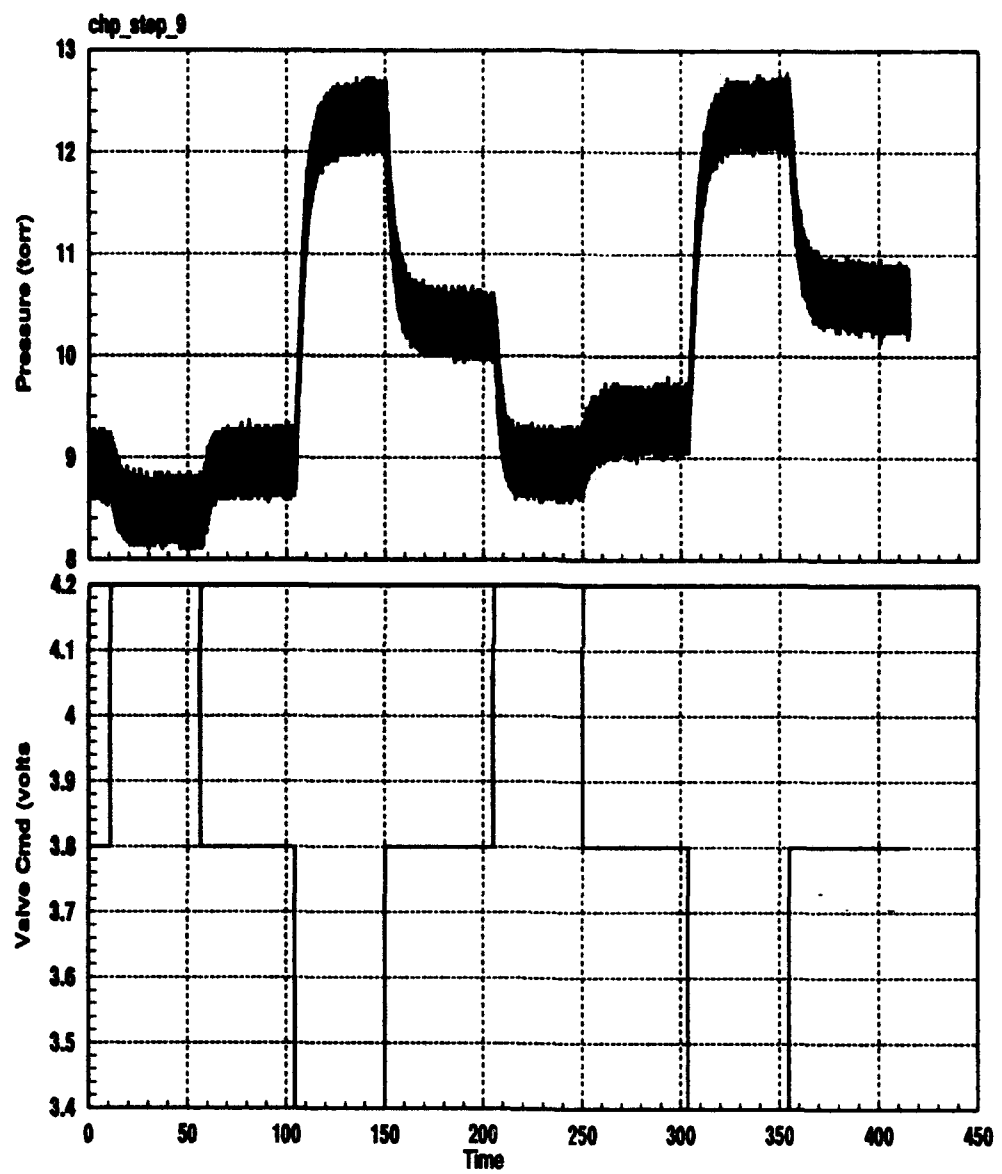


Figure C.9: Effect of valve hysteresis on chamber pressure.

Appendix D

Gas Rotational Temperature Sensor

D.1 Introduction

This appendix describes a sensor that has been developed for measuring the gas temperature in the plume of the arc jet. This sensor uses the emission spectra from the hot jet, specifically, the 430nm CH emission band (or CH A→X band). The spectral distribution of the line strengths in this band is dependent on the distribution of the rotational energies of the CH molecules. This rotational energy distribution can, for equilibrium distributions, be characterized by a rotational temperature. When the distribution of rotational energies equilibrates through collisions with a gas in local thermodynamic equilibrium the rotational temperature will be the same as the gas temperature.

This appendix is divided into three sections. The first section describes the apparatus used to acquire the spectrum, including the computer interface and data acquisition system. The second section describes the algorithm for estimating the rotational temperature and the two command line executable versions of the codes which implement this algorithm. Results obtained using these codes are presented. The third section describes the LabView implementation along with some results of real-time measurements on an arcjet plume.

D.2 Apparatus and Acquisition System

The emission from the hot arcjet plume is collected through a fiber optic cable that connects the collection optics near the reactor to the centralized detection system. The collection optics typically used includes a 50mm quartz singlet stopped at an f-number of approximately 1.4. The fiber optic, with a 0.2mm entrance pupil, is positioned near the focus of the singlet providing a reasonable depth of field at the arcjet plume.

The emission spectra from the hot plume is detected using a grating monochromator equipped with an intensified silicon detector array and an optical multichannel analyzer (OMA). The OMA provides a complete spectra at 630 wavelengths at a rate of approximately one spectra every 1-3 seconds. The acquisition rate depends on the user selected detector integration time. The spectra, both wavelength and spectral intensity, are passed to a Macintosh (Apple) computer through a GPIB interface. The Macintosh uses the LabView (National Instruments) software to acquire the spectrum and write it to a file. The command line versions of the rotational temperature codes analyze this data file. Another LabView VI (virtual instrument) has been developed which continuously (once every 2-3 seconds) analyzes spectra arriving from the OMA and outputs a rotational temperature. This real-time version of the rotational temperature sensor is implemented as C-code linked with LabView, and requires no user intervention beyond startup.

D.3 Rotational Temperature Estimation

The rotational temperature is estimated by comparing the measured CH emission (420-440nm) with spectra computed using a Fortran program called RLS, provided by Jay Jeffries of SRI. The RLS code was apparently first implemented by Zare, *et al.*, after the paper "A direct approach for the reduction of diatomic spectra to molecular constants for the construction of RKR potentials.", J. Mol. Spec. 46, pp.37-66, 1973. Zare's implementation was intended to provide a means of deducing molecular constants from a spectrum, and was not intended to provide an exact match to measured spectrum. Nevertheless, in the current implementation we have used molecular constants to model the emission spectrum. We are primarily interested in the temperature dependence of the rotational line intensity distribution, and less interested with the exact match to the spectrum, or with higher order bands. The RLS Fortran code is not included here, but the codes described here incorporate output from RLS.

The output from RLS is a list of line positions and line strengths, among other data. These line positions and line strengths must be convolved with a slit function for a specified bandwidth to produce the spectra. The code `slitall` convolves the lines with a slit function to produce spectra for a user specified detector bandwidth and user specified wavelength range. The RLS output is hard coded into `slitall` for the temperatures 1500, 1750, 2000, 2250, 2500, 2750, and 3000 K. The outputs from `slitall` are spectra at these seven temperatures. Figure D.1 shows these calculated spectra for a bandwidth of 0.15 nm and normalized to unity at the peak emittance. The output from `slitall` should be directed to a file named `slitall.out` where the next code, `rms_vs_t`, can find it.

Once the spectra are computed for a range of temperatures, the code `rms` compares measured spectra with the computed spectra and finds the best match. For example, Figures D.2, D.3, and D.4 show a comparison between computed spectra and the the measured

spectrum for positions in the arc jet labeled C0, C4, and D0, respectively. From these figures it is clear that the spectrum is most sensitive to temperature in the wings of the band. This result reflects the fact that the populations of higher energy rotational states increases with increasing temperature. The population of the lowest energy states has a weaker temperature dependence¹.

To facilitate the matching between the measured spectrum and the calculated spectrum, *rms* uses the following algorithm:

1. Allocate memory for arrays.
2. Read command line input (to be discussed later).
3. Open the output file *rms_vs_t.out* for printing results.
4. Read computed spectra (at seven temperatures) from file *slitall.out*. If *rms* cannot find *slitall.out* it will not run.
5. Read the file *rms_vs_t.cfg* to obtain a list of files from which measured spectra are to be read. *rms* will calculate the temperature for each file named.
6. For each readable file name found in *rms_vs_t.cfg* do the following:
 - a. Read measured spectrum. This is done by reading one line at a time. If the first two words on the line can be converted to real numbers then the first is assumed to be wavelength in nm and the second is assumed to be signal. Lines that can't be converted are ignored. A minimal amount of checking is done to ensure the data is valid - this is the responsibility of the user.
 - b. Normalize the measured spectrum. The signal is scaled to span from 0 to 1, where the maximum (1.0) is the peak signal lying in the wavelength range from 430 to 432 nm.
 - c. Compute the weighting from the calculated signal (to be discussed later). This calculation could be moved out of this inner loop, since it does not currently use the measured data.
 - d. Shift the wavelength of the measured signal by an integer number of pixels until the peak signal is near the peak signal of the computed spectra.
 - e. Calculate the RMS difference between the measured spectrum and the computed spectrum, one RMS difference for each of the seven computed temperatures. This is done with one of three weighting schemes, depending on the first command line argument, and is discussed below.

¹The Boltzmann population of the J 'th rotational state is $N_J = N_0(2J+1)\exp(-E_r/kT)$, thus $dN_J/N_J = (E_r/kT)(dT/T)$. Since the rotational energy is $E_r \simeq BJ(J+1)$, the sensitivity of N_J to temperature increases with increasing energy, and goes to zero at $J = 0$.

- f. Fit a cubic spline to the seven computed values for RMS(T), and find the temperature, T, at which RMS(T) is minimum.
 - g. Print output to the default output file, `rms_vs_t.out` and to the console. If the command line flag for `plotoption` is non-zero, then print long form MATRIX_x results to the output file.
7. Close the output file and quit.

The command line arguments for `rms` are a real weight parameter, WT, followed by an optional non-zero integer that flags the code to produce long form output readable by MATRIX_x. The WT parameter is required and can be positive, zero, or negative. WT determines how `rms` will compute the RMS difference between the measured and calculated spectra, as mentioned above. The options are:

WT=0. When WT=0 `rms` will compute the rms difference giving all wavelengths equal weighting. For example,

$$RMS = \sqrt{\frac{1}{n} \sum_{i=1}^n [I_{\text{calc}}(\lambda_i) - I_{\text{meas}}(\lambda_i)]^2 w(\lambda_i)}$$

where

$$w(\lambda_i) = \begin{cases} 0 & ; 431.5 \leq \lambda_i \leq 435 \text{ nm} \\ 1 & ; \text{otherwise} \end{cases}$$

The weighting function, $w(\lambda_i)$, is always set to zero in the range from 431.5 to 435 nm to discard the unmodeled higher order CH vibrational band ($v'' = v' = 2$) and the hydrogen emission line. The problem with this uniform weighting scheme is that small errors in temperature sensitive spectral regions and those in temperature insensitive regions are weighted equally.

WT>0 When WT is positive, the uniform weighting function discussed above is replaced with a function that is proportional to dI/dT . The code, `rms`, calculates dI/dT using the computed spectra. Then it normalizes the result to obtain the function $w'(\lambda_i)$ which spans 0 to 1. Finally `rms` constructs the function $w(\lambda_i) = 1 + WT w'(\lambda_i)$. Setting WT=100,000 gives 100,000 times more weight to the most temperature sensitive wavelength, compared to the least temperature sensitive wavelength. A value of WT=1 doubles the weight given to the most temperature sensitive part of the spectrum, compared to the least sensitive wavelengths. Figure D.5 shows the function $w(\lambda_i)$ for WT=100,000.

WT<0 When WT is negative, the weighting function is defined as

$$w(\lambda_i) = \begin{cases} 0 & ; 431.5 \leq \lambda_i \leq 435 \text{ nm} \\ 1 & ; \lambda_i < 431.5 \text{ nm} \\ -WT & ; \lambda_i > 435 \text{ nm} \end{cases}$$

This scheme looks primarily at the long wavelength (P-branch) of the spectrum to determine temperature. From Figure D.5 we see that this is the most temperature sensitive part of the spectrum. The problem with this scheme is that it relies heavily on a small portion of the spectrum that is has relatively weaker signals.

All of the three weighting schemes discussed above have disadvantages, however the scheme currently favored is $WT > 0$. This scheme attempts to fit the entire spectrum, thus is less sensitive to small variations at any one wavelength. Also, this scheme places additional importance on fitting the curve at temperature sensitive wavelengths. Finally, this scheme makes use of the strongest signals, those near the central Q branch, where the S/N should be largest.

The major disadvantage of the $WT > 0$ scheme is that it attempts to match the central Q-branch of the spectrum to spectra computed with only the $v'' = v' = 0$ vibrational transition. This fit ignores the overlapping $v'' = v' = 1$ vibrational transition. The end result is that r_{ms} will tend to overestimate the emission temperature, mistaking increased population of the $v = 1$ vibrational state with broadening of the fundamental Q-branch. Comparing the results using $WT > 0$ and $WT < 0$ seems to confirm this result, as illustrated in Table D.1.

Some results are presented in Table D.1, and some curves of RMS versus T are shown in Figure D.6 and Figure D.7. It is evident that 100 K changes in temperature affect the fit error by small amounts. This does not, in itself, speak to the precision of the measurement, since we have not looked at two data sets that were taken for the same position in a steady state temperature.

D.4 Real-Time Implementation

A real-time implementation of the above computer codes has been developed by ISI to allow continuous measurement of the rotational temperature at the Technion facility. A LabView code interface node (CIN) was developed in C to provide a fully functional version of the codes described above. The CIN was incorporated into a LabView virtual instrument (VI) that periodically reads the spectral data from the OMA. The rotational temperature is estimated for each spectra and a running mean and standard deviation is computed. The rotational temperature can be saved to a file or converted to an analog voltage and output from the computer's D/A.

In the previous section the results are based on analyses of single spectra. Noise in the spectrum is not accounted for, and no estimate of the uncertainty in the calculated temperature is available. With this LabView implementation a statistically large number of sample is readily obtainable. A histogram of rotational temperature versus temperature was obtained by measuring the rotational temperature approximately 40 times while the operating

conditions remained fixed. For the results shown in Figure D.8, the mean temperature is approximately 3045 K with a standard deviation $\sigma \simeq 14$ K. The distribution about the mean appears to be quite Gaussian, which suggests that using ordinary statistical uncertainty estimates are appropriate. Other measurements were done with lower signals by increasing the f-number of the collection optics. The effect of this decrease in signal relative to noise (S/N) was that σ increased but the distribution remained Gaussian about a mean temperature.

Using the mean and standard deviation measure of T_{rot} discussed above, the rotational temperature of a plume on the TB reactor was measured for various arcjet enthalpies. The results are shown in Figure D.9. For comparison, the equilibrium temperature versus enthalpy was computed assuming chemical equilibrium between the H and H₂. The results compare well.

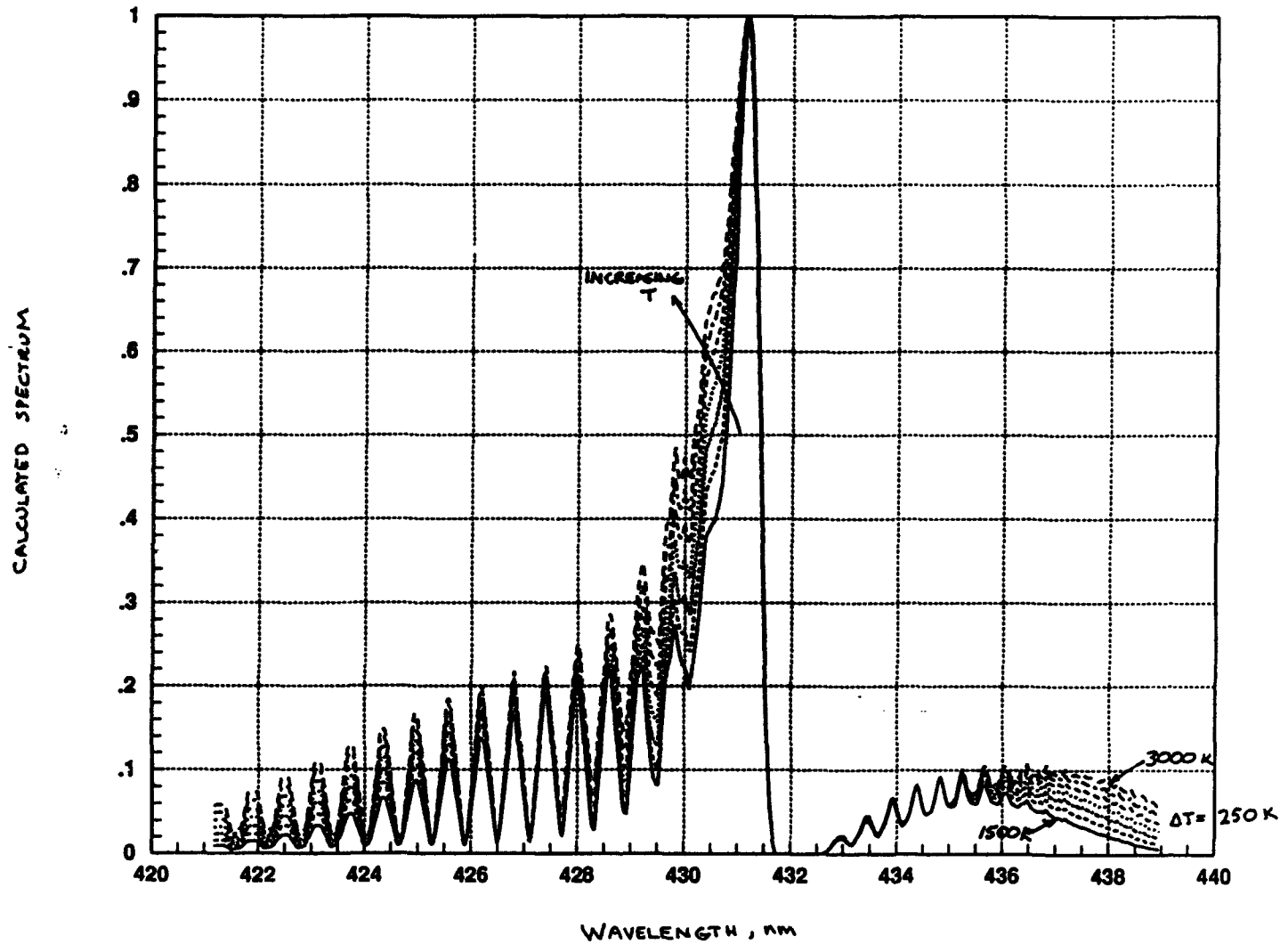


Figure D.1: Calculated rotational spectrum at various gas temperatures.

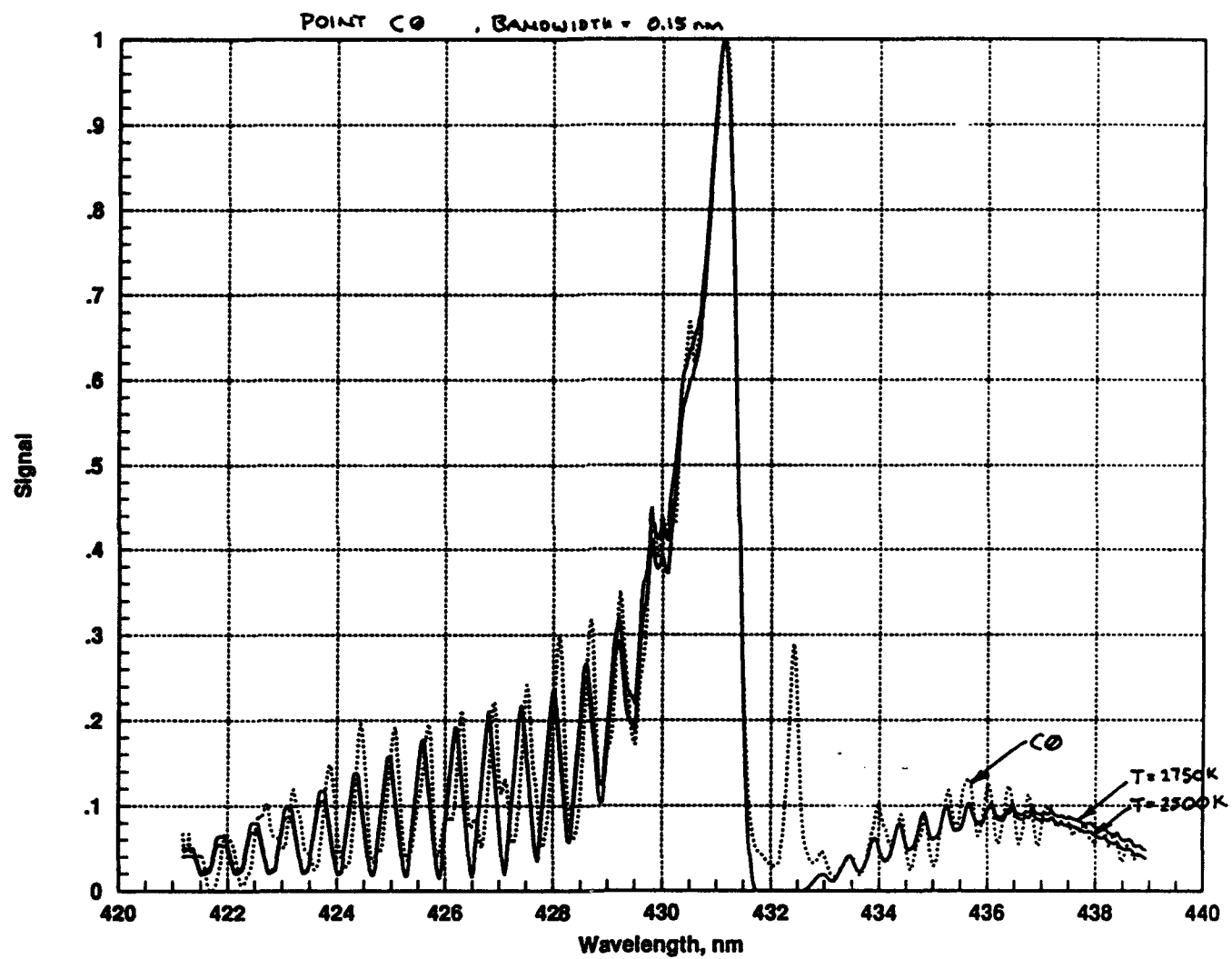


Figure D.2: Comparison of measured and calculated rotational spectrum at point C0.

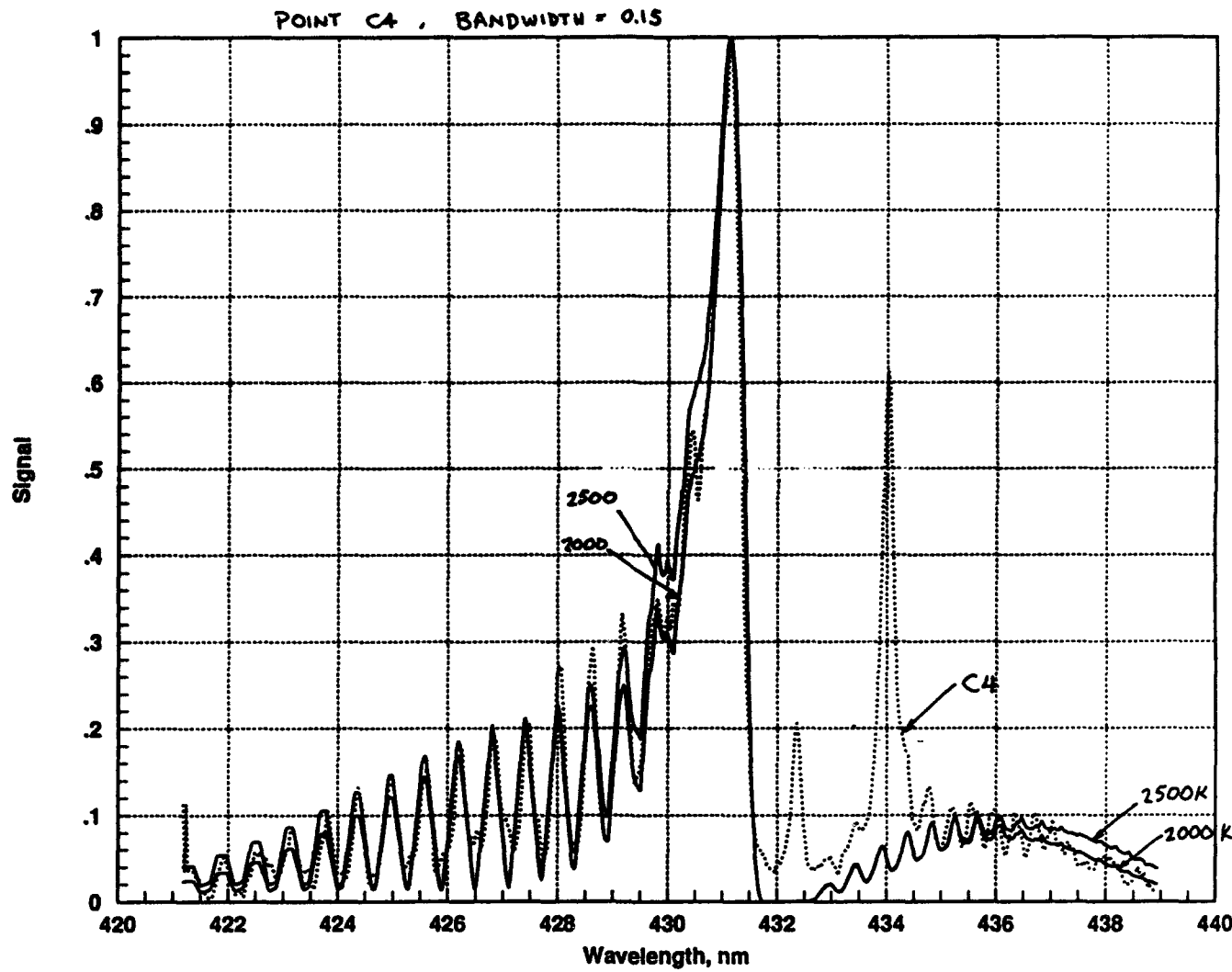


Figure D.3: Comparison of measured and calculated rotational spectrum at point C4.

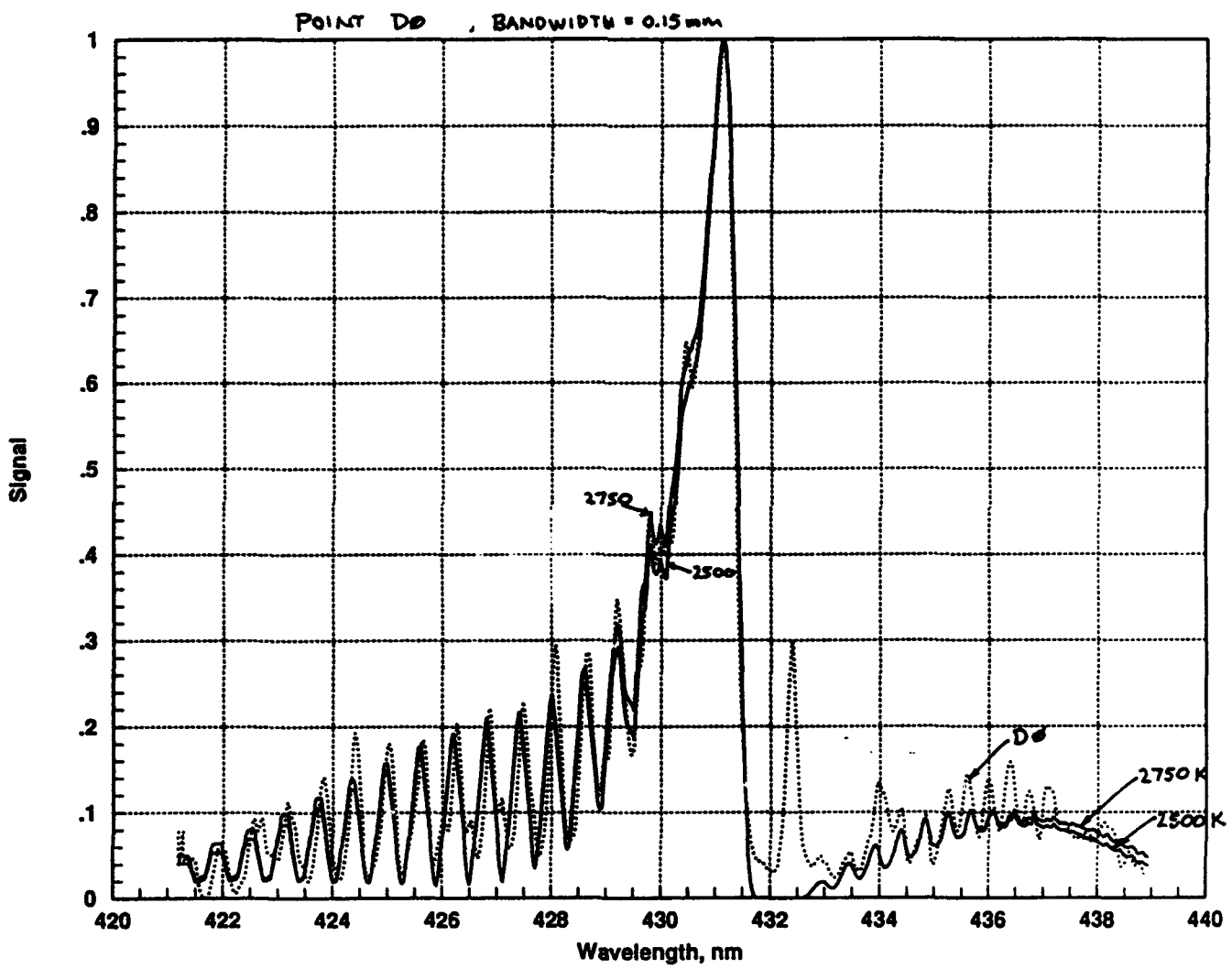


Figure D.4: Comparison of measured and calculated rotational spectrum at point D0.

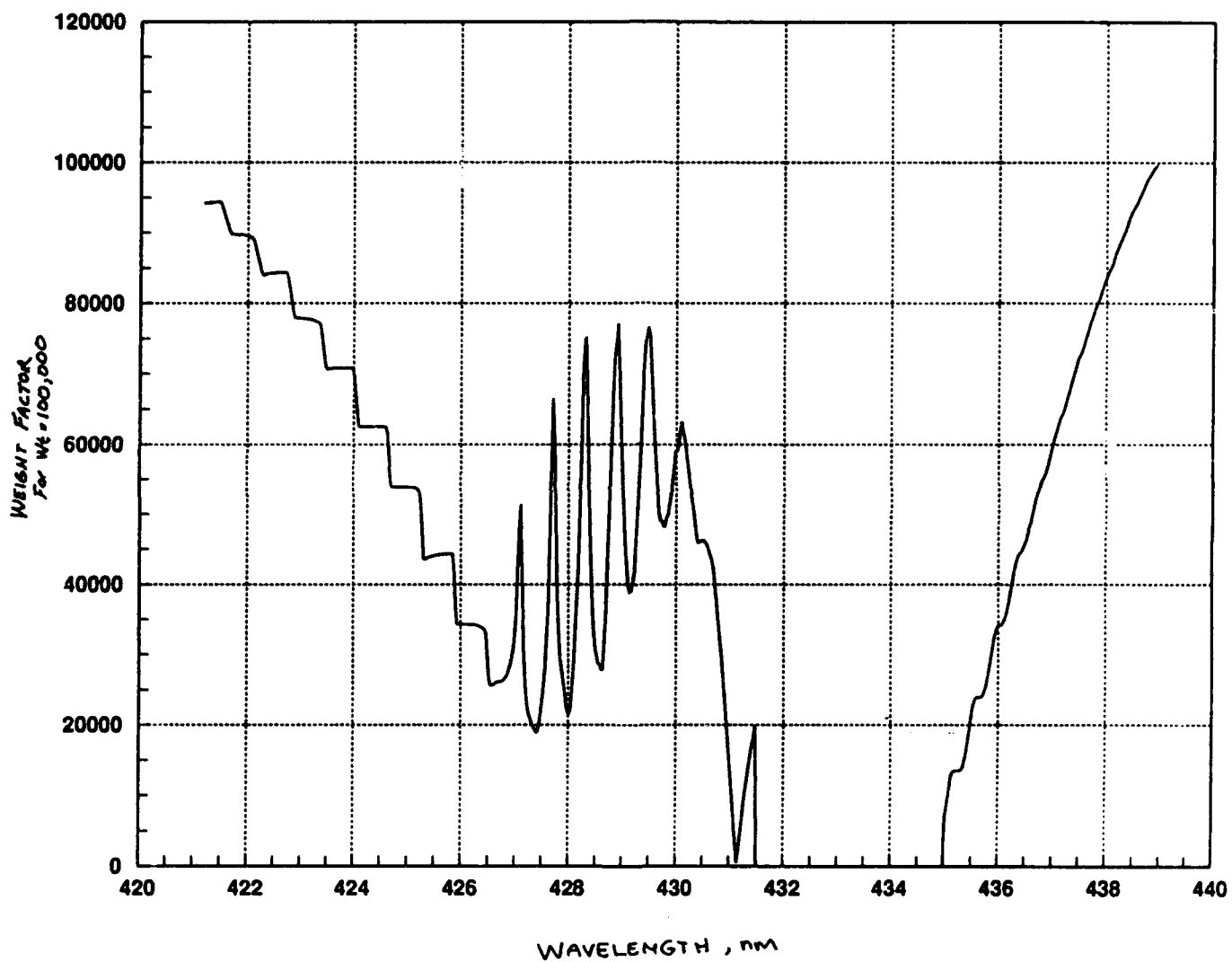


Figure D.5: Example weighting function used in estimating rotational temperature.

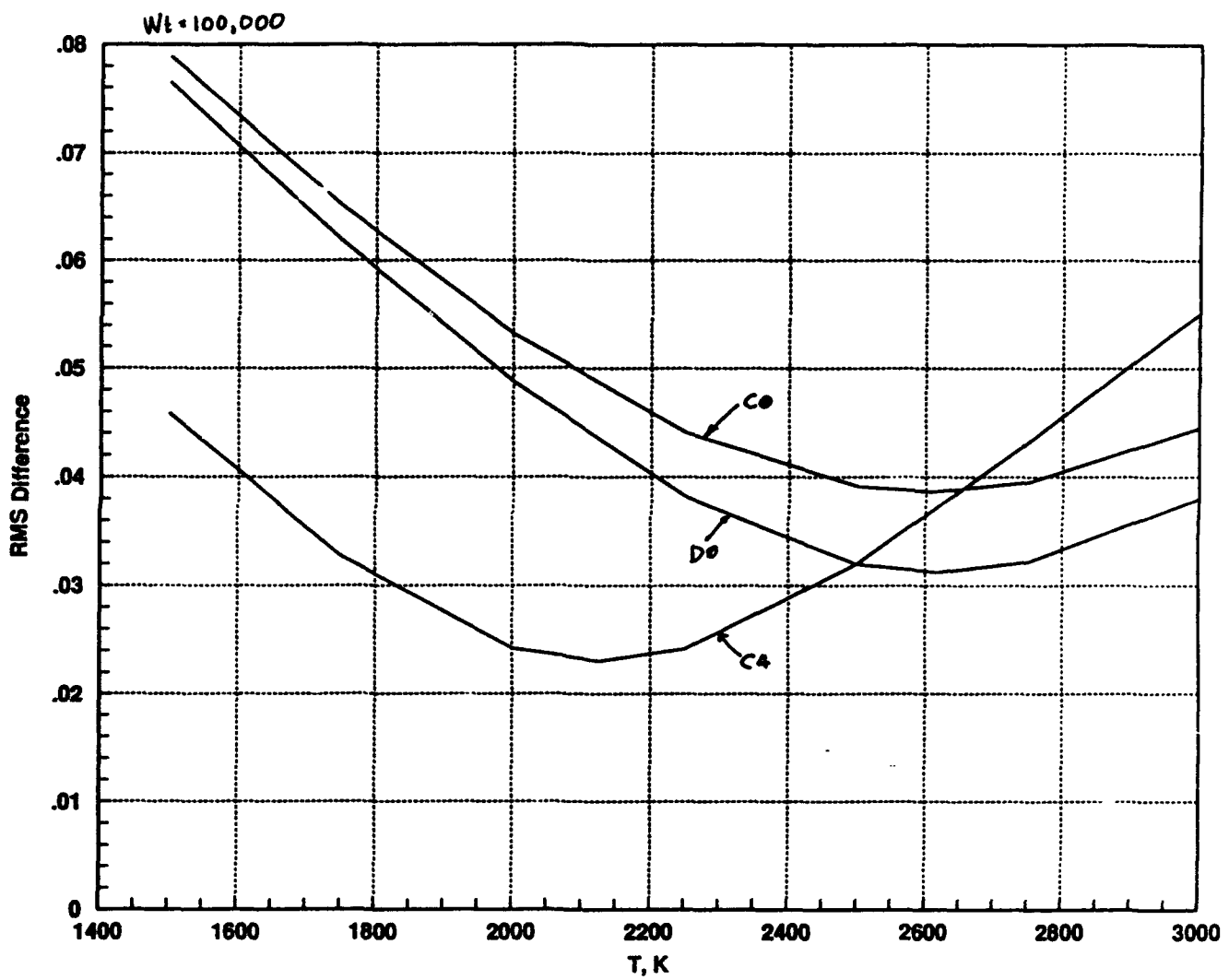


Figure D.6: Rms error in rotational spectrum fit using $WT=100,000$.

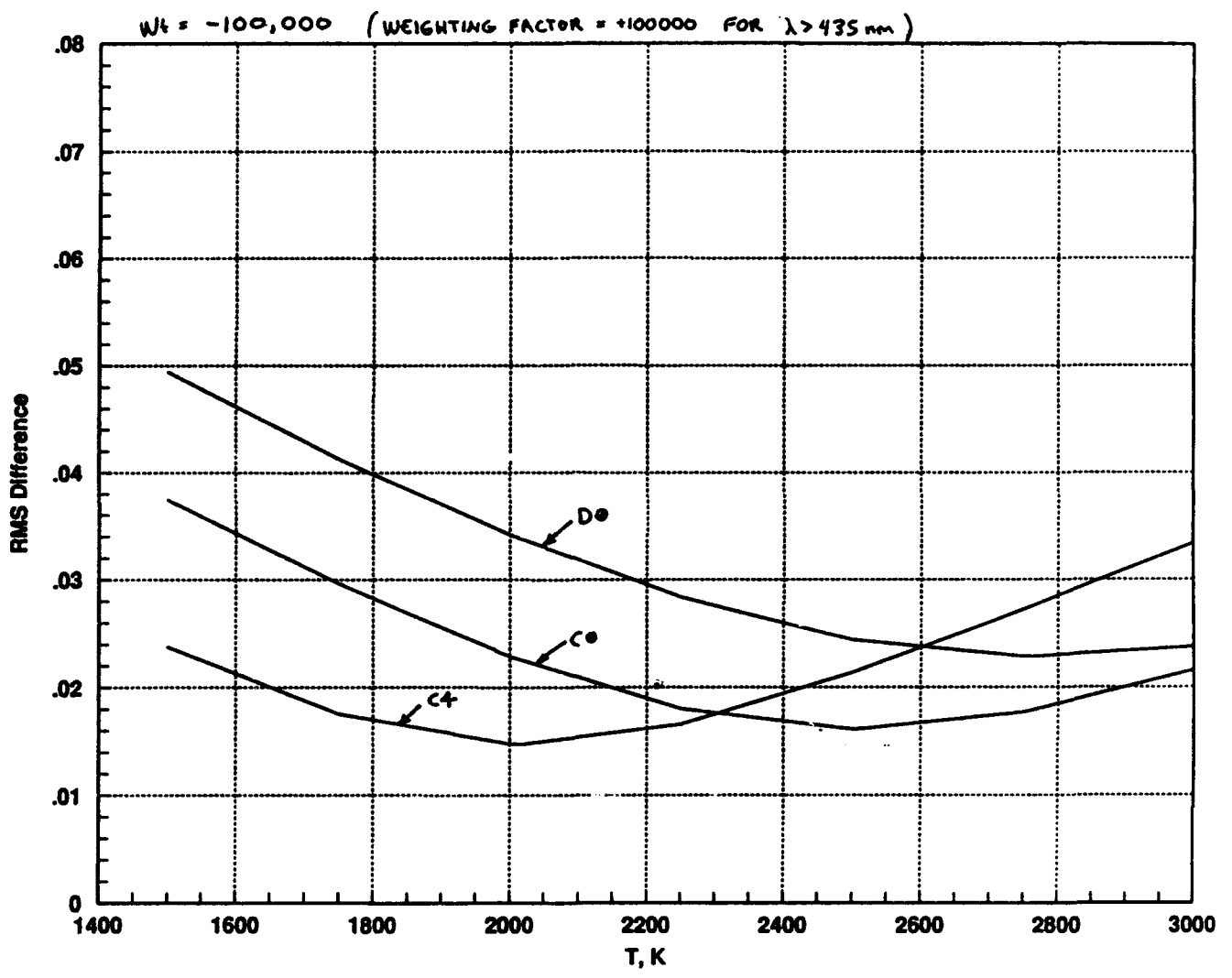


Figure D.7: Rms error in rotational spectrum fit using $WT=-100,000$.

Wt=0

A0:2658	A1:2569	A2:2106	A3:2175	
B0:2727	B1:2616	B2:2252	B3:2123	B4:1789
C0:2610	C1:2412	C2:2068	C3:2180	C4:2152
D0:2635	D1:2642	D2:2194	D3:2156	D4:2088
E-1:2581		E2:2366	E3:2363	E4:2123

Wt=100000

A0:2637	A1:2541	A2:2102	A3:2143	
B0:2684	B1:2572	B2:2218	B3:2126	B4:1877
C0:2608	C1:2421	C2:2082	C3:2146	C4:2125
D0:2617	D1:2586	D2:2133	D3:2087	D4:2034
E-1:2558		E2:2343	E3:2339	E4:2107

Wt=-100000

A0:2411	A1:2356	A2:1872	A3:1932	
B0:2468	B1:2403	B2:1965	B3:1933	B4:1978
C0:2507	C1:2319	C2:1977	C3:1983	C4:2020
D0:2762	D1:2518	D2:1874	D3:1805	D4:1812
E-1:2645		E2:2216	E3:2228	E4:2060

Table D.1: Rotational CH temperature estimated using various weightings.

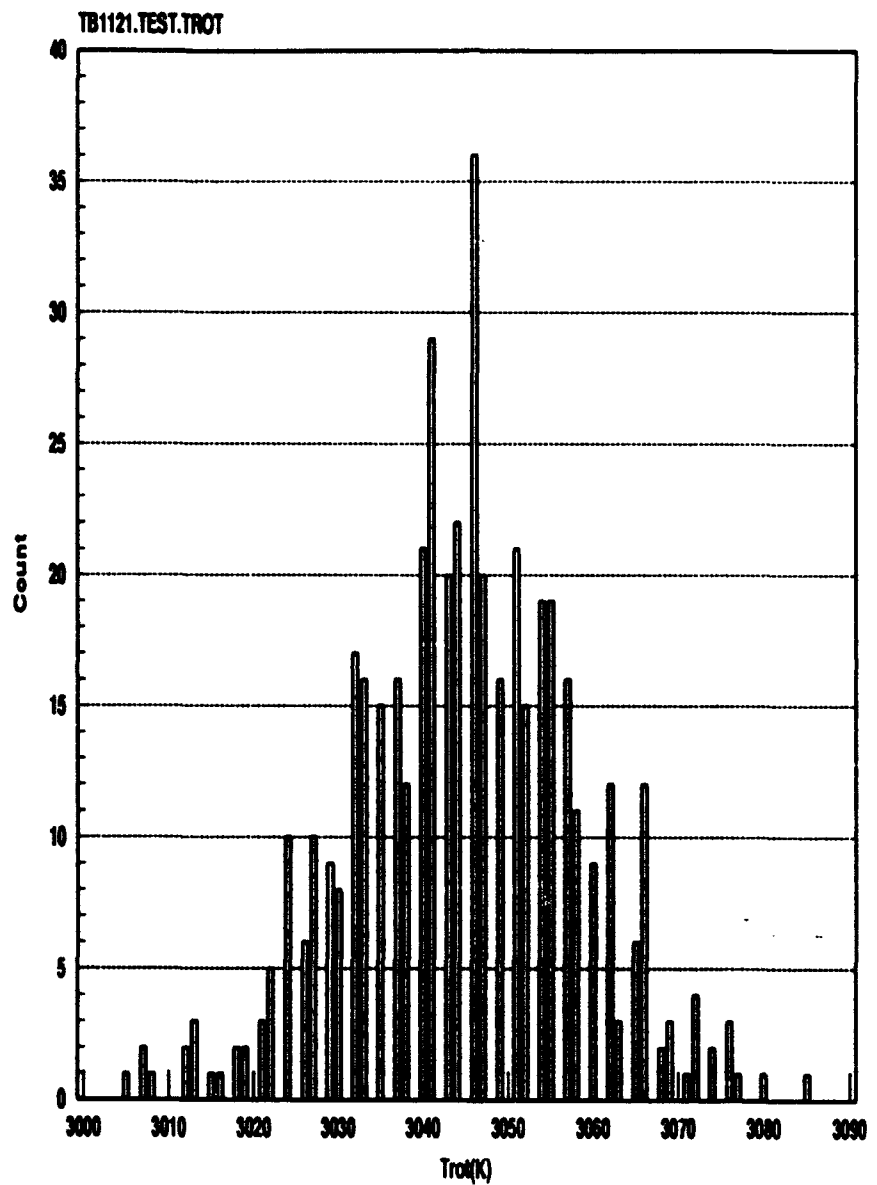


Figure D.8: Histogram of Rotational Temperature.

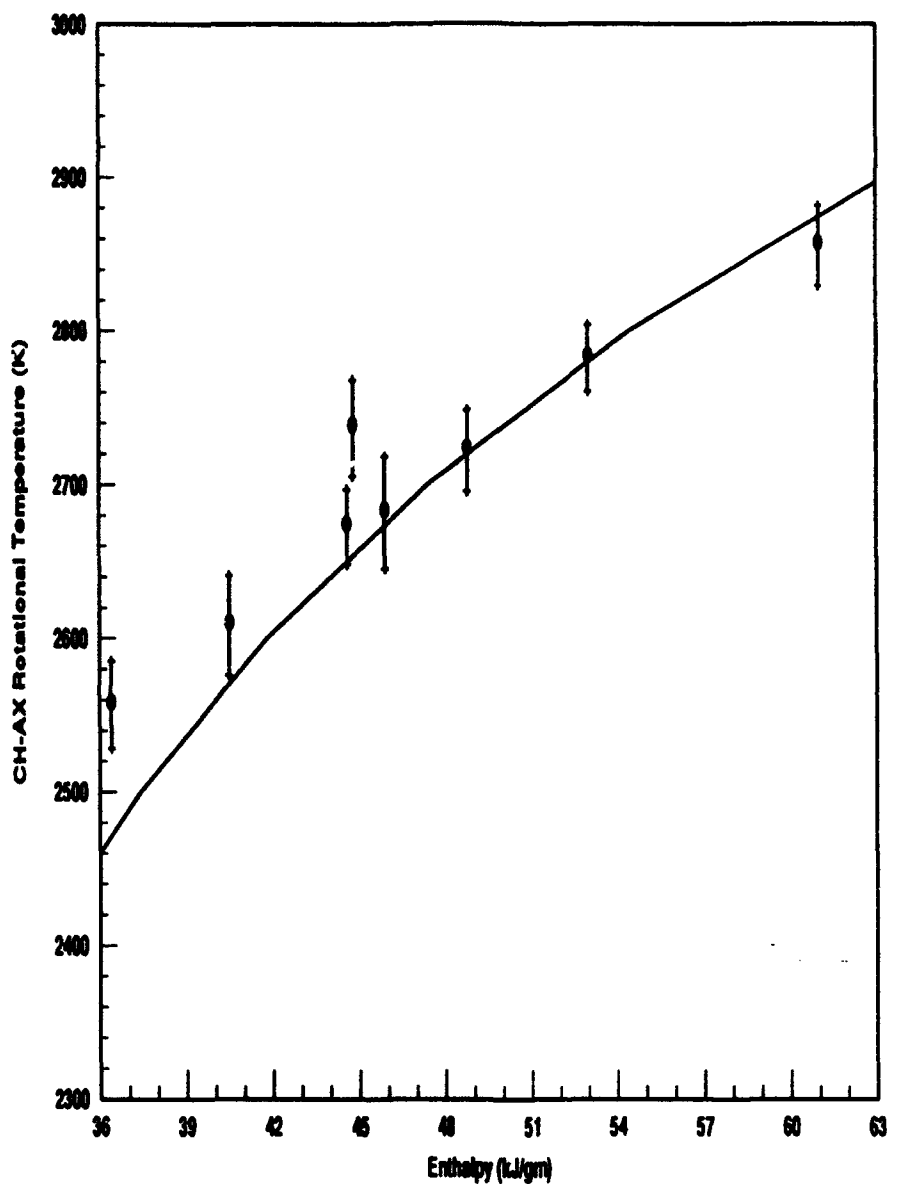


Figure D.9: Rotational temperature versus enthalpy compared to an equilibrium calculation assuming H₂H₂ equilibrium.